Controlling Interfacial Magnetism of Transition Metal Oxides in Proximity of Ferroelectrics

Abhishek Ranna

A Dissertation Submitted for the Partial Fulfilment of
Master of Science Degree

Indian Institute of Science Education and Research Mohali

May, 2022

Certificate of Examination

This is to certify that the dissertation titled “ **Controlling Interfacial Magnetism of Transition Metal Oxides in Proximity of Ferroelectrics** ” submitted by **Abhishek Ranna** (Reg. No. MP19004) for the partial fulfillment of MS Degree programme of the institute, has been examined by the thesis committee duly appointed by the institute. The committee finds the work done by the candidate satisfactory and recommends that the report be accepted.

Kavita Dorai

Prof. Kavita Dorai

Dr. Ananth Venkatesan

D Samal

Dr. Debakanta Samal

(Co-Supervisor)

Biswas

Dr. Samir Kumar Biswas

(Supervisor)

Dated: 5th May, 2022

Declaration

The work presented in this dissertation titled " **Controlling Interfacial Magnetism of Transition Metal Oxides in Proximity of Ferroelectrics** " has been carried out by me under the guidance of Dr. Samir Kumar Biswas at the Indian Institute of Science Education and Research, Mohali.

This work has not been submitted in part or in full for a degree, a diploma or a fellowship to any other university or institute. Whenever contributions of others are involved, every effort is made to indicate this clearly, with due acknowledgment of collaborative research and discussions. This thesis is a bonafide record of original research work done by me and all sources listed within have been cited in the references.

Abhishek

Abhishek Ranna
(Candidate)

Dated: 5th May, 2022

In my capacity as the supervisor of the candidate's research work, I certify that the statements made above by the candidate are true to the best of my knowledge.

Biswas

Samir Kumar Biswas
(Supervisor)

Dated: 5th May, 2022

Acknowledgements

First and foremost, I would like to express my sincere gratitude and most profound respect for my thesis supervisors Dr. Samir Kumar Biswas (IISER Mohali) and Dr. Debakanta Samal (IoP Bhubaneswar) for having given me the opportunity to work in their research groups. Their constant encouragement, uncompromising support, and indispensable guidance were instrumental in my academic and personal growth. I thank them from the bottom of my heart for teaching me all the aspects of academic research, from reading scientific articles and formulating research problems to performing experiments.

Despite being trapped in a vortex of meetings and administrative duties, both my supervisors never denied for help when I needed it. Working with them was an honour and I am truly indebted to them. The most important lesson that I have learnt from under their guidance is to remain optimistic in our life constantly and face every challenge with utmost courage and determination.

I am incredibly thankful to Dr. Shweta G. Bhat (IISc Bangalore) for helping me perform X-Ray Diffraction and Atomic Force Microscopy experiments on my thin film samples.

I am very much thankful to Dr. Raj Kumar Roy (IISER Mohali) for allowing me to carry out P-E measurements on my samples in his laboratory.

I thank our Scientific Officer, Dr. Sachin Sarangi (IoP Bhubaneswar), for his technical and logistical assistance.

I thank the IISER Mohali Library and Computer Center for providing me the necessary reading materials (books, journals, and articles) along with essential software subscriptions without which my research work would not have been possible.

I want to acknowledge my current lab members from the BioNaP Lab, IISER Mohali (Dr. Sriram, Dr. Nur, Amit, Sarvesh, Aniket, Nagendra) and the Designer Quantum Materials Lab, IoP Bhubaneswar (Dr. Ravinder, Subhadip, Digbijaya, Sairam, Pujalin) for creating a propitious environment to learn and grow. I would particularly like to single out Subhadip Jana. Subhadip, I thank you for your constant assistance in material synthesis, handling of the Pulsed Laser Deposition system, and constructive scientific discussions; I hope to get a chance of working with you again in the near future.

My gratitude goes to Shyam Sundar Yadav (ULTP Lab, IISER Mohali) for teaching me the fundamentals of device fabrication.

I thank Abhinna and Deya from the core of my heart, for their constant academic and emotional support during my stay at IISER Mohali. It is always a pleasure to acknowledge our memorable moments spent together.

Thank you, Akash and Shruti, for being the best roommates ever.

A special thanks goes to my school friend Ankita, who constantly helped and motivated me throughout my degree.

I want to thank my friends Prakriti and Karubakee, who were always a phone call away in my time of need.

Thank you, Ipsita Diii, for listening to all my problems and teaching me the real meaning of perseverance. Your influence drives me to become a better person and researcher.

I extend my thanks to all my other school and B.Sc. friends (Abinash, Rashmi, Chiku, Shubharam, Poonam, Minakshi, Swayang) who kept in touch with me and offered their generous help at times.

I wholeheartedly acknowledge all of my high school and college teachers who helped me build my educational foundation.

Finally, I am forever indebted to my parents - the paramount people in my life. Their constant love, affection, support, and faith throughout the years have made me the person I am today. I cannot ever thank them enough.

In the end, I thank the Almighty for blessing me with such nice people, because MS was a long journey for me that I could not have made alone.

Abstract

Electric control of magnetism has attracted a huge scientific attention due to both the fundamental importance and the tremendous technological potential. As a result of the coupling between the dual ferroic orderings, it can help attain unmatched performance and energy efficiency in the next-generation devices. However, the scarcity of naturally occurring magnetoelectric materials and the design complexities of electrostatic gating makes these approaches unfeasible for exploration for a large section of the condensed matter community. An exciting alternative to harness the great potential of magnetoelectric effect is by preparing artificial heterostructures with individual magnetic and ferroelectric components. In this thesis, we have attempted to control interfacial magnetism of candidate transition metal oxides by coupling with ferroelectric materials in heterostructures prepared by the Pulsed Laser Deposition method. First, the individual components of the heterostructures were studied in their thin film form. We synthesised the ferroelectric perovskite $Ba_{0.8}Sr_{0.2}TiO_3$ (BSTO) target material and optimised the growth of thin films, using structural characterisation techniques of X-Ray Diffraction, X-Ray Reflectivity and Atomic Force Microscopy. Electrical polarisation experiments and impedance analysis confirmed the ferroelectric nature of these films. In the next part, the growth of $La_{0.7}Sr_{0.3}MnO_3$ (LSMO) thin films was optimised by the same techniques, and a paramagnetic to ferromagnetic phase transition was observed around 320K by SQUID Magnetometry. Finally, the magnetoelectric heterostructure of BSTO/LSMO was grown and structurally characterised. This work will help improve our understanding of tailoring interfacial magnetic properties of TMO by exploiting the spontaneous electric polarisation of ferroelectric materials.

“To my parents, with love.”

Contents

List of Figures

List of Abbreviations

ME Magnetoelectric

FM Ferromagnet/Ferromagnetic

AFM Antiferromagnet/Antiferromagnetic

FE Ferroelectric/Ferroelectricity

TM Transition Metal

TMO Transition Metal Oxide

CFT Crystal Field Theory

SOJT Second Order Jahn Teller

PLD Pulsed Laser Deposition

RHEED Reflection High Energy Electron Diffraction

XRD X-Ray Diffraction

XRR X-Ray Reflection

AFM Atomic Force Microscopy

SQUID Superconducting Quantum Interference Device

BSTO $Ba_{0.8}Sr_{0.2}TiO_3$

BTO $BaTiO_3$

STO $SrTiO_3$

Nb:STO Nb doped $SrTiO_3$

LSMO $La_{0.7}Sr_{0.3}MnO_3$

RMS Root Mean Square

u.c. Unit Cells

Chapter 1

Introduction

Multifunctional materials, which unite different functionalities in the same phase, have attracted much attention in recent years due to their rich physics and a large variety of potential applications. In modern electronic devices, magnetism and transport are two key functional properties, thus active control of electronic and magnetic properties of these materials is the cornerstone for the development of future engineered devices, which promising enhanced level of functionality and tailorability while decreasing the cost, size, and power consumption.

1.1 Motivation: Electric Field Control of Interfacial Magnetism

To achieve higher energy efficiency and better performance, a large wave of interdisciplinary explorations have been inspired to integrate multiple physical properties into one system. One such class of materials are the multiferroic magnetoelectric (ME) compounds, which simultaneously show ferroelectricity (FE) and magnetic ordering such as, ferromagnetic (FM) or antiferromagnetic(AFM) have gained immense interest, since they offer the possibility to control the magnetic state via local electric fields which has great technological potential [1–4]. The electrical control of magnetism is of interest not only because of its technological importance, but also because it allows us to uncover properties of magnetic materials that are otherwise inaccessible [5].

Unfortunately, very few intrinsic multiferroic ME materials exist in nature. The coexistence of these two orders in a single phase compound is rare due to the contrasting electronic structures typically required for ferroelectric and ferromagnetic behaviour [6]. The atomistic origin of ferrolectricity requires d^0 configuration of the transition metal ion, magnetism on the contrary, requires partially filled d states that give rise to long range exchange interactions. This makes the two phenomena incompatible in terms of electronic structure, which in turn limits our ability to artificially synthesise such oxides [7]. Although some compounds, such as $BiMnO_3$ or $BiFeO_3$ with magnetic Mn^{3+} and Fe^{3+} ions, are ferroelectric. However the ferroelectric distortion here is due to the the shifting of Bi atom within the crystal. Because the ferroelectric and magnetic orders in these materials are associated with different ions, the coupling between them is too small to be useful in technological applications [3, 8, 9].

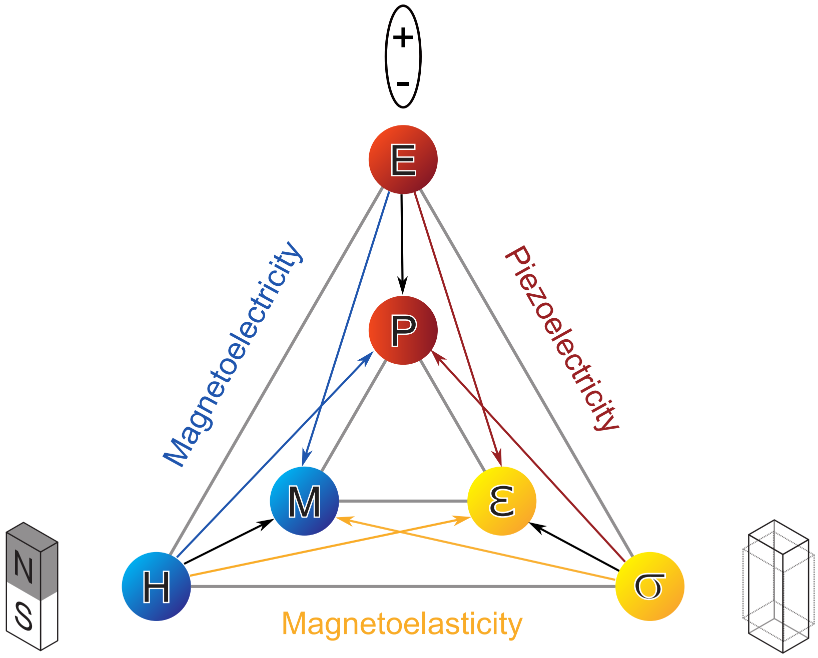

Figure 1.1: Phase control in ferroics and multiferroics.The electric field E, magnetic field H, and stress σ control the electric polarization P, magnetization M, and strain ε, respectively.

A time-honoured approach to change the properties of oxides is to alter the chemical composition by introducing dopant atoms and vacancies in the crystal structure, popularly known as chemical doping [10, 11]. This approach has obvious pitfalls which bottlenecks their implementation in next-generation nano-scale devices: (1) Chemical doping is not easily tunable, requiring the synthesis of new samples for each level of doping, (2) Apart from altering the chemical composition, this process also introduces unwanted disorder which can also affect its properties.

An attractive alternative to tune the electronic and magnetic properties of materials and simultaneously achieve magnetoelectric control in the system is through *electrostatic gating* [12, 13]. In gating, an electrostatic field is applied to the material, creating a field effect. This allows for modifications of the electronic and magnetic properties through controlled and reversible changes of the carrier concentration without introducing any additional level of disorder into the system. But extensive study of electrostatic gating effect by the diverse condensed matter community becomes challenging due to the inherent complexity in fabricating field effect devices [14]. A lot of steps are involved in the fabrication of a single sample like preparation of material thin films, multiple cycles of lithography and nano-structuring, contact deposition and lift off processes. All these require state of the art equipment, sometimes within the same research facility which prohibits the scope of exploration.

A solution to the aforementioned problems are composite material systems, in which ferromagnetic and ferroelectric compounds are artificially assembled heterostructures [15, 16]. These structures, which are referred to as extrinsic multiferroic composite structures, enable large magnetoelectric effects at room temperature by exploiting the coupling between the two ferroic constituents. And it also allows for electrostatic manipulation by the virtue of the ferroelectric material's local electric field [17, 18].

When a metal is exposed to an electric field, a surface charge is induced, $\sigma = \varepsilon_0 E$, this screens the electric field over the screening length of the metal. In case of a metallic FM, this screening charge is spin dependent due to the exchange splitting of the spin bands, which induces a surface magnetisation M_{surf} [19]. Duan *et. al* reports that a linear contribution to M_{surf} is determined by the surface ME susceptibility $\alpha_{\mathcal{S}}$ as

$$\mu_0 M_{\text{surf}} = \alpha_{\mathcal{S}} E \tag{1.1}$$

This observed ME effect can be substantially enhanced at the interface of a FM and a dielectric, because the surface charge scales with the dielectric constant $\sigma = \kappa\varepsilon_0 E$. First principle calculations have predicted the enhancement of $\alpha_{\mathcal{S}}$ by two orders of magnitude as compared to the bare FM thin films [20]. These electronically driven ME effects can be further enhanced by employing an FE material (inherently dielectric) to produce a field effect. The extensive possibility to control interfacial magnetism in oxide thin films by expitaxial coupling to ferroelectric materials are beautifully articulated in the review articles by Velev *et. al* [21], Ahn *et. al* [14], Song *et. al* [22] and Spladin [23].

1.2 Aim of the Thesis

The broad aim of this thesis is to modify the interfacial magnetic ordering of candidate transition metal oxides in proximity of ferroelectrics by fabricating magnetic/ferroelectric heterostructures and attempt to observe changes in magnetisation by the use of Superconducting Quantum Interference Device (SQUID) Magnetometry. In particular we have tried to manipulate the magnetisation of $La_{0.7}Sr_{0.3}MnO_3$ a well studied and established ferromagnetic transition metal oxide by interfacing it with $Ba_{0.8}Sr_{0.2}TiO_3$, a strained, high dielectric constant, low-leakage ferroelectric material. Another motivation to study the interface is that emergent physical phenomena often arise at interfaces of complex oxide heterostructures due to the interplay between various degrees of freedom, especially those with polar discontinuities.

1.3 Outline

This thesis is organised into 8 chapters

Chapter 1 (Introduction) is the current chapter which gives a general outline of the electric control of magnetism and the motivation of the thesis. Here, we discussed the importance of multifunctional materials and their possible impact on the advancement of next generation technologies. A general focus is given to the class of magnetoelectric materials which simultaneously show ferroelectricity and magnetic ordering (ferromagnetic, antiferromagnetic).

Chapter 2 (Theoritical Foundations) gives an overview of all the physical concepts essential to understand the magnetic and electrical phenomenon related to the candidate materials used in this thesis. The first section showcases the perovskite structure, the origin and consequences of crystal field splitting. The next two sections discuss magnetism in solids and various magnetic interactions in octahedrally coordinated transition metal oxides. The last two sections are dedicated to the discussion of electrically polarised materials, their classification based on the crystal symmetry and effects they exhibit, and the origin of ferroelectricity in perovskite oxides.

Chapter 3 (Pulsed Laser Deposition) highlights the several features of PLD, our major thin film growth method. First a brief outline of the Laser ablation process is presented followed by the mechanism and thermodynamics of epitaxial thin film growth. The final sections are from an experimental point of view that discuss the control parameters of PLD growth, advantages and a short description of the experimental setup used for thin film deposition.

Chapter 4 (Characterisation Techniques) outlines the basic principles of various characterisation (structural and magnetic) techniques employed for the work presented in this thesis (Reflection High Energy Electron Diffraction, X-Ray Diffraction, X-Ray Reflectivity, Atomic Force Microscopy and Superconducting Quantum Interference Device Magnetometry).

Chapter 5 (Growth of Ferroelectric $\mathbf{Ba_{0.8}Sr_{0.2}TiO_3}$ (001) Thin Films) presents a complete discussion on the growth, structural characterisation and investigation of ferroelectric properties of $Ba_{0.8}Sr_{0.2}TiO_3$ thin films. The first part is dedicated to the material synthesis by solid state reaction method, powder XRD characterisation and PLD target preparation. Next, the complete thin film growth process is presented along with the structural characterisation data. Finally the experimental outcomes related to the ferroelectric characterisation of the developed thin films are discussed.

Chapter 6 (Growth, Structure and Magnetic Properties of $\mathbf{La_{0.7}Sr_{0.3}MnO_3}$ (001) Thin Films) presents the growth, characterisation (by XRD, XRR), surface imaging (by Atomic Force Microscopy) and SQUID magnetometry of the developed $La_{0.7}Sr_{0.3}MnO_3$ thin films.

Chapter 7 (Growth and Characterisation of $\mathbf{Ba_{0.8}Sr_{0.2}TiO_3/La_{0.7}Sr_{0.3}MnO_3}$ (001) Heterostructure) discusses the growth of the composite magnetoelectric $Ba_{0.8}Sr_{0.2}TiO_3/La_{0.7}Sr_{0.3}MnO_3$ heterostructure and its structural characterisation followed by the discussion on the obtained data from a growth point of view.

Chapter 8 (Conclusion and Future Prospects) wraps up the thesis with a general conclusion and future prospects of the project.

Chapter 2

Theoritical Foundations

This chapter discusses the key physical concepts necessary to understand the origin and principles of magnetism and ferroelectricity in transition metal oxides.

2.1 The Perovskite Structure

Perovskite oxides have a general chemical formula ABO_3, where A and B represent a metal cation or mixture of two or more such elements or vacancies. The physical properties of the entire family are extremely diverse: depending on the composition and cationic ordering, they can be metallic or insulating and exhibit many different types of structural and magnetic order. It is a well known fact that the perovskite structure can accommodate over 90% of the natural metallic elements found in the periodic table [24].

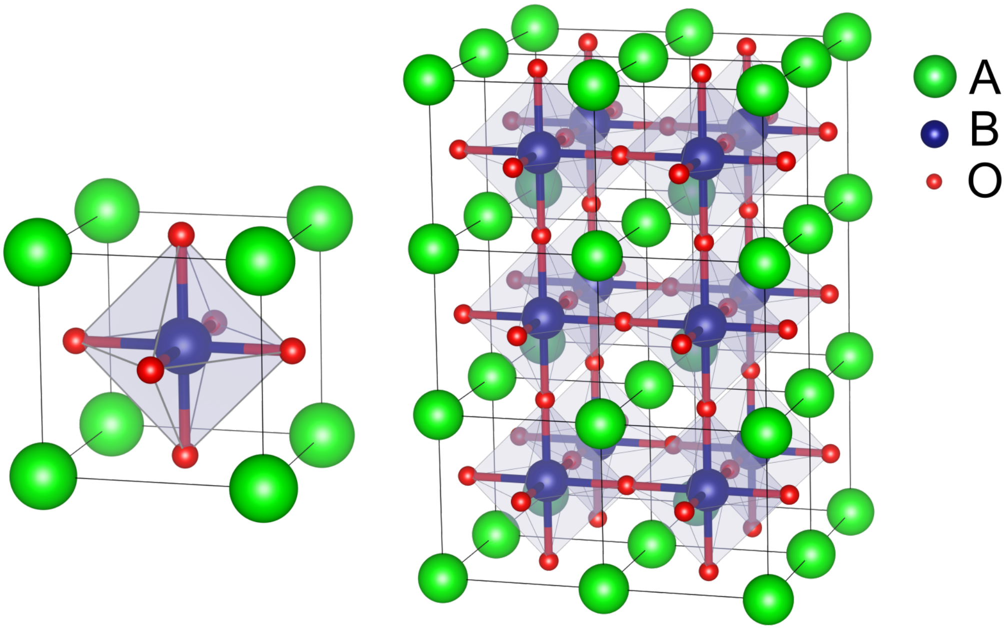

Figure 2.1: Single perovskite unit cell and an extended lattice.

The ideal perovskite structure, has space group $Pm3\bar{m}$ in the Hermann–Mauguin notation. As shown in Fig. 2.1, if the A atom is taken at the corner of the cube, the B atom is at the center surrounded by 6 oxygen atoms situated at the center of each face arranged in a regular octahedron. In the extended lattice it can be observed that each A atom is surrounded by 12 equidistant O atoms.

2.1.1 Crystal Fields

The first step in understanding the magnetic properties of Transition Metal Oxides (TMO) is to examine how interactions with neighboring ions alter the configuration of partially filled d orbitals. These interactions are modeled within the framework of *Crystal Field Theory* (CFT). CFT describes the lifting of the 5-fold degeneracy of the d orbitals of positively charged TMO ions due to electrostatic interactions with the negatively charged non-bonding electrons of the surrounding oxygen atoms.

As discussed before, in a perovskite structure, the transition metal ion is located at the center of a cube surrounded by six oxygen atoms, forming an octahedral environment. There are five different d orbitals: d_{xy}, d_{yz}, d_{zx} which point between the x, y and z axes and $d_{3z^2-r^2}$ orbital with lobes pointing along the z axis, the $d_{x^2-y^2}$ orbital with lobes pointing along the x and y axes. CF originates from an electrostatic interaction of these d orbitals with the $2p$ orbitals of the neighbouring oxygen atoms.

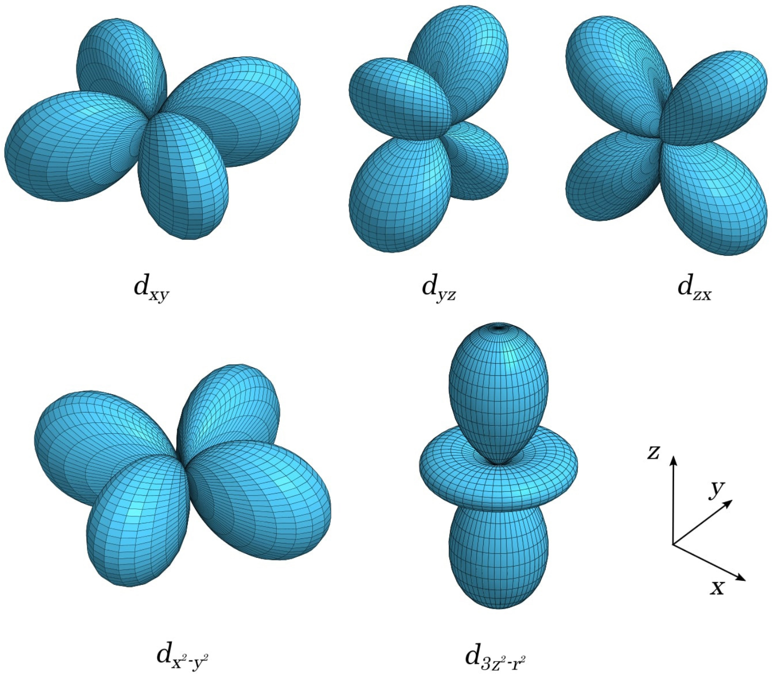

Figure 2.2: The angular distribution of the five d orbitals. The d_{xy}, d_{yz} and d_{zx} are grouped together and are called the t_{2g} levels. The $d_{x^2-y^2}$ and $d_{3z^2-r^2}$ are grouped together and called the e_g levels.

To demonstrate that the environment affects the orbitals in different ways, consider Fig. 2.3 which in three dimensional view shows all the d orbital's orientations in an octahedral environment. The lobes of the $d_{3z^2-r^2}$ and $d_{x^2-y^2}$ orbitals point towards the charges, so the repulsion force is higher. While the lobes of d_{xy}, d_{yz}, and d_{zx} orbitals point away from the oxygen lowering their electrostatic interaction energy.

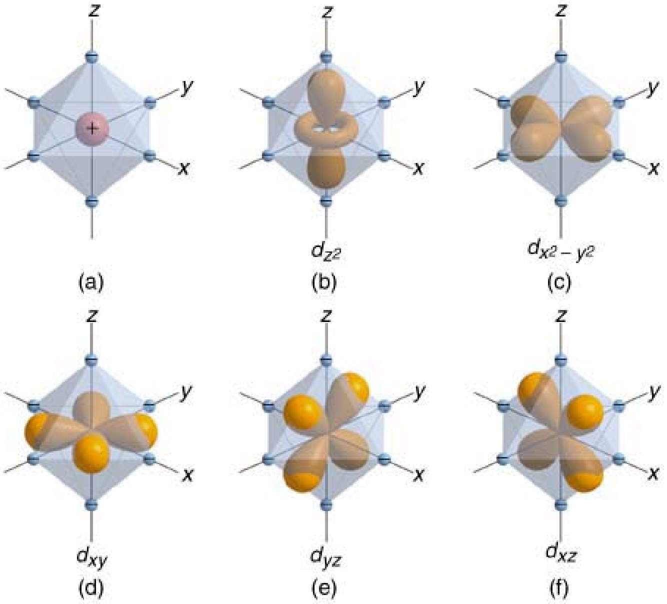

Figure 2.3: (a) The B site metal ion of perovskite oxide in an octahedral environment. (b-f) The orientations of the d orbitals relative to the negatively charged oxygen cations. Notice that the lobes of the $d_{3z^2-r^2}$ and $d_{x^2-y^2}$ orbitals (b and c) point toward the charges. The lobes of the d_{xy}, d_{yz}, and d_{zx} orbitals (d-f) point between the charges.

This overall interaction with the oxygen octahedra breaks the degeneracy of the d levels by raising the energy of the twofold e_g manifold while lowering the energy of the threefold t_{2g} manifold (See Fig. 2.4). The energy difference between these new levels is called *Crystal Field Splitting Energy.*

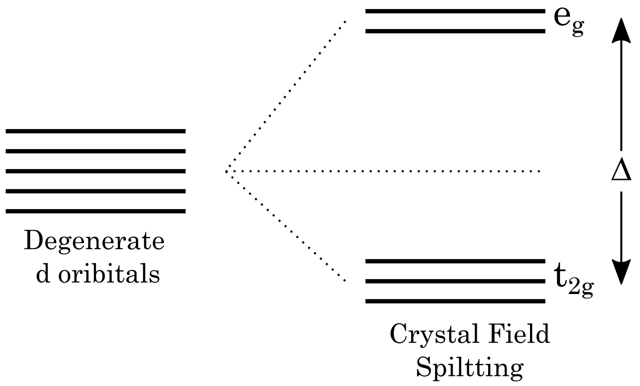

Figure 2.4: The crystal field in an octahedral environment, illustrating the breaking of d orbital degeneracy.

2.1.2 Jahn-Teller Distortion

So far we have only considered the role octahedral symmetry in defining the elctronic structure of TMO's and hence figure out the magnetic properties based on how the electrons fill the energy levels. Sometimes, however, the electronic configuration of certain transition metal ions can further influence the symmetry of the local environment. This geometric distortion is formally called the Jahn-Teller effect. When a transition metal ion in an octahedral state exhibits a spatially degenerate electronic ground state, it will undergo a geometrical distortion that removes this degeneracy and lowers the overall energy of the species [25].

For a high spin d^4 transition metal oxide such as Mn^{3+}, there is a vacancy in the orbital set e_g, either in the $d_{3z^2-r^2}$ or in the $d_{x^2-y^2}$ orbital. According to Jahn and Teller, this configuration is not stable and the octahedron must reduce symmetry through spontaneous structural distortion (See Fig. 2.5) in a way that there is splitting in the energy levels of both the e_g and t_{2g} orbitals [26]. However we do not see this effect if the e_g orbitals of the ion are either half filled as in a d^5 configuration or completely empty in Mn^{3+} (d^3).

The distortion can be elongative or compressive, and the effects are dictated by the amount of overlap between the transition metal and oxygen orbitals.

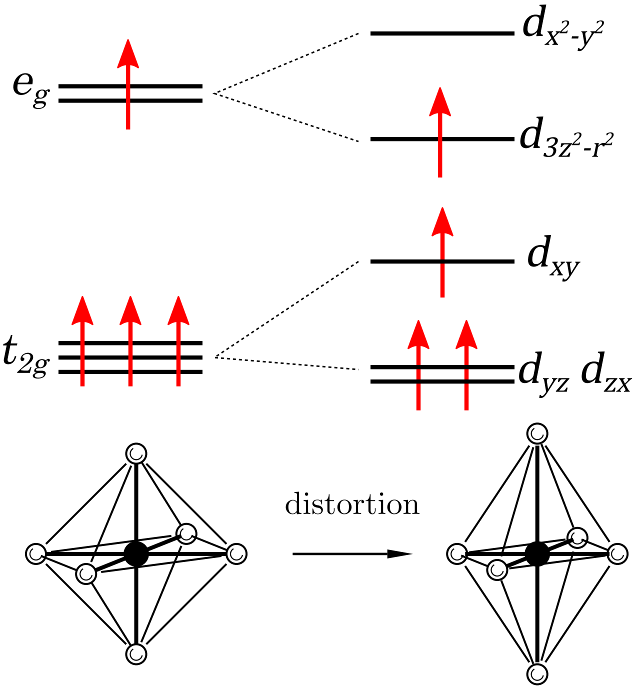

Figure 2.5: The Jahn–Teller effect for Mn^{3+} ($3d^4$). An octahedral complex (left) can distort (right), thus splitting the t_{2g} and e_g levels. The distortion lowers the energy because the singly occupied e_g level is lowered in energy. The saving in energy from the lowering of the d_{zx} and d_{yz} levels is exactly balanced by the raising of the d_{xy} level.

2.2 Magnetism in Solids

2.2.1 Magnetisation and Field

A magnetic material has a large number of atoms, each with their magnetic moments. While it is difficult for us to study the dipole moment associated with all the individual atoms, we define the *Magnetisation* vector; **M** which is the magnetic moment per unit volume. This vector field is considered to be smooth everywhere except at the edges of a solid. For legacy considerations, **B** is defined as *magnetic flux density*, which gives the measure of the number of magnetic field lines crossing per unit area; *magnetic field strength* is represented by **H**. The former is measured in Tesla (T), while the latter in Am^{-1}.

In free space **B** and **H** are just scaled versions of each other, as there is no magnetisation. Both vector fields are related by:

$$\boldsymbol{B} = \mu_0 \boldsymbol{H} \tag{2.1}$$

where $\mu_0 = 4\pi \times 10^{-7}\ \mathrm{Hm}^{-1}$ is *permeability of free space.* In a magnetic solid, the relation between **B** and **H** is more complicated due to the presence of magnetisation. The general vector relation is

$$\boldsymbol{B} = \mu_0(\boldsymbol{H} + \boldsymbol{M}) \tag{2.2}$$

A *linear material* is a special case where the magnetisation and the field strength are proportional, and we write

$$\boldsymbol{M} = \chi_m \boldsymbol{H} \tag{2.3}$$

where χ_m is a dimensionless quantity called *magnetic susceptibility.* In this special case, the relation between **B** and **H** is

$$\boldsymbol{B} = \mu_0(1 + \chi_m)\boldsymbol{H} = \mu_0 \mu_r \boldsymbol{H} \tag{2.4}$$

Here $\mu_r = 1 + \chi_m$ is the *relative permeability* of the material.

2.2.2 Magnetic Orderings

The magnetic response of materials is classified into four major groups: *diamagnetic*, *paramagnetic*, $ferromagnetic$, and $antiferromagnetic$.

Diamagnetism is seen in materials whose composite atoms or molecules do not posses a net dipole moment. Being placed in an external field the diamagnetic materials partially expel out the magnetic field lines from the interior of the material, and also produce a magnetisation opposite to the field. For noble gases and insulators, the diamagnetic moment arises because of the Larmor precession of the orbital electrons, which is induced by the applied field. All materials have a diamagnetic component due to the effect of the applied magnetic field upon the inner closed electron shells due to Lenz's Law. The diamagnetic response is usually linear to the applied field and temperature independent. In the classical form, diamagnetic susceptibility can be expressed as

$$\chi_m = -\frac{\mu_0 e^2 Z n}{6 m_e} \langle r^2 \rangle \tag{2.5}$$

Paramagnetic materials have a weak response to an applied external magnetic field. This magnetic moment arises from the presence of atoms or ions with unpaired electrons, but they lack long-range order. The unpaired electrons posses a magnetic moment, but the interaction of the moments is too weak to overcome the randomised demagnetizing influence of thermal motion. Application of an external magnetic field caused the randomised dipole moments to align in the direction of the applied magnetic field, giving rise to a small positive magnetisation.

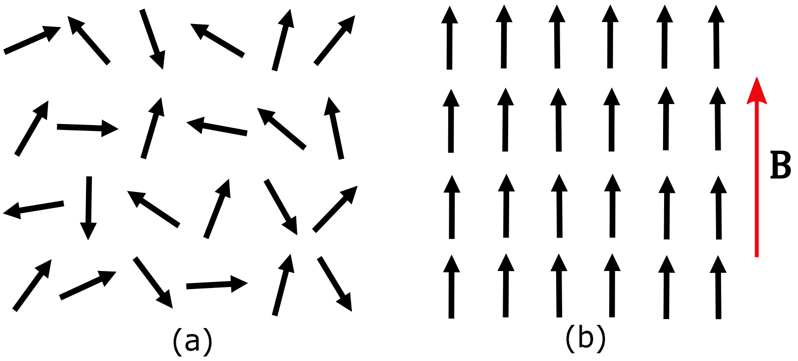

Figure 2.6: (a) Randomly oriented Paramagnetic spins of a material in absence of an external magnetic field. Thus no net magnetisation is observed in this case. (b) Upon the application of an external field **B** all the moments align themselves in its direction giving rise to a small positive magnetisation. As soon as the field **B** will be removed the spins will go back to some random configuration similar to (a).

At low fields, the approximate susceptibility of paramagnetic materials is given by the Curie law.

$$\boldsymbol{M} = \frac{C}{T}\boldsymbol{H} = \chi_m \boldsymbol{H} \tag{2.6}$$

Here, the susceptibility $\chi_m = C/T$, showing that susceptibility decreases with increasing temperature. C is called the *Curie's Constant* named after Pierre Curie. The value of C is dependent on the individual magnetic moments of the atom,

$$C = \frac{n}{3k_B}\mu_{\text{eff}}^2 \tag{2.7}$$

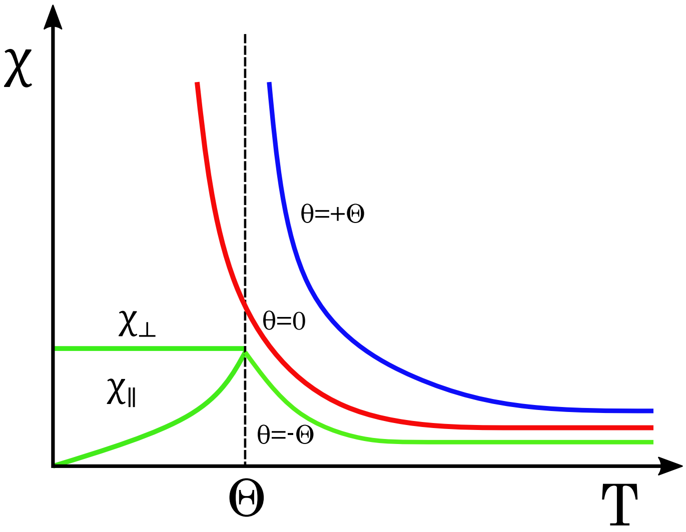

Figure 2.7: The Curie Weiss Law states that $\chi \propto 1/(T-\theta)$ for $T > \theta$. The magnetic susceptibility as a function of temperature is shown in this figure for Paramagnetic (Red), Ferromagnetic (Blue) and Antiferromagnetic (Green) materials.

Ferromagnetism is the simplest ordered magnetic state. The unpaired electrons are present, as in paramagnetic materials, but in this case there are interactions between the moments that serve to align them even if there is no applied magnetic field. These interactions are strong enough to yield a cooperative alignment of magnetic moments, creating an internal 'molecular field'. This results in the presence of magnetisation even in the absence of an external magnetic field. The interaction between local moments is strong in a ferromagnet, but it cannot counteract the disordering effects of temperature indefinitely. Above the Curie temperature, the thermal energy destroys the alignment of the magnetic moments of the ferromagnetic material and behaves as a paramagnet. In this regime susceptibility has the following $Curie-Weiss$ form,

$$\chi_m = \frac{C}{T-\theta_C} \tag{2.8}$$

For an antiferromagnetic material, half of the magnetic moments are aligned in one direction, and the other half is aligned in the opposite direction. The ordered magnetic moments can be considered to lie on two sub-lattices. This means that there is no net magnetisation of the antiferromagnetic material. As with the ferromagnetic material, there is a critical transition temperature, which is known as the Néel temperature, T_N. Above this temperature, the magnetic moments are disordered, and the antiferromagnetic material becomes paramagnetic. However, below T_N, there is a net magnetization due to different magnetisations of the two sub-lattices. Hence, this can be used as a magnetic ordering parameter for antiferromagnetic materials. The magnetic susceptibility of an antiferromagnetic material is temperature dependent and it is small and positive at all temperatures. For temperatures above the T_N, the magnetic susceptibility follows the Curie-Weiss law, which is given by

$$\chi_m = \frac{C}{T - \theta_N} \tag{2.9}$$

where θ_N is the Curie-Weiss constant.

2.2.3 Exchange Interactions

Exchange interaction is at the heart of the phenomenon of long range magnetic order which was briefly discussed in last segment. The Heisenberg Model Hamiltonian is the basis of most theoretical studies of magnetism in determining the integral parameter of exchange J_{ij}. These parameters define most of the magnetic properties such as the Curie Temperature (T_C), magnetic response to an external field and magnon dispersion curves [27, 28].

Exchange interactions are nothing more than electrostatic interactions, arising because charges of the same sign cost energy when they are close together and save energy when they are apart. To understand the basic mechanism of exchange interactions, we shall consider the Heitler-London model for the H_2 molecule [29]. Here, we take a very simple system of two electrons with spatial coordinates $\mathbf{r}_1$ and $\mathbf{r}_2$ as shown in Fig. 2.8.

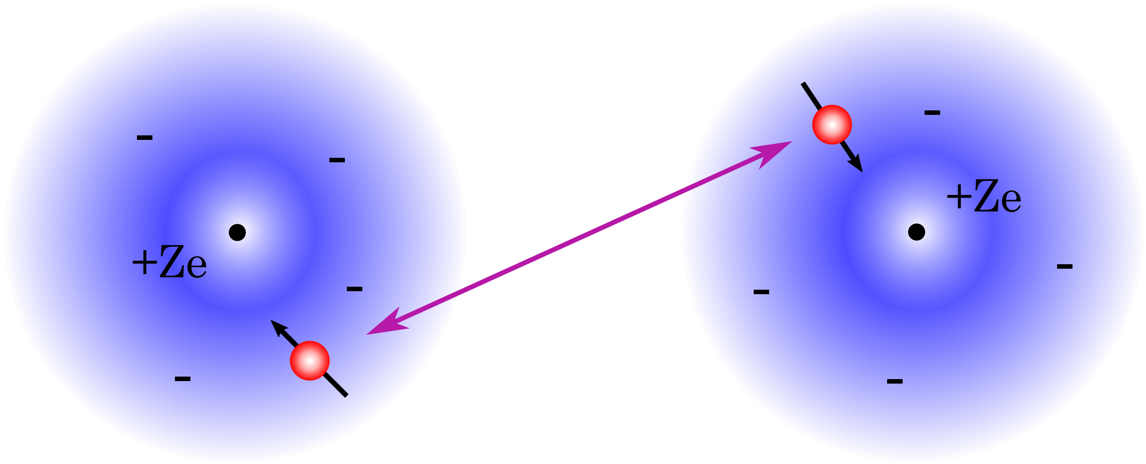

Figure 2.8: Symmetric representation of a two-particle model which illustrates the phenomenon of the direct exchange. Two electrons feel each other through Coulomb interaction between the corresponding electron densities and exchange interaction which appears for indistinguishable fermionic wavefunctions.

Following Pauli's Exclusion Principle, the total wave function of the joint state must be antisymmetric. So, the spin part of the wave function must either be an antisymmetric singlet state χ_S ($S = 0$) in case of a symmetric spatial state or a symmetric triplet state χ_T ($S = 1$) in case of an antisymmetric spatial state. Thus, the wave functions for the singlet and triplet case can be written as

$$\Psi_S = \frac{1}{\sqrt{2}} \left[\psi_a(\mathbf{r}_1)\psi_b(\mathbf{r}_2) + \psi_a(\mathbf{r}_2)\psi_b(\mathbf{r}_1) \right] \chi_S \tag{2.10}$$

$$\Psi_T = \frac{1}{\sqrt{2}} \left[\psi_a(\mathbf{r}_1)\psi_b(\mathbf{r}_2) - \psi_a(\mathbf{r}_2)\psi_b(\mathbf{r}_1) \right] \chi_T \tag{2.11}$$

where both the spatial and spin parts are included in the total wave function. The energy corresponding to these states are

$$E_S = \int \Psi_S^* \hat{\mathcal{H}} \Psi_S d\mathbf{r}_1 d\mathbf{r}_2$$

$$E_T = \int \Psi_T^* \hat{\mathcal{H}} \Psi_T d\mathbf{r}_1 d\mathbf{r}_2$$

It is now possible to separate the spin-dependent part of the energy from the rest. For a singlet state $\mathbf{S_1} \cdot \mathbf{S_2} = -\dfrac{3}{4}$ while for a triplet state $\mathbf{S_1} \cdot \mathbf{S_2} = \dfrac{1}{4}$. Hence, the Hamiltonian can be written in the form of an “Effective Hamiltonian” [30]

$$\hat{\mathcal{H}} = \frac{1}{4}(E_S + 3E_T) - (E_S - E_T)\mathbf{S_1} \cdot \mathbf{S_2} \tag{2.12}$$

The constant $\frac{1}{4}(E_S + 3E_T)$ can be absorbed into other constant energy terms, but the second spin dependent term is more interesting. The *exchange integral*, J is defined by

$$J = \frac{1}{2}(E_S - 3E_T) = \int \psi_a^*(\mathbf{r}_1)\psi_b^*(\mathbf{r}_2)\hat{\mathcal{H}}\psi_a(\mathbf{r}_2)\psi_b(\mathbf{r}_1) d\mathbf{r}_1 d\mathbf{r}_2 \tag{2.13}$$

Hence, the effective spin Hamiltonian can be simply rewritten as

$$\hat{\mathcal{H}}^{\text{spin}} = -2J\mathbf{S_1} \cdot \mathbf{S_2} \tag{2.14}$$

If $J > 0$, $E_S > E_T$ and the triplet state $S = 1$ is favorable, while for $J < 0$, $E_S < E_T$ the singlet state $S = 0$ is favoured. This equation is relatively simple for two electrons, but generalizing it to a many-body system is far from trivial. However, this equation can still be applied to atoms in real materials leading to the Heisenberg model

$$\hat{\mathcal{H}} = -\sum_{ij} J_{ij} \mathbf{S_1} \cdot \mathbf{S_2} \tag{2.15}$$

where J_{ij} is the exchange interaction factor between the i^{th} and j^{th} spins.

2.2.4 Direct and Indirect Exchange

If electrons on the neighbouring atoms interact via an exchange interaction, this is known as *direct exchange*. This is because the exchange proceeds without the need for an intermediary. A direct exchange is also known as the dipole–dipole magnetic exchange interaction. Although it seems the most obvious route for interaction mechanism to happen, the energy of this kind of interaction is extremely small, of the order of $\sim 10^{-23}$ J, it is too weak to be responsible for magnetic ordering above 1 K.

When the magnetic moments are separated by a relatively large distance, then they cannot be coupled through direct exchange interaction. In this situation, the exchange interaction can occur indirectly through intermediaries. A number of indirect exchange mechanisms can interpret the magnetic coupling of many magnetic oxides. We shall discuss these effects in detail in the upcoming section.

2.3 Magnetic Properties of Transition Metal Oxides

2.3.1 Superexchange

In this type of interactions, non-neighbouring magnetic cations are mediated via a non-magnetic anion. Such interactions occur, for example, in transition metal oxides [31]. The super-exchange interaction contains a virtual transfer of two electrons simultaneously; resulting in the formation of an excited state. When a $2p$ electron of the oxygen transfers to neighbouring metal ion, the unpaired p electron of oxygen then enters into direct exchange with the other metal ion. The sign of the magnetic ordering is then determined by the relative orientation of the spin of the virtually transferred oxygen with respect to the first metal ion and the sign of the direct exchange between the oxygen and the second metal ion.

Superexchange being a second order process, the involved energy is approximately given by the square of the matrix element of the transition divided by the energy cost of making the excited state. The transition matrix is controlled by the hopping parameter t_{ij}, which is proportional to the bandwidth in a simple tight binding approach [32]. The energy cost of making an excited state is given by the Coulomb energy, U. By using second order perturbation theory, it can be shown that $J \propto -t_{ij}/U$ in superexchange interactions. As discussed previously, d orbitals can have different orientations and overlap configurations with respect to the oxygen orbitals; thus different types of superexchange interactions can take place, antiferromagnetic (AFM) or ferromagnetic (FM).

Antiferromagnetic Superexchange

In the case of a 180° bond angle between transition metal and oxygen, the antiferromagnetic ordering has a kinetic energy advantage. To understand this we shall refer to Fig. 2.10 (a), which shows two transition metal ions separated by an oxygen ion.

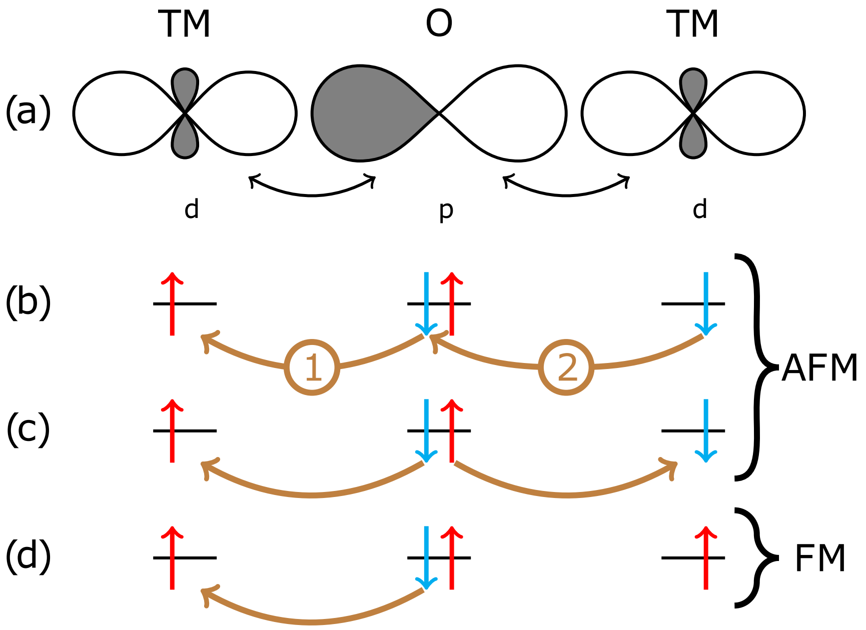

Figure 2.9: A schematic representation (a) of the two TM orbitals and intermediate O orbital involved in superexchange with a 180° bond angle. (b) and (c) correspond to the two virtual hopping processes in the case of AFM order on the TM sites, whereas for FM ordering only (d) is possible.

For simplicity we shall consider the single occupation of d orbitals and the double occupation of the p orbitals. In case of an AFM ordering, two different hopping processes may happen. First, an electron from the p orbital can hop to a d orbital followed by a second hop from the other d orbital to p orbital as is shown in Fig. 2.10 (b). In addition, both the p electrons can also hop to their respective d orbital as in Fig. 2.10 (c). This permits the system to lower its energy by allowing these electrons to become delocalised over the whole structure, thus lowering the kinetic energy.

Ferromagnetic Superexchange

In some circumstances superexchange favours FM ordering. For example when we consider a situation as shown in Fig.2.10 where by symmetry, hopping is only permitted between adjacent d and p orbitals.

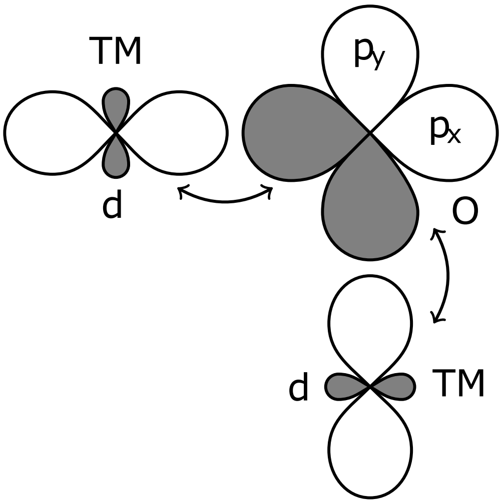

Figure 2.10: A schematic representation of ferromagnetic superexchange for a TM-O-TM configuration. The electrons in the p_x and p_y orbitals can hop only to the adjacent d orbitals.

This is generally seen in low Z transition metal oxides systems with cubic symmetry, where t_{2g} states are partially filled while e_g states are empty. Hence, the hybridization with oxygen is relatively small (because t_{2g} orbitals point away from the 2_p oxygen orbitals). As a result, ferromagnetic superexchange interaction becomes quite weak.

Goodenough-Kanamori-Anderson Rules

The theoretical foundations of electron hopping between the orbitals is based on these principles [33],

1. The spin angular momentum is conserved in an electron transfer, virtual or real.
2. The Pauli exclusion principal restricts electron transfer from a half-filled to a half-filled orbital or two-electron transfer from the same anion-p orbital.
3. The intra-atomic spin-spin potential exchange interaction is ferromagnetic and is determinative where the Pauli exclusion principle is not restrictive.

The so-called rules for superexchange in transition metal oxides in are codified in papers by Goodenough [34, 35], Kanamori [36], and Anderson [37] and are thus collectively known as the GKA rules and we can summarise the above classification of superexchange interaction as follows:

i. When two cations have lobes of magnetic orbitals (i.e. singly occupied d orbitals) pointing towards the same anion p orbital, there is a reasonably large overlap. The super-exchange interaction is then strong and favours AFM ordering to satisfy the Pauli exclusion principle. This interaction is known as antiferromagnetic super-exchange where the TM-O-TM bond angle is 180°.

ii. When the magnetic orbitals of two cations couple to different p orbitals, then there is no overlap by symmetry. Thus, it is not possible for an electron from the d orbital on one side to reach the d orbital on the other side. The super-exchange interaction in this case is FM and relatively weak; this is known as ferromagnetic super-exchange where the TM-O-TM bond angle is 90°.

These two rules explain the superexchange interactions in almost all the possible spin arrangements that are encountered real life compounds. Antiferromagnetic superexchange mechanism can only arise between two orbitals having a finite transfer integral t_{ij} connecting them. In other words, the two orbitals must have the same symmetry in the region of overlap. If the orbitals do not have the same symmetry such that, $t_{ij} = 0$, one expects ferromagnetic exchange based on the GKA Rules [38].

2.3.2 Double Exchange

Double Exchange is essentially a ferromagnetic interaction that takes place in transition metal oxides consisting of mixed valency ions and implies a real transfer of an electron, thus allowing electrical conductivity. This exchange interaction was proposed by Zener [39] in 1951 to explain the ferromagnetism observed in perovskite manganites.

For example we will consider a general doped manganite perovksite $RE_{1\text{-}x}AE_x\text{MnO}_3$ which has mixed valency of manganese ions *i.e.*, Mn^{3+} and Mn^{4+}, where RE is a trivalent rare-earth ion and AE is a divalent alkali-earth ion [40]. The e_g electron on a Mn^{3+} ion can hop to a neighboring site only if there is an empty orbital of the same spin (since hopping proceeds without spin flipping). If the neighbor is a Mn^{4+} ion which has no electron in its e_g shell, this should not present any problem. However, there is a strong intra-atomic exchange interaction between the e_g electron and the three electrons at the t_{2g} level. This interaction corresponds to the first Hund's rule and it wants to keep all spins aligned in the same direction. Thus, it is not energetically favorable for an e_g electron to hop to a neighboring ion in which the t_{2g} spins have antiparallel alignment (antiferromagnetic ordering) to the incoming electron. Therefore, the system aligns ferromagnetically (parallel spin alignment configuration) to save energy.

Zener proposed a mechanism (See Fig. 2.11 (a)) that involves the simultaneous transfer of an e_g electron from one transition metal ion to oxygen ion and from oxygen ion to the other TM ion. The spin of the transferred electron is preserved in this process. Moreover, the ferromagnetic alignment allows the e_g electrons to hop through the crystal and the material becomes metallic. Anderson and Hasegawa [41] in 1955 calculated the hopping parameter t_{ij} for a pair of magnetic ions with generalised spin direction as $t_{ij} = t_0 \cos(\theta_{ij}/2)$; where θ_{ij} is the angle between core spins at sites i and j, and t_0 represents the normal transfer integral that depends on the spatial wave function. Unlike superexchange where $J \propto -t_{ij}/U$, in the double exchange mechanism $J \propto t_{ij}$ [38].

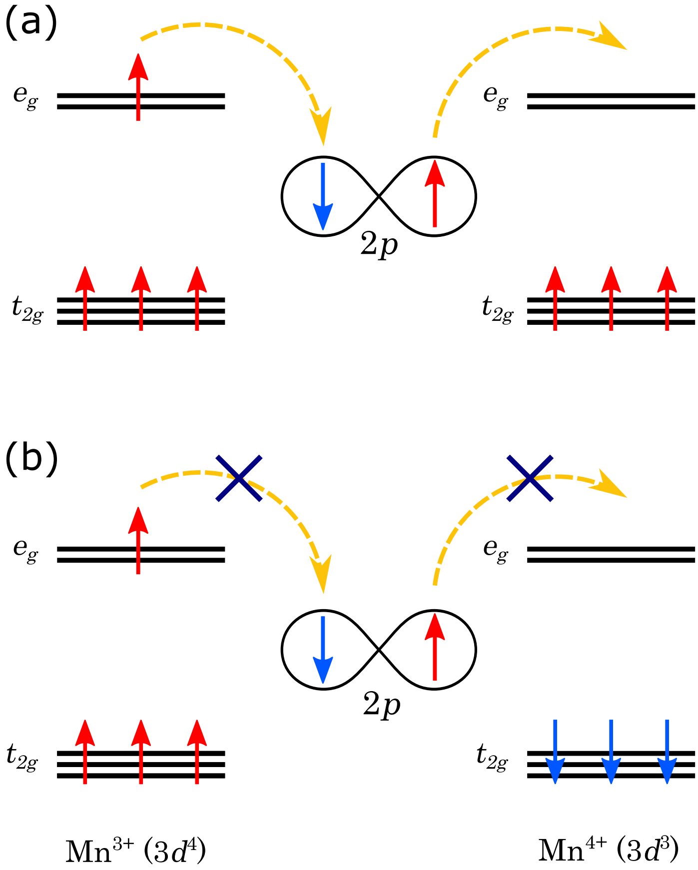

Figure 2.11: Double exchange mechanism gives ferromagnetic coupling between Mn^{3+} and Mn^{4+} ions participating in an electron transfer via the p orbitals of intermediate oxygen. (a) The single centre exchange interaction favours hoping only if the neighbouring ions are ferromagnetically aligned. As shown in (b) this hopping is not energetically favorable if they are antiferromagnetically aligned.

2.3.3 RKKY Interaction

This interaction occurs when there are both localised and band electrons. In rare-earths, for example, the observed magnetisation was found to be due to the 4f electrons. However, since these electrons are strongly localised, there is no direct interaction. Instead, the interaction between the localised magnetic moments of the $4f$ shell is obtained through the electrons in the $5d$ or $6s$ conduction band. This is known as the Ruderman, Kittel, Kasuya and Yosida (RKKY) interaction interaction and is used to interpret the resulting magnetism in metals.

The mechanism of this interaction depends on polarising the delocalised (itinerant) conduction electrons by a localised magnetic moment; this polarisation in turn interacts magnetically with the neighbouring localised magnetic moment that is located at a distance r from the first magnetic moment [42, 43].

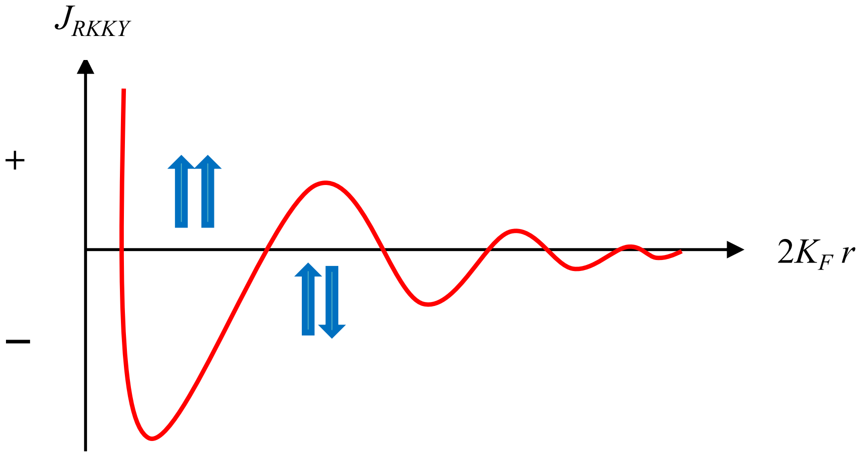

Figure 2.12: Schematic diagram of the RKKY indirect ferromagnetic/antiferromagnetic exchange interactions depending on the interatomic distance r.

RKKY is a long-range interaction compared to the direct exchange interaction. The main feature of this interaction is the oscillatory behaviour that varies its sign depending on the distance between the interacting magnetic moments. Thus, the resulting RKKY interaction can be either ferromagnetic or antiferromagnetic, as shown in Fig. 2.12 , where K_F is the Fermi wave vector [44].

2.4 Electrically Polarised Materials

This section provides an overview of electrically polar materials and their division based on the various properties they exhibit.

2.4.1 Symmetry and Physical Properties

In general, all materials undergo a small change in dimension when subjected to an external force, such as an applied electric field, a mechanical stress, or a change in temperature (application of heat). Depending on the crystal structure of the material under consideration, such small changes in dimension may result in a change in the internal electric polarization and hence give rise to the occurrence of the phenomenon such as ferroelectricity, piezoelectricity, or pyroelectricity. It can be imagined that materials exhibiting these effects must be polar and have an electrical order, implying these effects are strongly dependent on the crystal geometry.

In a crystal, symmetry arguments are used to describe the presence or absence of certain physical properties. On the basis of translation and orientation there are 230 space groups. If we ignore the translational repetitions we can break down these 230 space groups into 32 point groups, which are based on orientational symmetry only. Theese 32 point groups make subdivisions of seven basic crystal classes, which are based on the degree of symmetry. In the order of ascending symmetry, these seven basic crystal systems are triclinic, monoclinic, orthorhombic, tetragonal, trigonal (rhombohedral), hexagonal, and cubic. The detailed description on these crystal systems and their symmetry condiderations are well documented in the literature [45, 46]. Of the 32 classes (or point groups), 11 classes are centrosymmetric and 21 classes are noncentrosymmetric, possessing no center of symmetry. These noncentrosymmetric are of our interest as they are non polar and thus posses a finite polarisation or dipole moment. The relationship between polar behaviour and crystal symmetry is explained in a compact form in Fig. 2.13.

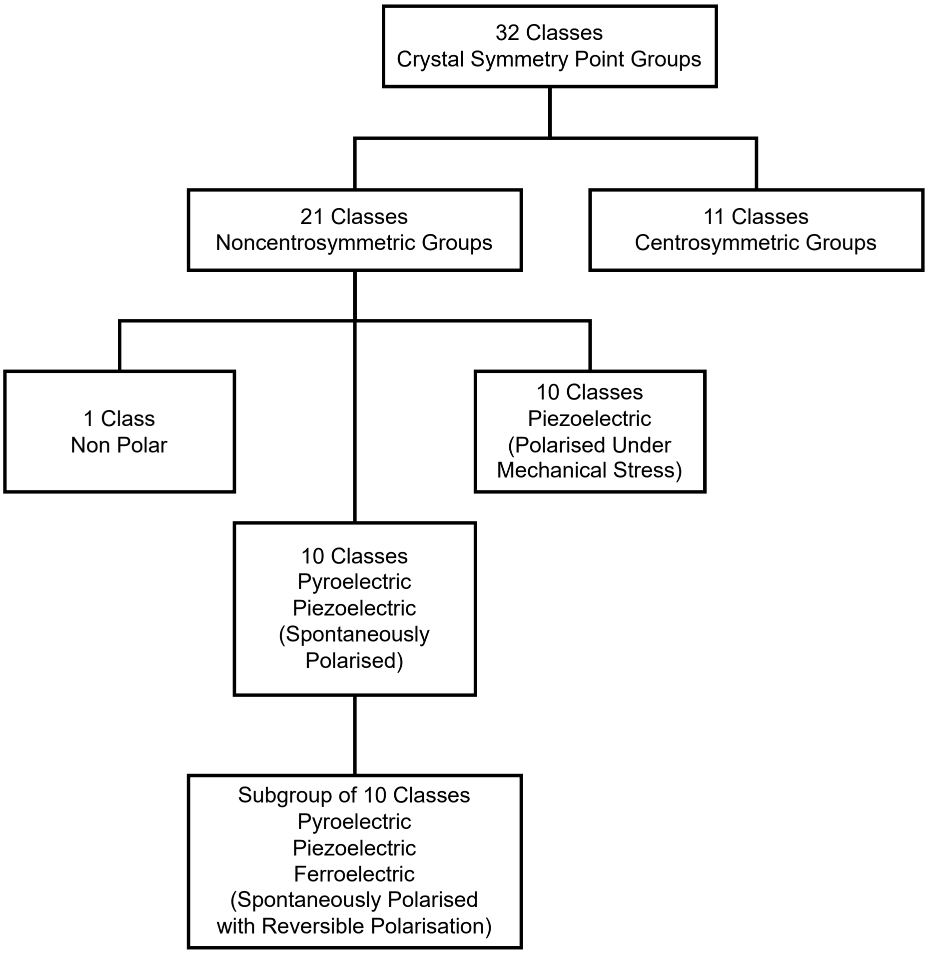

Figure 2.13: Hierarchy of materials based on crystal structure, with special focus to electrically polarised materials.

2.4.2 Macroscopic Polarisation

When an external electric field is applied to a dielectric material it causes the displacement of bound charges. Positive charges are displaced in the direction of the field, and negative charges are displaced opposite to the direction of the field. *Polarisation* **P**, is defined as the dipole moment generated per unit volume of the material.

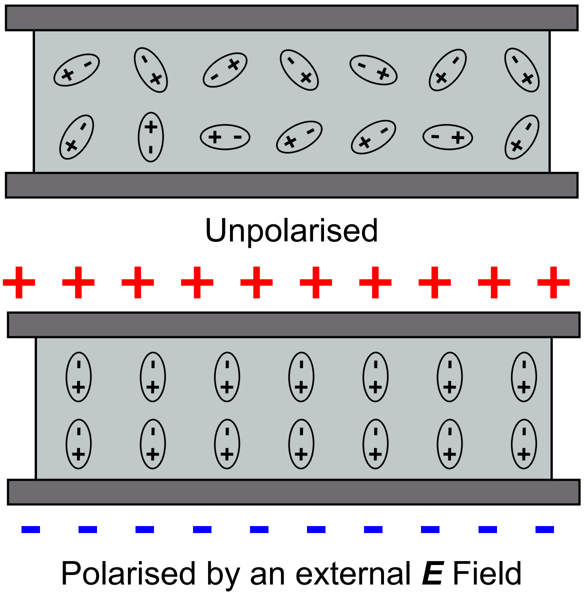

Figure 2.14: An illustration of electric polarisation phenomenon and behaviour of bound charges in absence and presence of an external electric field.

Similar to magnetic susceptibility, we can also define a term *electrical susceptibility*, χ_e, which is a dimensionless constant of proportionality that indicates the degree of polarisation of a dielectric material in applied electric field. Higher electric susceptibility indicates the ease of polarising a material in response to the field.

$$\mathbf{P} = \epsilon_0 \chi_e \mathbf{E} \tag{2.16}$$

The above equation relates the polarisation to the applied field. The susceptibility of a medium is related to its relative permittivity ϵ_r by

$$\epsilon_r = 1 + \chi_e \tag{2.17}$$

The *electric displacement* can be written in terms of electric field and polarisation as

$$\mathbf{D} = \epsilon_0 \mathbf{E} + \mathbf{P} \tag{2.18}$$

Using Eqn. 2.16 and 2.18 we can write

$$\mathbf{D} = \epsilon_0 (1 + \chi_e) \mathbf{E} = \epsilon_0 \epsilon_r \mathbf{E} \tag{2.19}$$

2.4.3 Piezoelectric Materials

Piezoelectric effect implies that under the application of mechanical stress to the crystal specimen creates an overall polarization and developing a voltage across the material. Reversing the direction of stress causes polarity reversal. The piezoelectric effect is reversible, which means that an external electric field will generate mechanical strain in the crystal depending on the direction of the applied field.

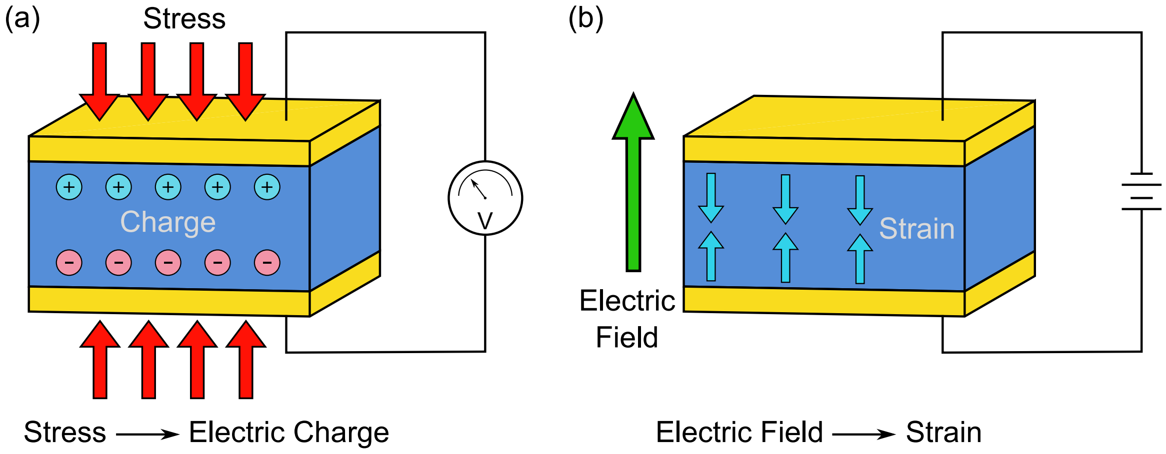

Figure 2.15: An illustration of direct and converse piezoelectric effect. We can observe in that the direct piezoelectric effect provides an electric charge upon application of a mechanical stress (a), whereas in the converse piezoelectric effect describes the situation where strain develops under an applied electric field (b).

In direct piezoelectric effect, the charge density, D_i has a linear relation with the applied stress, σ_{jk}, which is written as

$$D_i = d_{ijk}\sigma_{jk} \tag{2.20}$$

Here, d_{ijk} is the *piezoelectric coefficient tensor*. In the converse piezoelectric effect, an external strain, x_{ij} developes in respose to an applied electric field, E_k by the following relation.

$$x_{ij} = d^{*}_{ijk}E_k \tag{2.21}$$

Here, d^{*}_{ijk} is the *converse piezoelectric coefficient tensor*. In uniform field approximation both the coupling coefficients are equal as the consequence of the existence of thermodynamic potential [47].

2.4.4 Ferroelectric Materials

Ferroelectric phenomena is a sub-class of piezoelectric behaviour, thus all ferroelectric materials exhibit piezoelectric properties. It is one of the most fascinating properties of dielectric solids. Materials exhibiting ferroelectric properties must be either single crystals or polycrystalline solids composed of crystallites. To be classified as a ferroelectric a material it must posses reversible spontaneous polarisation, and so a non-reconstructive transition between two stable states of opposite polarisation must be accessible at known experimental fields.

The ferroelectric polarisation shows a nonlinear response to external fields, unlike most of the piezoelectric. Furthermore the polarisation is dependent not only on the electric field but also on its history that the material has experienced, thereby yielding a hysteresis P-E (Polarisation–Electric Field) loop, as shown in Fig 2.16.

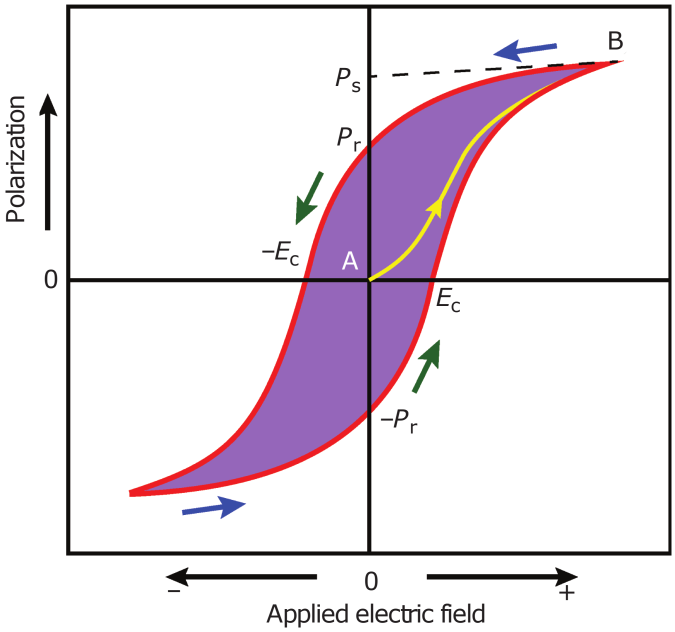

Figure 2.16: A typical Polarisation Vs. Electric Field hysteresis loop observed in ferroelectric materials.

Starting from point A, the polarization initially increases slowly with E-field, but turns to a sharp rise when the applied field is sufficiently high. Then, after a long and slow stage, the polarisation reaches a saturation level (saturation polarisation, P_s). P_s is normally estimated by intersecting the polarization axis with the saturated linear part. The polarization does not go back to the starting point after the removal of E-field but instead results into non-zero values, which is defined as the remnant polarization, P_r. In order to reach a zero polarisation state, an E-field must be applied along the opposite direction. This E-field is named as the coercive field, E_c, which is magnitude of the electric field necessary to reverse the direction of polarisation.

2.5 Ferroelectricity in Perovskite Oxides

2.5.1 Lowering of Crystal Symmetry

As discussed in Sec. 2.1 the ideal structure of a perovskite oxide can be represented as a simple cubic structure. However, the real structures of most perovskites deviate from the ideal simple cubic unit cells. Structural frustrations which lower the symmetry of the crystal are induced through rotations and tilting of the BO_6 oxygen octahedra [48, 49].

Goldschmidt in 1926 put forward an empirical criterion for the stability of the perfect perovskite-type structure [50]. His model is based on the concept of ionic radius and the following rules:

i. A cation will be surrounded by as many anions as can touch it and not more than that.

ii. All the anions must touch the cations and the anion–cation distance is obtained as the sum of their ionic radii.

The end structure is fully determined by the size of the oxygen octahedra containing the B atoms, while the A atoms fit the holes between the octahedra. Following the above rules the ideal relation between the ionic radii is given by:

$$r_A + r_O = \sqrt{2}(r_B + r_O) \tag{2.22}$$

Here the subscript represents the radii of the respective ions in an cubic ABO_3 structure. The deviation from the ideal structure is measured through a tolerance factor t defined as follows:

$$t = \frac{r_A + r_O}{\sqrt{2}(r_B + r_O)} \tag{2.23}$$

When $t < 1$, the A atom is small in comparison to the hole between the oxygen octahedra: the A atom cannot effectively bond with all 12 neighboring O atoms. Giving rise to an orthorhombic structure. While for $t > 1$, the structure is imposed by the A–O distance and the B atom is too small for the oxygen octahedron so that the structure will develop a small polar distortion which causes the system to crystallise in a tetragonal geometry.

Figure 2.18 shows the typical structures of perovskite oxides on the basis of Goldschmidt tolerance factor t.

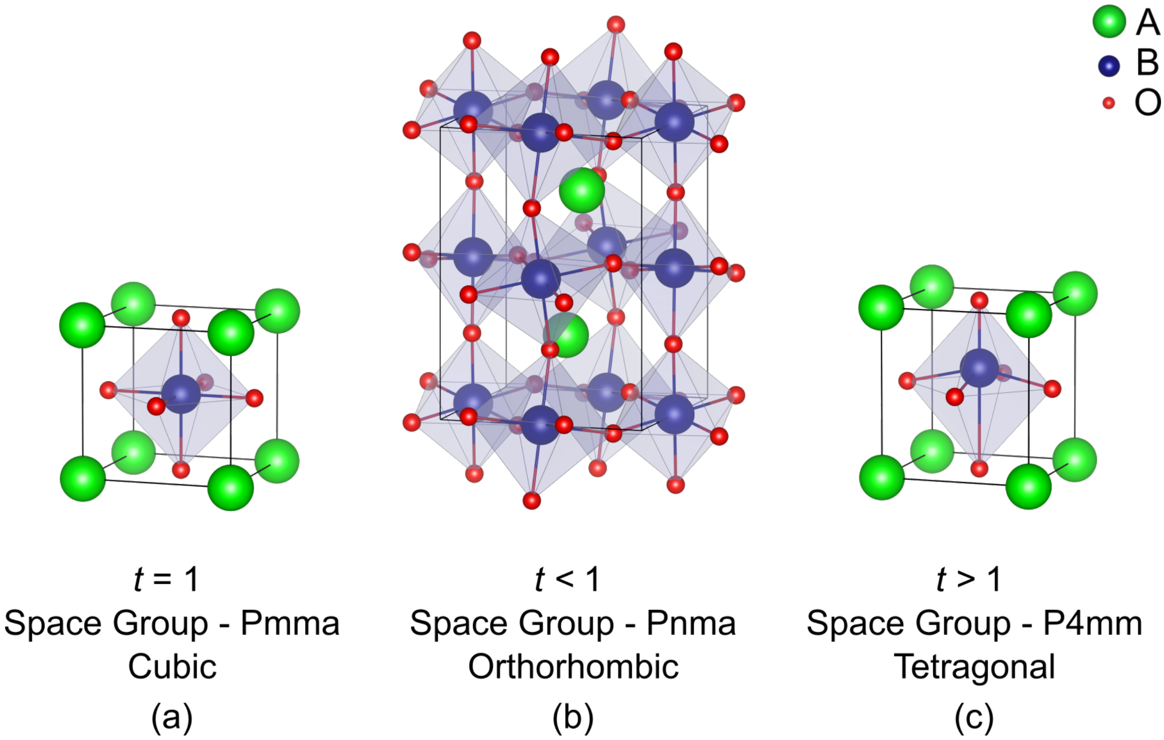

Figure 2.17: Illustration showing the typical crystal structures of perovskite oxides based on the Goldschmidt tolerance factor. (a) Ideal Cubic structure for $t = 1$; (b) Orthorhombic structure for $t < 1$; (c) Tertragonal structure for $t > 1$.

2.5.2 Landau-Devonshire Theory of Ferroelectric Phase Transition

Similar to ferromagnets, ferroelectric materials lose their intrinsic polarisation at temperatures above a transition temperature and become paraelectric. Above the transition temperature the electrical susceptibility, χ_e, of the substance follows the law

$$\chi_e = \frac{C_e}{T - T_C} \tag{2.24}$$

This has same form of expression as the Curie Weiss susceptibility of ferromagnets.

The first successful phenomenological model to explain the phase transition in ferroelectric was the soft mode picture [51]. Soft mode concept is based on the assumption that the crystal gets unstable against a particular normal vibration of the lattice (phonon). In the high temperature paraelectric phase there exists a certain unstable phonon (the "soft mode") whose frequency deceases upon approaching T_C and becoming zero at T_C. This means that the correspondent vibration (or the atomic positions) become "frozen" at this temperature and produce a structure of modified symmetry with a permanent dipole moment.

The soft mode picture of ferroelectric phase transition can be explained by the

Landau-Devonshire theory [52, 53]. We expand the free energy energy density $\mathcal{F}$ in terms of polarisation P of the ferroelectric material in the paraelectric(unpolarised) phase [54]

$$\mathcal{F} = \frac{1}{2}aP^2 + \frac{1}{4}bP^2 - EP \tag{2.25}$$

For a second order phase transition, we assume $b > 0$ [55]. Minimising $\mathcal{F}$ over P we obtain the following relation

$$E = aP + bP^3 \tag{2.26}$$

From this we determine the inverse susceptibility as

$$\chi_e^{-1} = \left.\frac{\partial E}{\partial P}\right|_{P=0} = a \tag{2.27}$$

In the soft mode picture of a second order phase transition the quadratic term in $\mathcal{F}$ changes from $a > 0$ to $a < 0$ as the unpolarsied phase is cooled below T_C. So, a can be written as a function of temperature T as $a = a_0(T - T_C)$. Thus, we have the ferrolelectric susceptibility of the form

$$\chi_e = \frac{a_0^{-1}}{T - T_C} \tag{2.28}$$

which demonstrates the Curie-Weiss divergence of χ_e at the transition temperature.

2.5.3 Second Order Jahn Teller Distortion

The soft mode picture only offers a macroscopic view of phase transition. It fails to provide an atomistic explanation for why the off center shifting of the B cation occurs within the oxygen octahedra in terms of the chemistry of the B cation. The theoretical framework to understand the microscopic origin of the polarization is called the second order Jahn-Teller effect (SOJT) [56]. This effect is associated with the movement of cation species with d^0 configuration on the B site (e.g. Ti^{4+}, Nb^{5+}) and/or $6s^2$ lone-pair configuration on the A site (e.g. Pb^{2+}, Bi^{3+}), which form strong covalent bonds with the surrounding oxygen anions [57].

We take the example of BaTiO_3 where Ti atom has a d^0 configuration. The small amplitude of the Ti^{4+} cation off-centering, Q is treated as a perturbation from the $Pm\bar{m}3m$ energy surface [58].

We can then expand the perturbed Hamiltonian, $\mathcal{H}$ as

$$\mathcal{H} = \mathcal{H}_0 + \left(\frac{\partial \mathcal{H}_0}{\partial Q}\right) Q + \frac{1}{2}\left(\frac{\partial^2 \mathcal{H}_0}{\partial Q^2}\right) + \cdots \tag{2.29}$$

Where $\mathcal{H}_0$ is the undistorted cubic Hamiltonian. We label the stationary states and ground state of $\mathcal{H}_0$ as $|\psi_0\rangle$ and $|\psi_n\rangle$ respectively. Expanding the above Hamiltonian using the standard time independent perturbation theory we obtain the first and second order energy contributions as

$$E^{(1)} = Q \langle\psi_0| \frac{\partial \mathcal{H}_0}{\partial Q} |\psi_0\rangle \tag{2.30}$$

$$E^{(2)} = \frac{1}{2} Q^2 \langle\psi_0| \frac{\partial^2 \mathcal{H}_0}{\partial Q^2} |\psi_0\rangle + Q^2 \sum_n \frac{\left|\langle\psi_0| \frac{\partial \mathcal{H}_0}{\partial Q} |\psi_0\rangle\right|^2}{E_0 - E_n} \tag{2.31}$$

The first order term, $E^{(1)}$ is responsible for splitting of e_g and t_{2g} levels of a transition metal ion in an octahedral environment with a spatially degenerate ground state. This is the First Order Jahn-Teller distortion discussed in Sec. 2.1.2.

We focus only on second order correction and write the energy shift associated with it

$$\delta E = \frac{1}{2} k Q^2 + \mathcal{O}(Q^4) \tag{2.32}$$

where k is the effective force constant given by

$$\langle\psi_0| \frac{\partial^2 \mathcal{H}_0}{\partial Q^2} |\psi_0\rangle + 2 \sum_n \frac{\left|\langle\psi_0| \frac{\partial \mathcal{H}_0}{\partial Q} |\psi_0\rangle\right|^2}{E_0 - E_n} \tag{2.33}$$

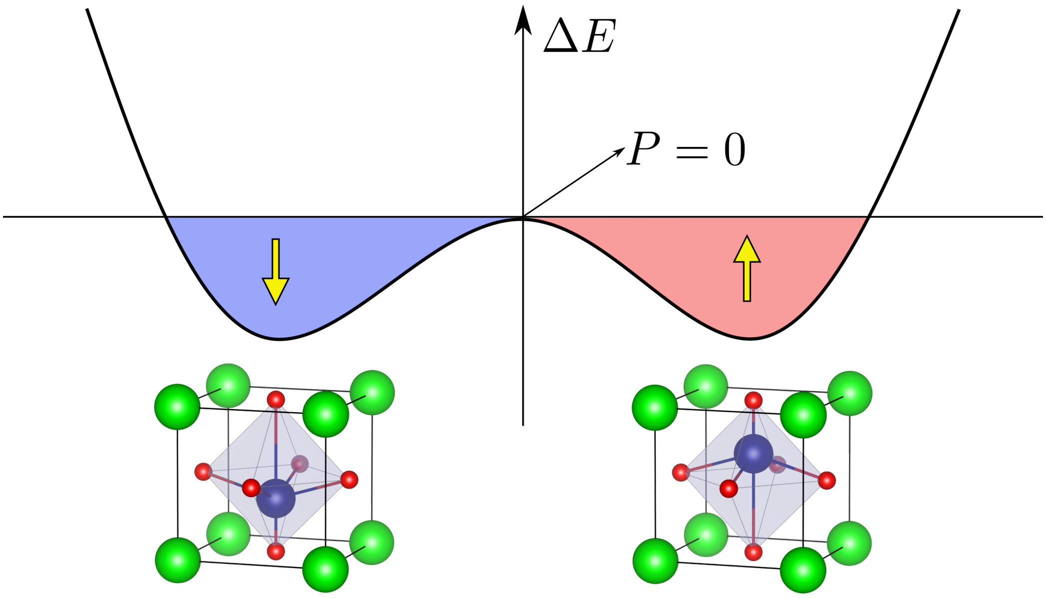

Figure 2.18: Energy Vs. Distortion double well potential of a typical Second order Jahn Teller driven ferroelectric perovskite for a negative value of k. The direction of polarisation is same as that of the non-centrosymmetric shifting of B cation.

For a nondegenerate $|\psi_0\rangle$, the first term in $E^{(2)}$ being positive, corresponds to the increase in coulomb repulsion when the electron clouds from two ions overlap as they are pushed together with the electrons frozen into their original high symmetry configurations, thus being unfavorable for ferroelectricity. The second term which is negative is favorable for ferroelectricity and describes the energy lowering chemical bond formation as the electrons rearrange. Since the distortion Q has odd symmetry with respect to inversion, this term is non-zero when one of the ground and excited electronic states is odd and the other is even, else the integral in the numerator goes to zero. This condition is satisfied in transition metal oxide ions with d^0 configuration, since the valence band is made of odd symmetry oxygen $2p$ states and the conduction band is made of even symmetry transition metal d states. The combination of these two second order terms known as the Second Order Jahn Teller effect determines whether or not a material is ferroelectric.

Chapter 3

Pulsed Laser Deposition

Pulsed Laser Deposition is a method of thin film growth, in which a short-pulsed laser beam is focused onto a target beyond the material's ablation threshold creating a plasma of the target material to expand towards and deposit onto a substrate under vacuum. It is a simple but versatile experimental method that finds use as a means of growth for a very diverse range of materials and in wide areas of thin-film deposition and multilayer research.This ejected material is comprised of ions, atoms, and molecules as it propagates and, upon reaching the substrate, they diffuse on the surface and arrange themselves in one or more crystallographic orientations. This method is excellent for preserving the stoichiometry of complex materials during the deposition process. Since the process involves a high intensity pulsed LASER beam of short pulse width in the order of nano to femtoseconds which is focused on a very small area (few mm^2), the non-equilibrium process of plasma generation allows a great degree of freedom to change various parameters to fabricate desired high quality thin films. This chapter provides a background and short review of the central processes involved in the Pulsed Laser Deposition (PLD) method.

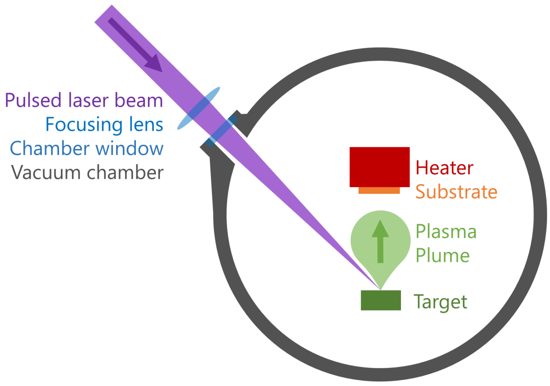

Figure 3.1: A schematic diagram of a PLD system.

PLD as a Non-Equillibrium Process

In thermal deposition techniques for thin film growth, the kinetic energies of the impinging particles are of the order of 0.1 eV. Conceptually, the most simple approach to transport material from the bulk onto a thin film is via thermal evaporation. This process can be understood by relatively simple Maxwell-Boltzmann statistics (where the evaporation is an equilibrium thermodynamic process). However, thermal techniques suffer from the limitation that each degree of freedom in the partition function of a participating chemical system has the same temperature. This leads to a non-stoichiometric transfer of target materials to the substrate, creating unwanted phases in the final thin film. It may be advantageous if one particular energetic degree of freedom can be accessed non-thermally, thus shifting a chemical reaction of interest away from thermal equilibrium [59].

If we consider the case of non-thermal interactions, energy can be selectively transferred via a non-thermal pumping mechanism (Laser or Electromagnetic Fields) into one degree of freedom that is effectively decoupled from the rest of the system. In this way, the activation barrier for the reaction is significantly reduced while the whole system is maintained at a low temperature. The described process is in fact achieved in the ablation process, where a high laser energy density is absorbed by a very small volume of the target material. The ablation threshold must be satisfied to eliminate any thermal evaporation due to laser heating; this is dependent on the absorption coefficient of the material, thus in turn depends on wavelength. With an appropriate choice of ablation wavelength with the target, high energy densities are absorbed by a small volume of material, resulting in vaporisation that is not dependent on the vapour pressures of the constituent cations [60].

3.1 The Ablation Process

In this section, we shall briefly discuss the material ablation process and plasma generation. In general, we can divide the process into three parts *i.e.*

- Light Material Interaction.
- Plasma Formation.
- Plasma Expansion.

All exact physical nature of these individual events is highly complex and a quantitative explanation is beyond the scope of this thesis, so we shall only discuss this in a qualitative manner.

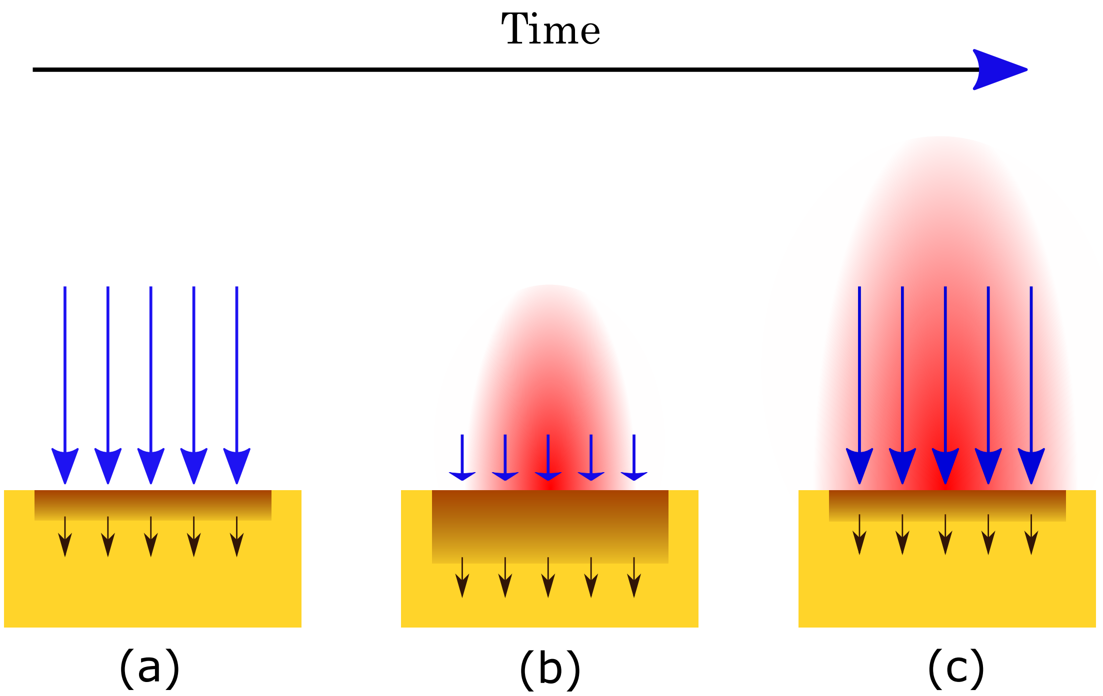

Figure 3.2: A schematic illustrating the key events of the laser ablation process. (a) Initial absorption of laser radiation into the material and formation of free electrons at the surface which transfer energy into the lattice via thermal means. (b) Formation of plasma as the initial pulse begins to recede, interaction of laser with target surface, as well as evaporated material. (c) Expansion of plasma into the deposition chamber as the next pulse reaches the target for ablation.

3.1.1 Light-Material Interaction

When high power Laser radiation is incident on a compressed target material, the electromagnetic energy is immediately converted into electronic excitations in the form of free electrons, plasmons and excitions in case of dielectrics.

Laser irradiation causes extremely high temperatures and electric fields in a small area of the target [61]. This can be easily understood by considering the amplitude scaling of the electric field produced at the surface as a result of radiation.

$$E \approx \left(\frac{2\Phi}{n\epsilon_0 c}\right)^{1/2} \tag{3.1}$$

where Φ is the incident power density expressed in $\mathrm{W/cm^2}$ and n is the refractive index of the material. For a material with refractive index 2.5 and laser power density of the order of 10^8 $\mathrm{W/cm^2}$ the approximate electric field turns out to be in the order of 10^5 $\mathrm{W/cm^2}$ which is enough to cause the breakdown of most materials at an atomic scale and induce plasma formation.

$$l_T = 2\sqrt{D_T \tau_p}; \text{ where } D_T = \frac{k}{\rho C} \tag{3.2}$$

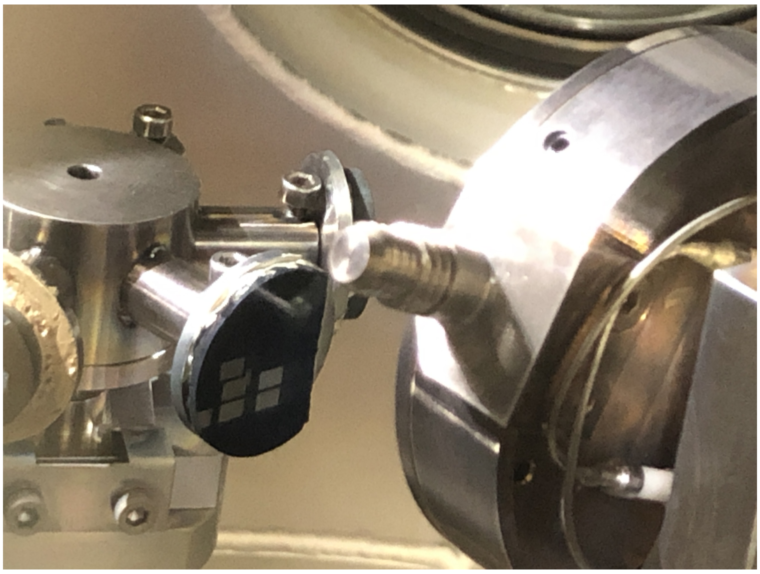

Figure 3.3: Post-ablation marks on the surface of a $SrIrO_3$ target, the well-defined laser exposure areas are indicators of how localised the laser ablation process actually is. Unexposed regions can be focused on for subsequent depositions; hence, the actual usage of material for the PLD process is much less compared to other deposition methods.

However, the optically excited free electrons transfer their energy to the lattice via thermal conduction. This is governed by Fick's law, which gives the thermal penetration depth [62] in the material in relation to the duration of the laser pulse τ_p.

$$l_T = 2\sqrt{\frac{k\tau_p}{\rho C}} \tag{3.3}$$

Here, k is the thermal conductivity, ρ is the density, and C is the specific heat of the material. We can write the above equation in an even compact form by introducing the term Thermal Diffusivity into it.

The excited electrons transfer their energy to the lattice within a few picoseconds and heating begins within the optical absorption depth of the material $1/\alpha$, where α is the optical absorption coefficient. If the thermal penetration depth is smaller than $1/\alpha$, the bulk of the material will be heated down, regardless of the duration of the pulse. In ablation of multi-elemental targets, congruent evaporation essential for stoichiometric transfer can only be guaranteed if this condition is met, and hence the use of fast UV laser sources is favoured.

3.1.2 Plasma Formation

The incidence of high intensity (10^8 W/cm^2) short pulsed laser with the target causes the surface temperatures to rise much above the melting point of the material. In their study, Bhattacharya *et.al.* [63] have estimated that the surface of $YBa_2Cu_3O_7$ (YBCO) superconducting targets will reach temperatures of 2000-3500K during the laser target interaction. As discussed previously, these high temperatures followed by electron excitation followed by material evaporation. Note that these high temperatures also cause the thermionic emission of ions, neutral atoms, and molecules from the surface. The high temperature induced pressure waves cause the kinetic energy of the ejecta to cross the thermal energy of the plume, which will act as a propelling source for the plume into the background gases of the deposition chamber.

3.1.3 Plasma Expansion

Upon the formation of plasma, it is highly concentrated near the target surface; this acts as an excellent absorption medium for the incident laser, which heats the plasma even more. This absorption predominantly occurs in the neutral atoms when the just-produced plume has a very low population of free electrons and ions. Photoionisation of the evaporated neutral and charged particles leads to a formation of an expanding plasma above target surface in form of a highly luminous glow.

Figure 3.4: A high energy 248nm Laser pulse shoots a $CaCu_3Ru_4O_{12}$ (CCRO) target producing a plasma.

The initial expansion of plasma happens in a one-dimensional fashion. Upon the termination of the first laser pulse the plume already travels 30-100 µm [64]. This happens in a very short interval of roughly $t < 100$ ns. During this time the pressure gradients are much lower near the inner edge of the plasma compared to its outer edge. During this period more evaporated material is being injected into the inner edge of the plasma, while at the same time the outer edge is rapidly expanding. In this stage the density and the pressure of the plasma decreases exponentially from its inner edge [65]. The kinetic energy of the plasma pushes it forward towards the substrate, where as it begins to lose its energy and become transparent to the subsequent laser pulses.

The plume now expands adiabatically in the deposition chamber while rapidly cooling down. The expansion is strongly peaked in the forward direction due to the extreme pressure gradients of one dimensional expansion. Due to the exponential decrease of the pressure gradient during three dimensional expansion the plume it gradually comes to a stop creating a shockwave between the background gas and the ablation plume [66]. Dyer *et. al* [67], in their study of pulsed laser ablation YBCO superconducting thin films show that as the plume expands and the mass of driven gas increases, its velocity falls and over a limited range the plume, R, behaves approximately like an ideal blast which scales as

$$R \simeq \epsilon (E/\rho_0)^{1/5} \tag{3.4}$$

where E is the laser energy coupled to the ablated species, ρ_0 is the background O_2 density and ϵ is a dimensionless parameter nearly equal to unity.

3.2 Thin Film Growth

Growth of thin film on a substrate is a complex phenomena since there are multiple factors governing the interaction of ablated spices with the substrate surface. The substrate is generally exposed to an incoming flux of plasma ablated from the target for a brief period and then enters a short hiatus before receiving the next dose of material. Upon impact the few highly energetic incident atoms may immediately bounce off the surface, while some may enter thermal equilibrium with the substrate and get adsorbed. There is also a likelihood of deposited molecules being sputtered off or re-evaporate post adsorption.

The thermal state (temperature) of the surface is a very important parameter in deciding the plasma condensation and crystalline nature of the thin film.

3.2.1 Nucleation and Self Assembly of Atoms

Assuming that the incident particles get adsorbed on the surface of the substrate, they begin to self assemble in form of tiny clusters called nuclei. This process of surface condensation and cluster formation is referred to as nucleation.

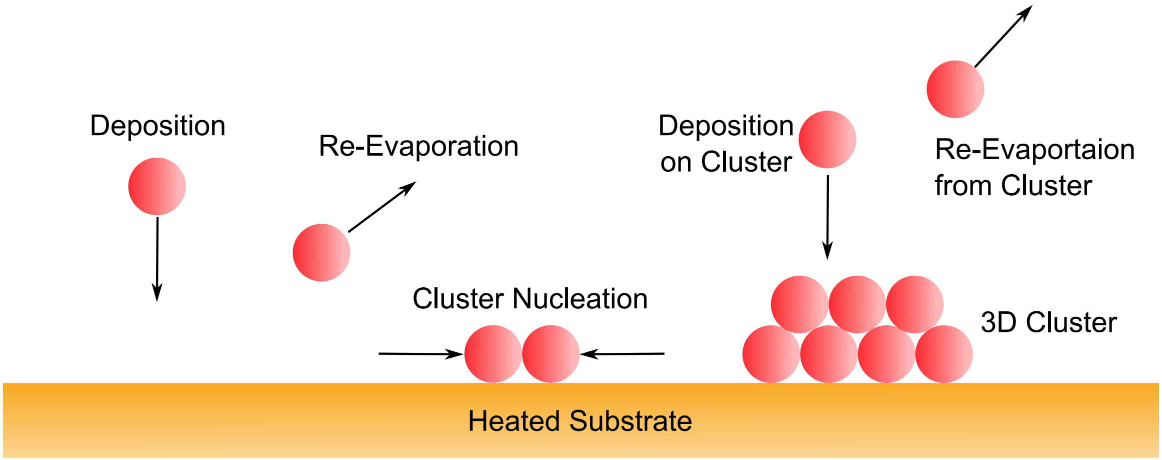

Figure 3.5: Schematic illustration of cluster formation and nucleation of incident atoms on the surface of the substrate.

The general sequence of nucleation can be described as follows. In the beginning the nuclei are randomly distributed over the substrate and are fairly uniform in size. The initial growth being diffusive in nature happens very close to the surface with the clusters having negligible height. As these relatively flat nuclei begin to coalesce together, the projected area over the substrate starts to reduce while the height of these self assembled structures increase. This exposed more substrate surface to the incoming atoms, resulting in the growth of secondary nuclei. The comparatively large clusters begin to form islands, consequently these islands elongate to form a continuous network structure separated by small irregularities. Eventually this process continues until a hole free layer is deposited on the surface.

3.2.2 Growth Modes

As the impinging atoms begin to nucleate on the substrate, it shall eventually try to minimise the interface and surface energies; similar to what a drop of wetting liquid does when it lands on a solid surface. If we model it as a similar situation taking in account all the atomistic processes happening during the vapour deposition we can consider a paradigmatic picture for the nucleation of thin films as shown in Fig. (4.1)

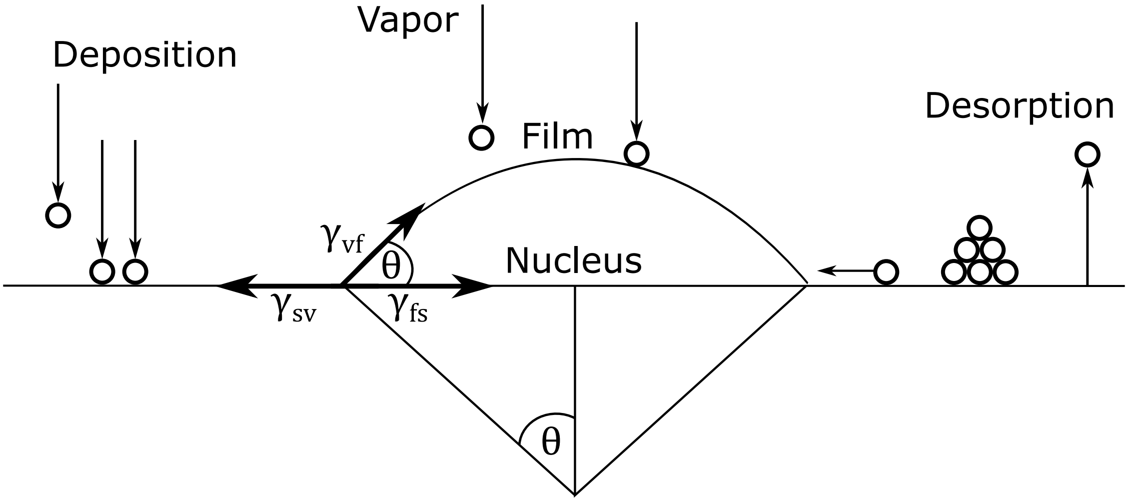

Figure 3.6: A simplified schematic of various atomistic processes and involved energy terms in a typical nucleation process.

There are several surface tension terms, γ, to deal with now, and these are identified by the subscrtipts f, s, v to represent film, substrate and vapour respectively. For the system to be in mechanical equilibrium we arrive at the relation [68]

$$\gamma_{sv} = \gamma_{fs} + \gamma_{vf} \cos\theta \tag{3.5}$$

Here θ represents the contact angle between the nucleus and the substrate, which depends only on the surface properties of the involved materials.

Now we shall look into the three basic growth modes and distinguish them based on Eqn. (3.5).

Frank-van der Merwe Growth

This is also called layer-by-layer growth where the conjunction of the smallest nucleus occurs in two dimensions, resulting in the formation of planar sheets over the surface of substrate. For layer upon layer growth to happen ideally the contact angle θ must be zero, hence we arrive at the condition;

$$\gamma_{sv} = \gamma_{fs} + \gamma_{vf} \tag{3.6}$$

This is the simplest mode of growth where a stable monolayer will form completely before a new layer begins. Such growth requires a good lattice match between the growing film and substrate, and results in formation of highly epitaxial films.

Volmer–Weber Growth

This growth mode is referred to as island growth. Here the initial clusters continue to nucleate on the substrate without coalescing with other clusters, thus growing continuously in three dimensions. This has a requirement of $\theta > 0$ thus the interfacial energy condition is

$$\gamma_{sv} < \gamma_{fs} + \gamma_{vf} \tag{3.7}$$

This kind of growth is observed when the atoms are more strongly bound to each other than to the substrate, resulting in patchy or rough films.

Stranski–Krastanov Growth

Also known as 'layer-plus-island growth', the SK mode follows a two step process: initially, complete films of adsorbates, up to several monolayers thick, grow in a layer-by-layer fashion over the substrate. Then beyond a critical layer thickness, depending on strain and the chemical potential of the deposited film, growth continues through the nucleation and coalescence of three dimensional islands. For this growth, we have the condition

$$\gamma_{sv} > \gamma_{fs} + \gamma_{vf} \tag{3.8}$$

In this case, the strain energy per unit area of film overgrowth is large with respect to γ_{vf}, permitting cluster formation above the layers.

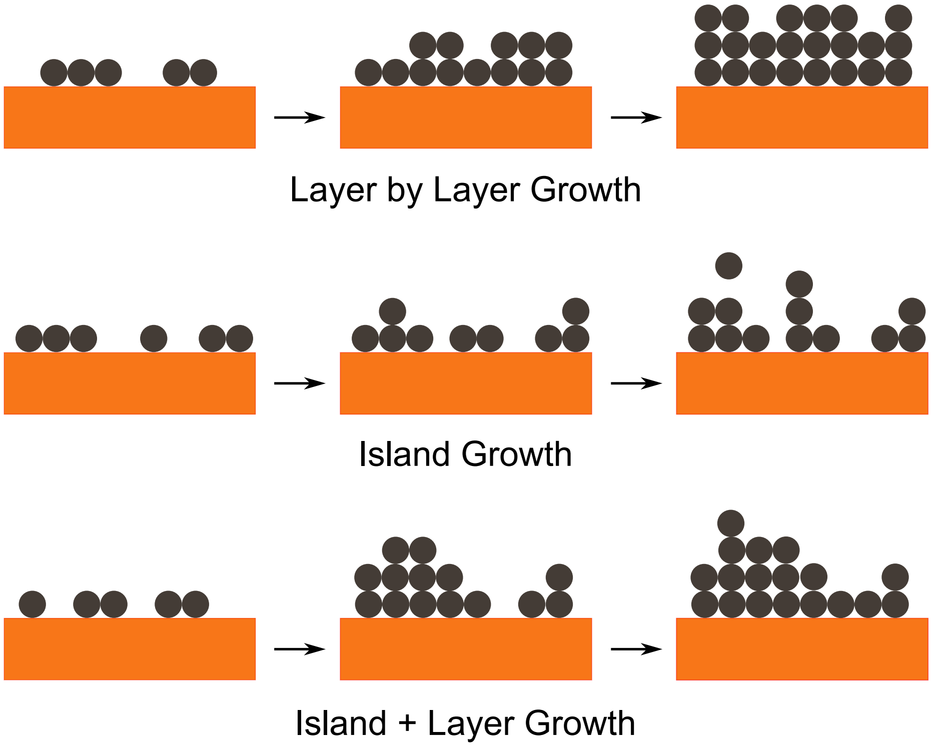

Figure 3.7: Illustration of basic modes of thin-film growth.

3.3 Effects of Processing Parameters

3.3.1 Substrate Temperature

The role of substrate temperature is paramount to grow high quality single crystalline thin films of desired materials. After adsorption on the substrate the surface diffusion rate of the adatom is given by

$$D_s = D_0 e^{-(\epsilon_D / k_B T)} \tag{3.9}$$

where ϵ_D is the activation energy essential for diffusion, it's value typically ranges from 2-3 eV on an extremely flat surface. There must be sufficient surface diffusion to allow adatom migration to stable sites by minimising their energy. A high surface temperature gives rise to increased adatom mobility and reduced quenching of ablated species. Lower substrate temperatures fail to provide the necessary surface energy to the adatoms for migrating to the lattice sites which is essential for the formation of epitaxial thin films. Hence, lower substrate temperatures may sometimes lead to multiphase and(/or) polycrystalline films. However extreme temperatures can also have adverse effect like desorption of certain deposited species, reducing the overall deposition rate and creating unwanted vacancies in the film. Therefore, for different materials an optimum substrate temperature must be determined.

3.3.2 Target to Substrate Distance

As discussed in Sec. 3.1.3, the plasma expansion is modeled as a shockwave where the plume range, R, scales as E/ρ_0. For an ambient pressure of 0.05 mbar and Laser fluence of 4 J/cm^2 the approximate plume range comes out to be $\sim$ 6 cm. For distances a lot smaller than R there is no significant difference in particulate size and species distribution. As the target to substrate distance increases, the proportion of smaller particulates decreases and a few larger particulates appear, indicating the coalescence of particulates during flight. Once the substrate is located far beyond R, the adhesion of the ablated species to the substrate surface deteriorates. Hence, the target to substrate distance must be optimised to achieve an acceptable deposition rate and film stoichiometry.

3.3.3 Ambient Gas Pressure

The gas pressure during deposition affects both plume dynamics and shape. In a vacuum environment there is virtually no collision between the ejected species before they reach the substrate due to outward plume expansion. But with the increase of ambient gas pressure the vapor species can undergo enough collisions hence promoting particulate formation before their arrival at the substrate. The gas pressure also plays an important role in determining the composition of the final thin films.

3.4 Advantages of PLD

We now list the various advantages of Pulsed Laser Deposition and understand why it is one of the most popular methods of thin film fabrication.

- Stoichiometric Transfer: Congruent evaporation of material from Laser irradiation ensures that the stoichiometry of multicomponent targets are faithfully reproduced.
- Versatile: Families of materials can be deposited in a wide variety of gases over a broad range of ambient background pressures.
- Cost Effective: Several vacuum deposition systems can be clustered around a single laser reducing the overall cost.
- Precise Thickness Control: PLD provides high degree of control on the process parameters resulting in desired deposition thickness.
- Heterostructure Growth: Growth of multilayer heterostructures and superlatices is easy compared to other deposition methods.

3.5 Experimental Setup

We have used a state of the art Pulsed Laser Deposition system manufactured by TSST, Netherlands for our thin film and heterostructure growth. The main deposition chamber can reach Ultra-High vacuum of the order of 10^{-8} mbar. The vacuum is maintained by a combination of rotary and turbo molecular pumps. It has an automated gas inlet system for precise control of background gas mixture and deposition pressure. It consists of a load-lock mechanism for the loading and unloading of the heater and targets that allows for the preservation of high vacuum in the main chamber, avoiding contamination due to repeated breaking of vacuum. For ablation our system consists of a COMPex 110 KrF Eximer laser manufactured by Coherent, USA. It gives off 248 nm laser pulse with a maximum energy of 400 mJ/pulse and a pulse width of $\sim$ 25 ns. Upon emission the laser pulse goes through a series of mirrors and a mask to define it's spot size before being focused onto the target.

The in-situ RHEED system is manufactured by kSA, USA. The diffraction pattern focused on phosphor screen which is then captured by a CCD detector for image processing. The electron beam is generated by a 30kV electron gun, manufactured by STAIB Instruments, USA.

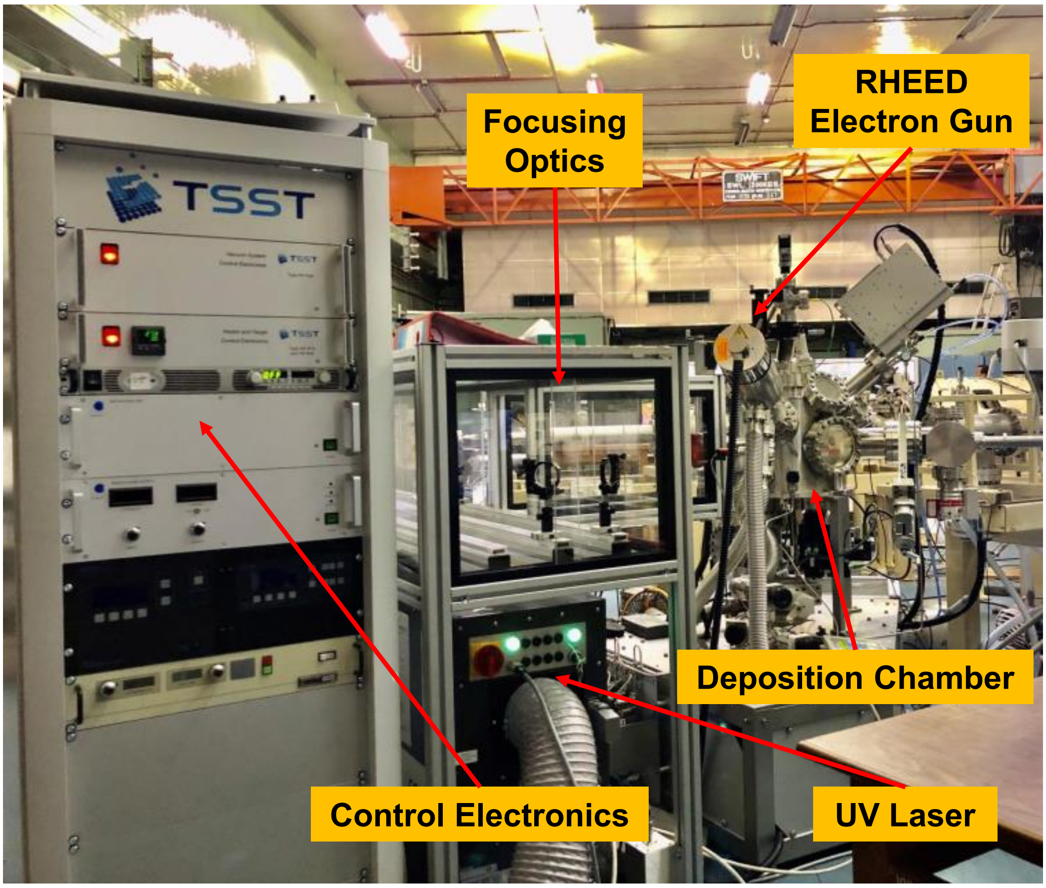

Figure 3.8: Pulsed Laser Deposition System at IoP Bhubaneswar, showing the major components the setup.

Chapter 4

Characterisation Techniques

In this chapter, the experimental techniques used for the structural and magnetic chacaterisation of the prepared thin films will be discussed.

4.1 Reflection High Energy Electron Diffraction

Reflection High-Energy Electron Diffraction (RHEED) is a powerful in situ growth characterisation technique which has proven to be a very versatile for surface studies of thin films. The combination of the forward scattering geometry of RHEED with the arrangement of pulsed laser deposition, in which the plasma plume is incident normally on the substrate, enables diffraction features to be monitored during growth.

In RHEED, high-energy electrons with energies of 10-35 keV are incident on the surface of a crystal at a grazing angle of a few degrees (1-4°). The high-energy electrons only interact strongly with the first few layers of a material, because of the low grazing angle. This makes RHEED extremely sensitive to surface morphology.

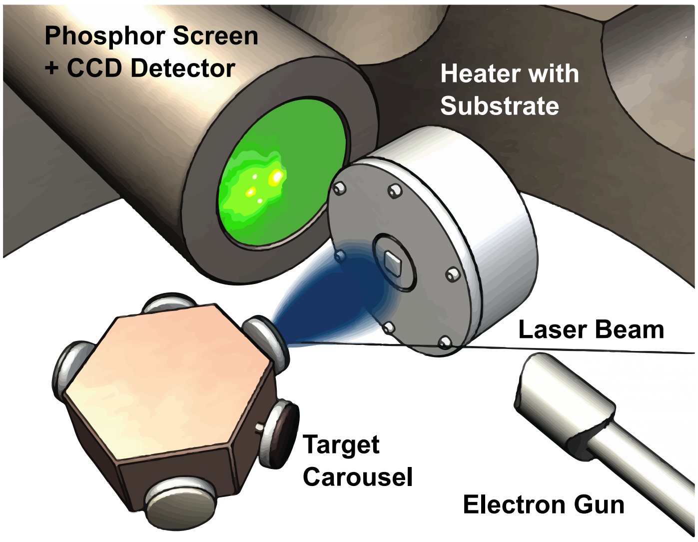

Figure 4.1: Schematic representation of the PLD system with a RHEED setup.

4.1.1 Surface Diffraction

The electrons are scattered from the crystal surface resulting in a characteristic diffraction pattern on the phosphor screen. The features in this diffraction pattern can be used to analyse the surface structure. The diffraction pattern is a combination of true reflection diffraction on smooth surfaces and transmission-reflection diffraction through particles on the surface. For a perfect surface, the rods are narrow, and spots are observed along an arc on the RHEED screen where the in-plane momentum transfer of the scattered electrons has the value of the reciprocal lattice. If broad rods or streaks are observed, this is due to poor crystallinity where the rows of atoms are partially disordered and are arranged with a range of angles relative to the incident beam. The surface diffraction collected in this way sensitively characterizes the rich variety of surface structures and phases that arise from the deposition of sub-monolayer to monolayer amounts of material [69].

When the surface is near to perfect, the '2D-pattern' exhibits in-plane diffraction spots lying on concentric circles, called Laue circles, resulting from the intersection of k-space out-of-plane lattice rods intersecting the Ewald sphere with points satisfying Braggs law. This pattern shows an angle dependence when the sample is rotated in-plane, see Fig. 4.2 (a). In the case of transmission diffraction, the lattice reciprocal space is represented by a lattice instead of rods, resulting in a typical '3D-pattern' of spots, lacking an angle dependence, see Fig. 4.2 (b).

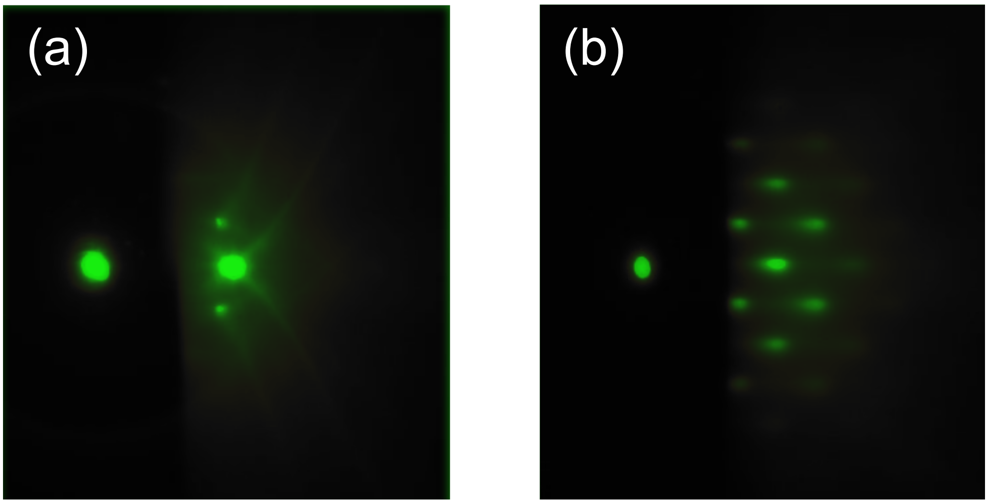

Figure 4.2: **(a)** Typical RHEED pattern of a STO substrate showing a 2D pattern resulting from an atomically flat surface. **(b)** RHEED pattern of a STO substrate showing a 3D pattern after deposition of $SrTiO_3$ under non-ideal circumstances resulting in a roughened surface.

4.2 X-Ray Diffraction

X-Ray Diffraction (XRD) is used as one of the initial, non-destructive technique to analyze the crystalline quality and crystallographic phase of any material or thin film. The detailed principles behind the working mechanism and data reconstruction procedures are well documented in literature [70–72]. In simple words an XRD works by irradiating a material with incident X-rays and then measuring the intensities and scattering angles of the X-rays that leave the material.

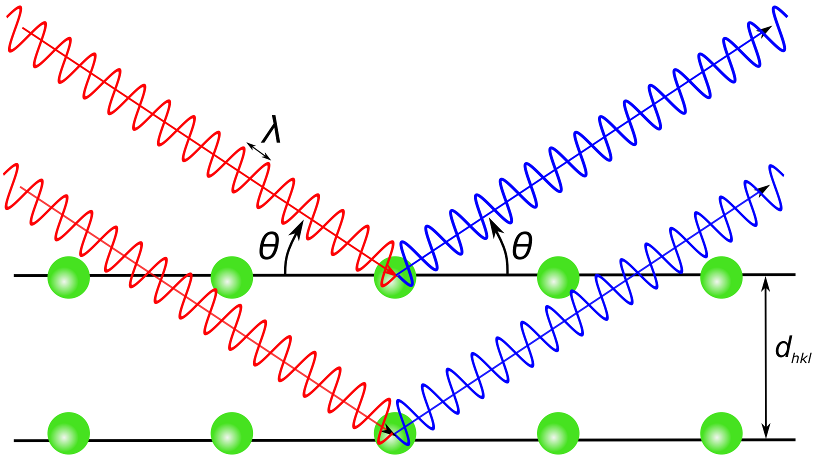

Figure 4.3: Illustration of the basic principle of X-Ray Diffraction in solids. The incident waves (red) interact with the atoms of a solid and get diffracted (blue). Bragg's Law gives the condition for constructive interference between diffracted waves, that leads to observation of peaks in the X-Ray diffraction spectra.

According to Bragg's law [73], the lattice spacing and the scattering angle of the X-ray are related as

$$2d_{hkl}\sin\theta = n\lambda \tag{4.1}$$

where d_{hkl} is the lattice spacing of a particular family of planes represented by the Miller Indices (hkl), θ is the scattering angle, λ is the wavelength of the X-ray source and n is the order of diffraction. The observation of distinct diffraction peaks is an indication of crystalline nature of the material under investigation.

4.3 X-Ray Reflectivity

X-Ray Reflectivity is a surface sensitive characterisation technique employed in the analysis of surfaces, thin films and multilayers. Derived from Snell's Law, when X-rays are incident to a sample's surface at grazing angles, total reflection will occur at or below a critical angle, θ_c. Generally θ_c is extremely small and varies depending upon the electronic density (refractive index) of the material, along with the wavelength of radiation. For extremely flat surfaces, for radiation that incidents above the critical angle the reflectivity, R, scales as $R \sim \theta^{-4}$ [74].

For rough surface or multilayer samples, a drastic decrease in reflectivity is observed. If such a material is used as a substrate for a uniform deposition of another material having a different electronic density, then reflected X-rays from the interface between the substrate and the thin film as well as from the free surface of the thin film will exhibit either constructive or destructive interfere with each other, this results in an interference induced oscillation of the recorded reflectivity. Considering a general approximation, the intensity scattered by a material thin film is proportional to the square of modulus of the Fourier transform of the electron density. Thus XRR analysis leads to determination of electron density profile from the measured intensity oscillations, and subsequently the vertical properties (layer thicknesses) as well as the lateral properties (roughness and correlation properties of interfaces or lateral layer structure) essential for characterizing multilayered structures can be obtained [75]. The film thickness can be determined from the periodicity of the oscillation and information on the surface and interface from the angular dependency of the oscillation pattern's amplitude. X-ray reflectivity data is analysed by fitting to the measured data a simulated curve calculated using the recursive Parratt's formalism combined with the rough interface formula. The fitting parameters are generally the individual layer thickness values [76].

4.4 Atomic Force Microscopy

Atomic force microscope (AFM) is a kind of scanning probe microscope that relies on the force felt by a suspended cantilever. It images the surface by 'feeling' across it. At the end of the cantilever, there is an extremely fine tip generally made of Si_3N_4 whose dimensions are of the order of a few nanometers. When the sample is scanned under the tip, the contact force causes the cantilever to deflect. By measuring the deflection of the cantilever and making a correspondence with the spatial coordinates, one can map the entire surface. A schematic diagram of the experimental setup is shown in Fig. 4.4.

4.4.1 Working Mechanism of an Atomic Force Microscope

The deflection of the cantilever beam is measured generally by using a laser beam which is reflected off the cantilever onto a position sensitive photo detector. The detector will have a split cathode photo-diode arrangement. As the sample scans the surface, the deflection of the cantilever produces a shift in the position of laser beam at the detector. When it is shifted towards any of the halves, one of the two cathodes will generate a higher voltage than the other and the difference in voltage output increases. Thus by detecting the difference in voltage, the height of the surface fluctuations of the sample is quantified. These undulations are used in a feedback mechanism to maintain a constant height with respect to the surface under investigation. With reference to this height the entire topography of the surface is mapped.

The resolution of the imaging depends on the precision of cantilever movement. For a very high resolution, the tip ought to have a relative motion of equivalent resolution with respect to the sample. For this purpose a piezoelectric transducer is used. The piezoelectric transducer will change its shape according to an applied external voltage. The sample or the cantilever can be placed onto a stage that is coupled to the piezoelectric transducer. A typical piezoelectric material will expand by about 1 nm per applied Volt. Thus, to obtain the required motions, multilayered layered piezoelectric transducers are employed, this magnifies the total movement by orders of magnitude. The in-plane resolution of the mapped image is given by the accuracy of the movement of the sample with respect to the tip and also by the dimension of the tip itself.

The resolution of the image in the third dimension depends crucially upon vibrations felt by the sample. Hence it is important to isolate the setup from mechanical vibrations by the use of floating tables or vibration dampeners [38].

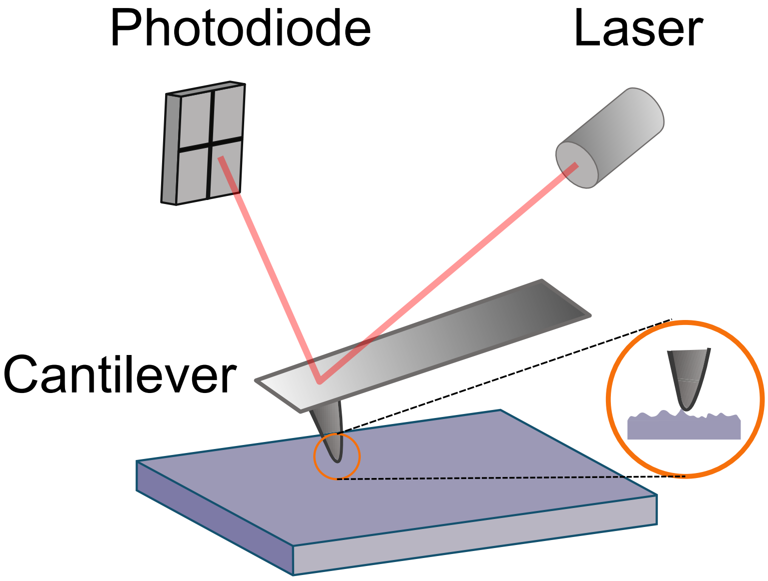

Figure 4.4: A schematic of an Atomic Force Microscopy setup.

4.5 Superconducting Quantum Interference Device (SQUID) Magnetometry

The Superconducting QUantum Interference Device (SQUID) is maybe the most sensitive measurement device known. It can measure magnetic flux of three orders of magnitude smaller than one flux quantum. A flux quantum is given by

$$\Phi_0 = \frac{h}{2e} = 2.067 \times 10^{-15}\ \mathrm{Tm}^2 \tag{4.2}$$

A flux quantum can be visualized as the magnetic flux of the Earth's magnetic field (5×10^{-5} T) through a single human red blood cell, which has a typical diameter of about 0.7 microns. The operating principles of SQUIDs is based on the phenomenon of Josephson effects, a device based on a Nobel prize winning tunneling effect proposed in theory by Brian. D. Josephson [77] in 1962 and first observed experimentally in 1964 by Anderson and Rowell [78]. A SQUID device consists of a closed superconducting loop including one or two Josephson junctions in the loop's current path.

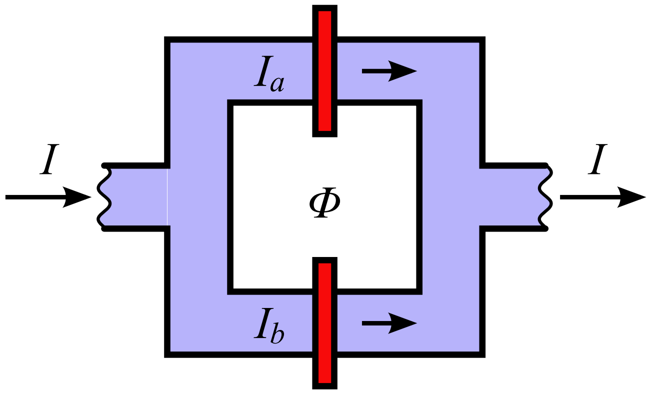

Figure 4.5: A schematic diagram of a DC squid with two Josephson Junctions (red) in parallel. Φ represents the trapped magnetic flux within the superconducting ring.

As discussed by Mizutani [79] the total phase change in superconducting ring must be an integral multiple of 2π, for the wavefunction to remain single valued. Following the derivation we have the total current in the loop as

$$I - 2I_C \cos\left[\pi\left(n - \frac{\Phi}{\Phi_0}\right)\right]\sin\delta \tag{4.3}$$

Where δ is a self adjusting parameter that depends on the measuring current I and Φ is the magnetic flux threaded to the superconducting ring. So the maximum external current that can flow as supercurrent in the device is

$$I = 2I_C \left|\cos\left(\frac{\pi\Phi}{\Phi_0}\right)\right| \tag{4.4}$$

In the absence of a measuring current internal circulating current *adjusts* itself such that there are exactly integral number of fluxoids trapped in the ring. When the applied flux matches the required values i goes to zero and for half integral values the circulating current is maximum in either direction. [80]

4.5.1 Measurement principle of SQUID magnetometry

The magnetic field detection sensitivity of a SQUID depends on its effective loop area. But generally due to design constraints the area of the SQUID loop cannot be made much large, this affects the overall sensitivity of the system. So in commercial systems a superconducting flux transformer is used to amplify the magnetic field sensitivity of a SQUID system. Pickup coils consist of a superconducting wire wound in a set of three coils configured as a second order gradiometer as shown in Fig. 4.6.

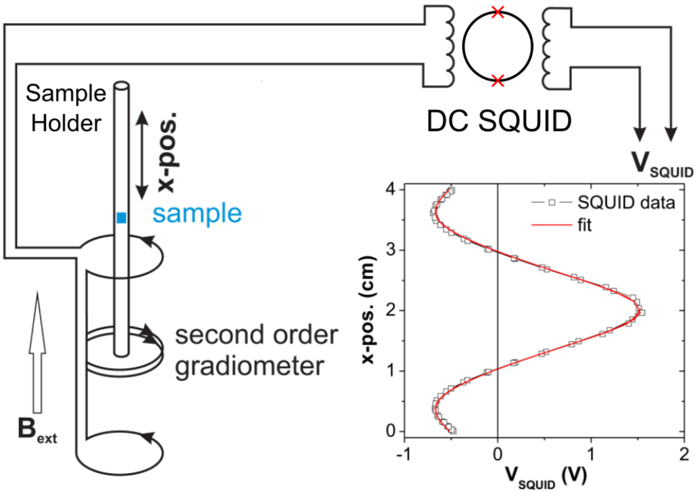

Figure 4.6: Schematic setup of a SQUID magnetometer with 2nd order gradiometer and a typical voltage response curve with respect to position.

The upper coil is a single turn wound clockwise, the center coil comprises two turns wound counterclockwise, and the bottom coil is again a single turn wound clockwise. This gradiometer configuration is used to reduce the noise in the detection circuit caused by the fluctuation in the large magnetic field of the superconducting magnet whereas any homogeneous contributions from any external fields are cancelled out. Centered around the pick-up coil is the superconducting magnet capable of producing a uniform constant magnetic field over the entire coil region.

The actual measurement is performed by moving the sample through the superconducting pick up coil, which are located outside the sample chamber and at the centre of superconducting magnet. The sample is mounted in a sample holder that is in the form of a rod and it is externally attached to transport mechanism to drive the sample through the pick up coil. As the sample moves through the coils, the magnetic moment of the sample induces an electric current in the pick up coil due to the change in the flux associated with it. Since the pick up coil, the connecting wire and the SQUID input coil form a closed superconducting loop, any change of magnetic flux in the pick up coil produces a change in the persistent current in the detection circuit, which is proportional to the change in the magnetic flux. A SQUID system can be considered as a linear high-gain current to voltage amplifier [81], thus any variation of current in the pick up coil produces corresponding variation in the SQUID output voltage. Eventually, the output voltage V is recorded as a function of scan length z. The data aquisition and processing interface then fits the measured $V(z)$ data points to the theoretical curve of an ideal dipole and thus extracting the magnetic moment, m.

Chapter 5

Growth of Ferroelectric $Ba_{0.8}Sr_{0.2}TiO_3$ (001) Thin Films

5.1 Introduction

$Ba_{1-x}Sr_xTiO_3$ is essentially a solid solution of $BaTiO_3$ and $SrTiO_3$. $BaTiO_3$ is in the ferroelectic (polar) phase at room temperature, and has a ferroelectric to paraelectric transition temperature (Curie point) of 130° C , while $SrTiO_3$ is paraelectric (non-polar) down to absolute zero [82]. In the $Ba_{1-x}Sr_xTiO_3$ solid solution, substitution of Sr atoms in the place of Ba atoms causes the Curie point to decrease linearly. Studies have shown that the Curie point of $Ba_{1-x}Sr_xTiO_3$ drops to 0° C with 34% Sr content, corresponding to a decrease of 3.8° C per molar percent Sr [83].

Like its parent and dopant constituents $BaTiO_3$ and $SrTiO_3$, $Ba_{1-x}Sr_xTiO_3$ also has a perovskite structure. It's ferrolectric properties originate from the non centrosymmetric shifting of the Ti atom in the oxygen octahedron. The doping of Sr apart from increasing the dielectric constant introduces additional strain in the lattice that improves its piezoelectric behaviour [84]. This strain also reduces the lattice parameter and thus improves the tertagonality of the structure. For our case we have doped $BaTiO_3$ with a Sr substitution of x=0.2, making our effective material as $Ba_{0.8}Sr_{0.2}TiO_3$. This has the unit cell lattice parameter 3.989 Å compared to undoped $BaTiO_3$ with lattice parameter 4.007 Å. Hence this substitution also helps in reducing the lattice mismatch with $SrTiO_3$ substrates.

5.1.1 Polarisation Direction in BSTO Thin Films

Much literature is not available on the growth of epitaxial $Ba_{0.8}Sr_{0.2}TiO_3$ thin films. However, we can follow the reports based on it's mother compound $BaTiO_3$ due to their structural similarity. Experimental study have already proven that BTO thin films retain robust room temperature ferroelectricity down to 1 nm (∼ 2 u.c.) on $NdGaO_3$ substrate [85] and 1.6 nm (∼ 4 u.c.) on $SrTiO_3$ substrate [86].

Experimental studies have shown that many as-grown ferroelectric films tend to have one preferred polarisation direction, *i.e.* self-polarisation [87, 88]. Wu *et. al* [89] in 2016 studied influence of crystal orientations on the phase diagrams, dielectric and piezoelectric properties of epitaxial BTO thin films. They reported that (001) oriented films have the least misfit strain and will retain an out of plane polarisation. In 2021 Li *et. al* [90] demonstrated a polarisation-enhanced interface in *c* axis oriented BTO films by tuning oxygen inhomogenity through first principle simulations [90]. Despite these extensive studies, the issue of as-grown polarization of the BTO films has not been addressed adequately to implement in experiments. An important factor in our experiments was to identify and stabilise the self polarisation direction in the thin film.

A fairly recent study that focused on investigating the self polarisation of BTO thin films was conducted by Guo *et. al* [91]. They found that the self-polarization of BTO thin films depends on both the interface and the flexoelectric effects. In the low thickness regime, the film is fully strained, the interface effect (surface termination) is the dominating factor which determines the self-polarization direction. With increase of the film thickness, the strain of BTO film by STO substrates starts to relax, and the flexoelectric effect becomes dominant which favors the self-polarization to be upward.

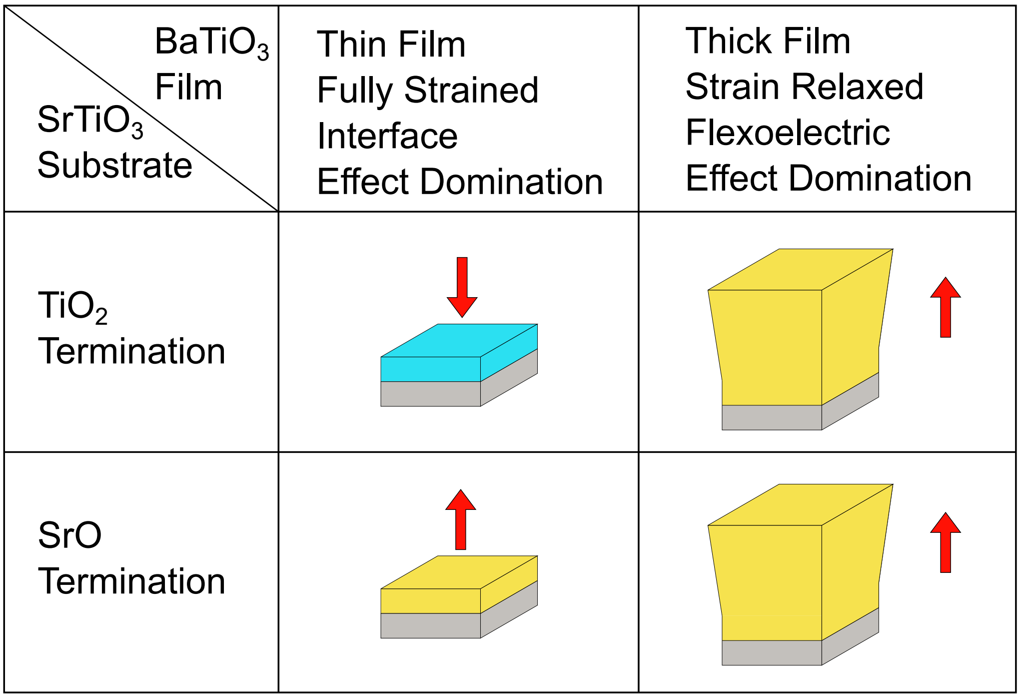

Figure 5.1: Schematic summary of how surface and flexoelectric effects affect the polarization of BTO films grown on STO substrates with two different terminations. Adapted from Guo *et. al* [91].

5.2 Target Preparation and Analysis

5.2.1 Solid State Reaction Method

The reaction sequence used to prepare $Ba_{0.8}Sr_{0.2}TiO_3$ is

$$BaCO_3 + SrCO_3 + TiO_2 \longrightarrow Ba_{0.8}Sr_{0.2}TiO_3 + CO_2 \tag{5.1}$$

Prior to preparation the precursor materials were heated at around 60-70% of their decomposition temperatures to remove adsorbed volatile impurities. Polycrystalline $Ba_{0.8}Sr_{0.2}TiO_3$ was prepared by mixing the preheated $BaCO_3$, $SrCO_3$ and TiO_2 powders in stoichiometric quantities in an Agate mortar pestle. The mortar pestle was cleaned with Aqua-Regia followed by de-ionised water before tranferring the materials into it.

The materials were grounded together for roughly 12 hours to ensure proper intermixing of the powders. a few drops of pure isopropyl alcohol was occasionally added to promote adhesion between the powders during the grind.

The reaction crucible was cleaned in Aqua-Regia and rinsed in de-ionised water. It was then allowed to dry in an hot air oven for 3 hours. The uniformly mixed contents were transferred to the Alumina crucible which was placed in a Box Furnace. The calcination reaction was performed at 1100° C for 10 hours. The following temperature profile was followed for the reaction.

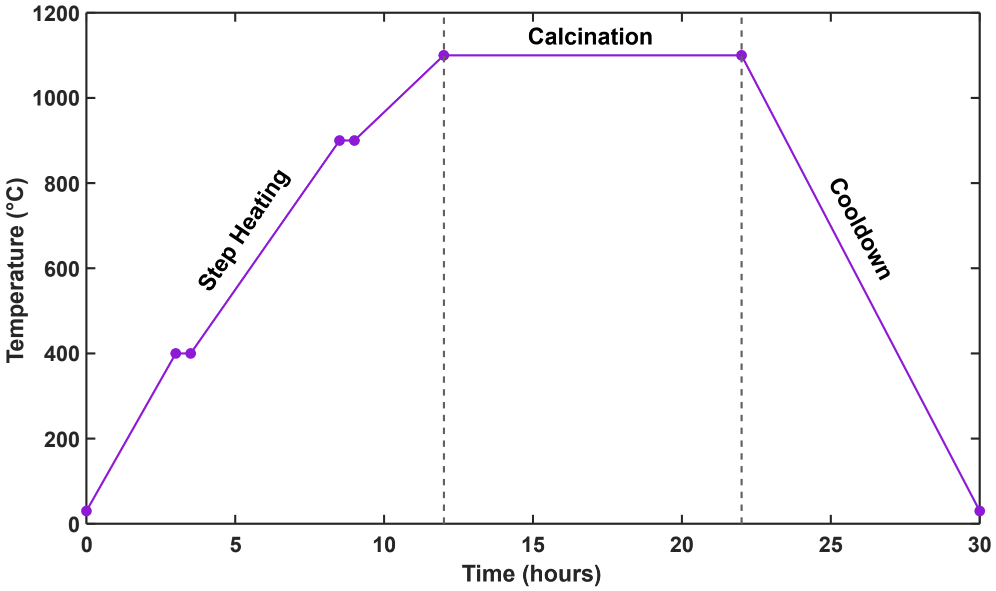

Figure 5.2: Temperature profile followed for the calcination reaction, in preparing BSTO.

There are three major regions in the temperature profile followed for the solid state reaction, as seen in Fig. 5.2.

1. **Step Heating:** Here the furnace is heated in three steps from room temperature to the calcination temperature (1100° C). Initially a fast ramp rate is used till it reaches 400° C the the furnace is held there for 30 minutes before heating to 900° C and again holding for 30 minutes. The final ramp is done at a much slower ramp rate to reach the target temperature of 1100° C. This profile of variable ramp rate and 0.5 hour holdings are done to protect the heater filament from breaking.

2. **Calcination:** The main reaction happens in this step when we hold the furnace temperature at 1100° C for 10 hours. The different precursor materials gain very high thermodynamic energy due to the temperature and begin to react among themselves forming a stable phase. Depending upon this calcination temperature and time the final product can be single or multiphase.

3. **Cooldown:** The furnace cooling is done at a relatively fast rate over a period of 8 hours.

5.2.2 Polycrystalline Powder Characterisation

A $\Theta - 2\Theta$ XRD (See Sec. 4.2 for details) scan of the prepared powder was performed with Cu-Kα radiation, at a scan rate of 5° per minute.

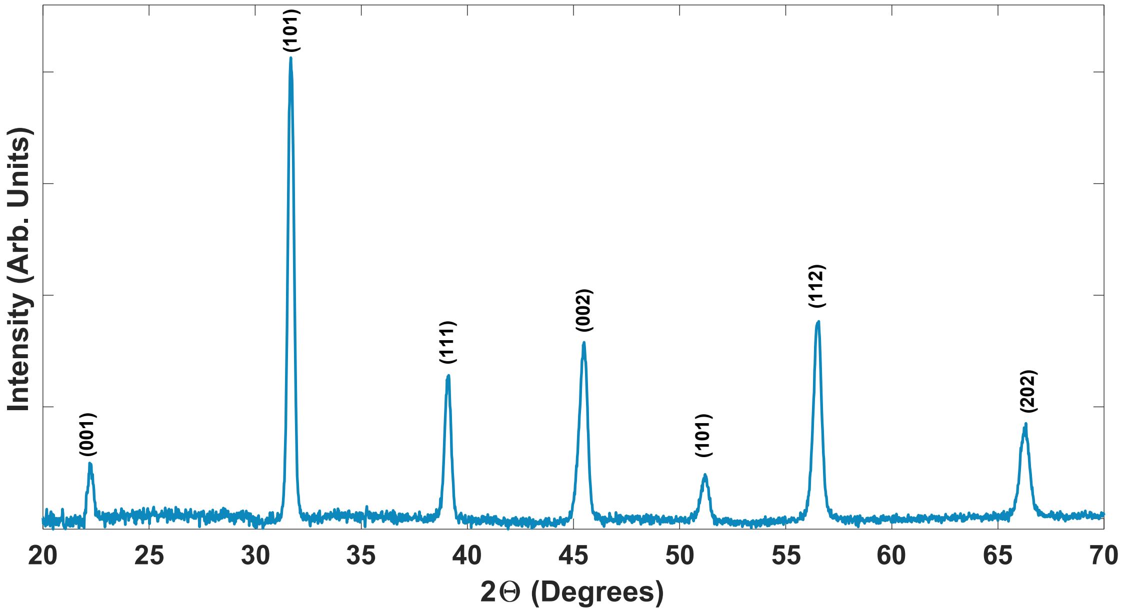

Figure 5.3: X Ray Diffraction pattern of the prepared BSTO powder. The powder shows proper polycrystalline phase and the cubic lattice parameters.

5.2.3 Pellet Preparation

The powder was ground again for 1 hour to break the agglomerates that had formed during the calcination reaction. A few drops of isopropyl alcohol were added to enhance the adhesion between the particles, helping in the pelletisation process. The prepared powder was then transfered into a circular die and a pressure of 8 tonnes was applied. The powder was left under pressure for 30 min to allow the particles to bond to each other properly.

The formed pellet was sintered at 1000° C for 12 hours to harden it by fusing the particles together. After the process, a very slow cooling rate of about 60°C/hour was maintained to avoid crack formation.

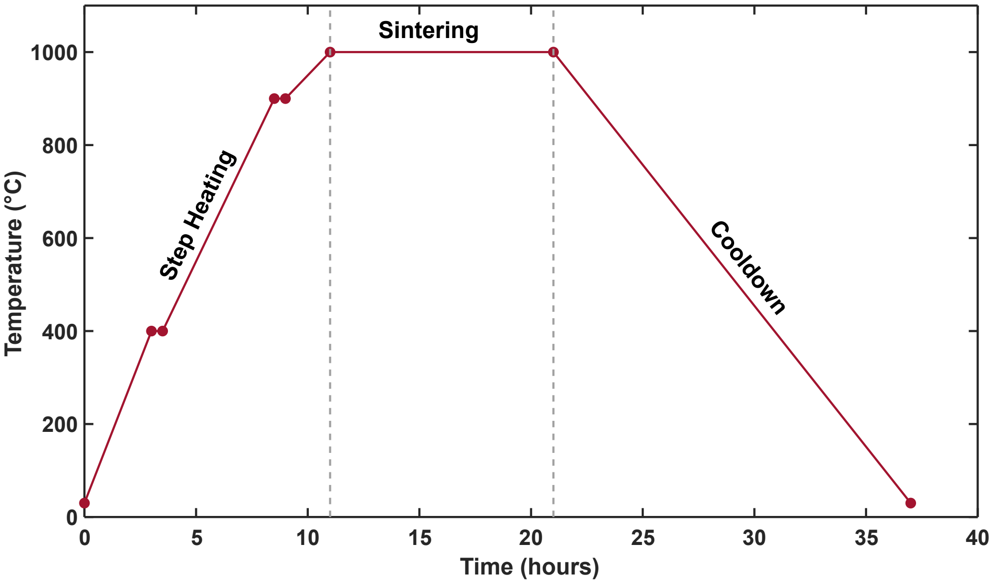

Figure 5.4: Temperature profile followed for the sintering process of BSTO pellet.

The hardened pellet was pasted on to a target holder with conducting silver epoxy to mount in the in PLD target carousel.

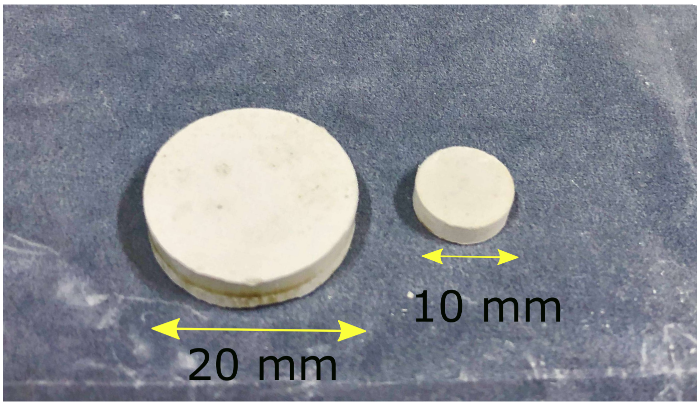

Figure 5.5: The hardened 20mm and 10mm pellets of BSTO post sintering procedure.

5.3 Thin Film Growth

The thin films were prepared by Pulsed Laser Deposition process whose complete review is presented and discussed in Chapter 3.

5.3.1 Substrates

Since tetragonal single phase film of BSTO with out of plane polarisation direction is required to observe the desired interfacial effects, we choose $SrTiO_3$ single crystalline substrates with (001) orientation. STO has a cubic perovskite structure with a lattice parameter of 3.905 Å. Taking into account the in-plane lattice parameters of BSTO, the STO/BSTO interface will have a lattice mismatch of 2.1% which is acceptable for epitaxial growth. For experiments where a bottom contact is required, 0.05 wt% Niobium doped STO substrates were used. Nb doped $SrTiO_3$ single crystal has similar structure to pure $SrTiO_3$, but becomes electrically conductive.

Before use, the substrates were cleaned by immersing in isopropyl alcohol in an ultrasonic cleaner for 1 hour. The polished side of the substrate was properly dried and mounted on the heater using conductive silver paste. A DC voltage of 13 V was applied to the heater leads till the surface was hot to touch. This step is crucial as it allows the paint to dry and also evaporates any volatile organic solvents in the paint which can de-gas and contaminate the chamber when placed under vacuum.

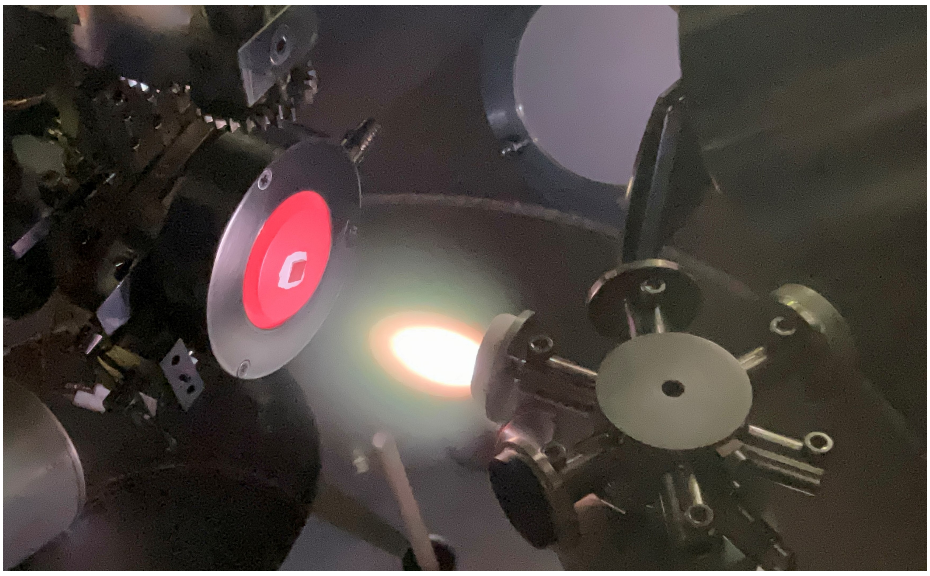

Figure 5.6: Snapshot of the BSTO thin film deposition process.

5.3.2 Deposition Conditions

The BSTO/STO (001) and BSTO/Nb:STO (001) thin films were grown under the following deposition conditions:

- Substrate Temperature: 650° C
- Target Substrate Distance: 110 mm
- Pressure Conditions: A pressure of 0.2 mbar O_2 was maintained with dynamic flow of gas in the chamber.
- Laser Fluence: 1.4 J/cm^2
- Pulse Repetition Rate: 2 Hz
- Number of Pulses: 4000 pulses in case of BSTO/STO(001) thin film and 6000 pulses in case of BSTO/Nb:STO(001) were fired.
- Cooling Rate: 5° C/min in presence of 0.2 mbar static O_2 pressure.

5.3.3 RHEED

In situ RHEED of deposition process was performed to examine the growth quality of the thin films. A 30 kV electron beam of beam current of value 1.6 µA was used for the imaging. It can be easily seen in Fig. 5.7 (a) that the specular spot intensity is very high and the three solid spots indicate a bare substrate surface. The image taken after deposition at room temperature under vacuum *i.e.* Fig.5.7 (b), has multiple prominent diffraction spots corresponding atomic layers of BSTO on STO. This indicates a high quality crystalline growth.

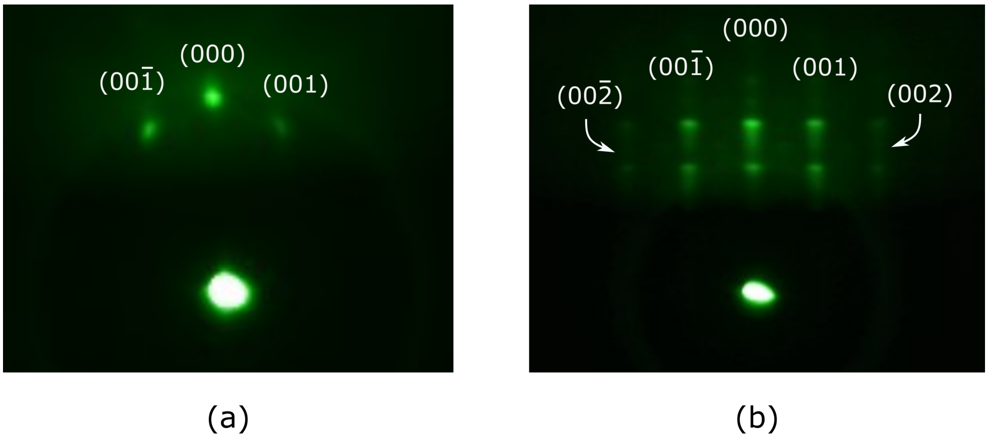

Figure 5.7: (a) RHEED of STO(001) substrate taken before deposition at 650°C in vacuum. (b) RHEED of BSTO film deposited on STO(001) substrate after 4000 laser pulses, taken at room temperature in vacuum. The labelling indicate the corresponding miller indices.

5.4 X-Ray Diffraction Study

The X-Ray Diffraction experiments were performed Cu K-α radiation which has a characteristic wavelength of 1.5406 Å.

5.4.1 BSTO/STO (001)

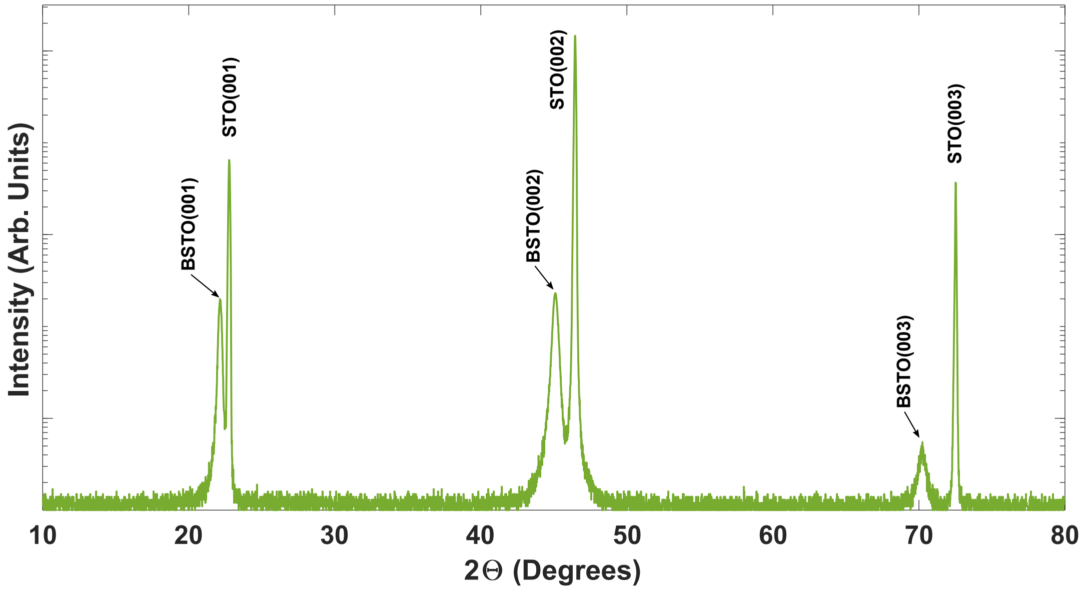

Figure 5.8: $\Theta - 2\Theta$ X Ray Diffraction spectra of BSTO/STO(001) thin film. The spectra shows the peaks for the BSTO thin film alongside the STO substrate peaks.

5.4.2 BSTO/Nb:STO (001)

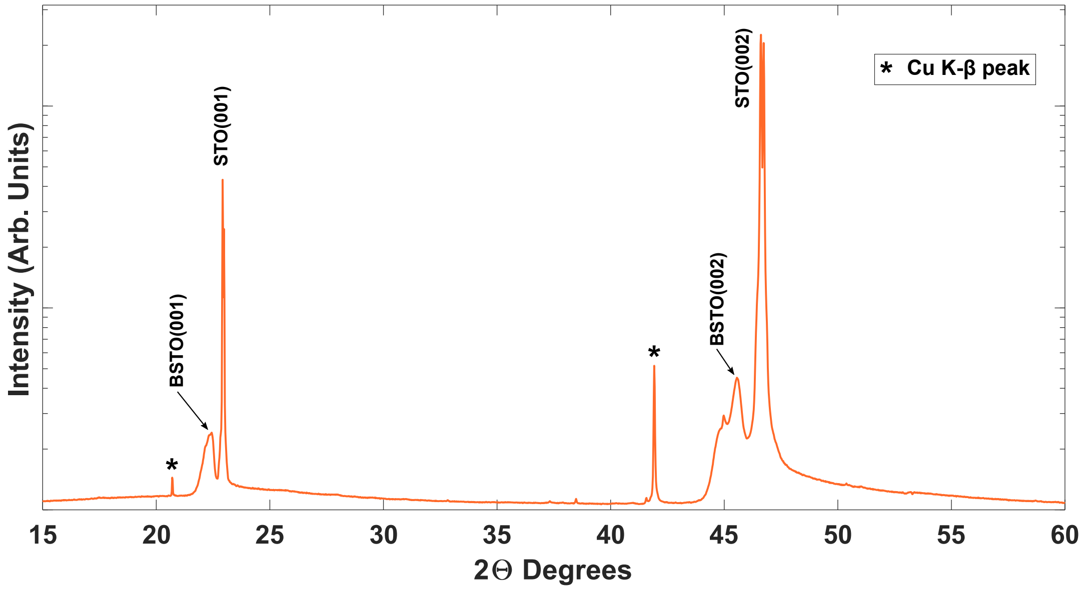

Figure 5.9: $\Theta - 2\Theta$ X Ray Diffraction spectra of BSTO/Nb:STO(001) thin film prepared by pulsed laser deposition method. The spectra shows the peaks for the BSTO thin film alongside the Nb:STO substrate peaks and Cu K-β radiation peaks.

5.5 Ferroelectric Characterisation

The ferroelectric properties of the BSTO thin films were characterised by various methods. The procedures and protocols are discussed in this section.

5.5.1 Device Fabrication

Before the polarisation measurements, metallic contacts had to be deposited on the top surface of the BSTO thin film. Since for these experiments films were grown on conducting Nb:STO subsrtates, thus the substrate itself acts as the bottom contact avoiding any complicated etching procedures to probe the lower surface.

Gold was chosen as the electrode material due to its low resistivity. About 0.4 µm thick gold was deposited on the top surface of the film using DC Sputtering technique.

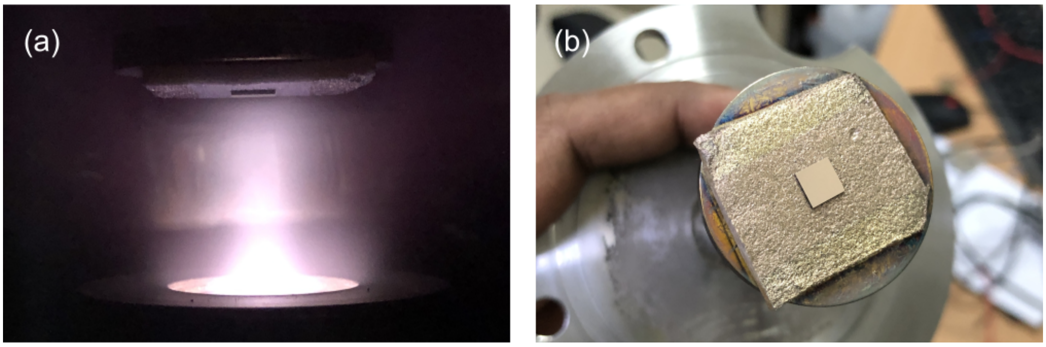

Figure 5.10: (a) Snapshot of the gold electrode deposition process via DC sputtering method, the bright luminous glow at the center is due to the sputtering gold ions moving towards the negatively charged substrate holder. (b) Uniform layer of gold deposited on the thin film surface.

After defining the top electrode a device was fabricated in the following schematic.

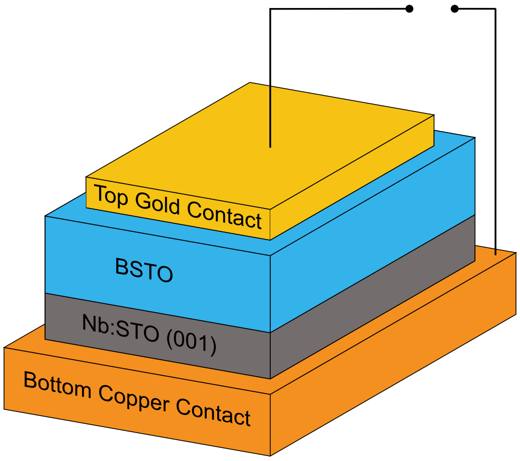

Figure 5.11: A schematic of the final configuration of the BSTO thin film used for property measurements.

5.5.2 Polarisation Measurements

The polarisation measurements were performed on a commercial Ferroelectric Tester setup. For the experiment a 1 kHz Standard Bipolar input wave was applied to the ferroelectric thin film and the output was amplified using the 200V internal amplifier of the device.

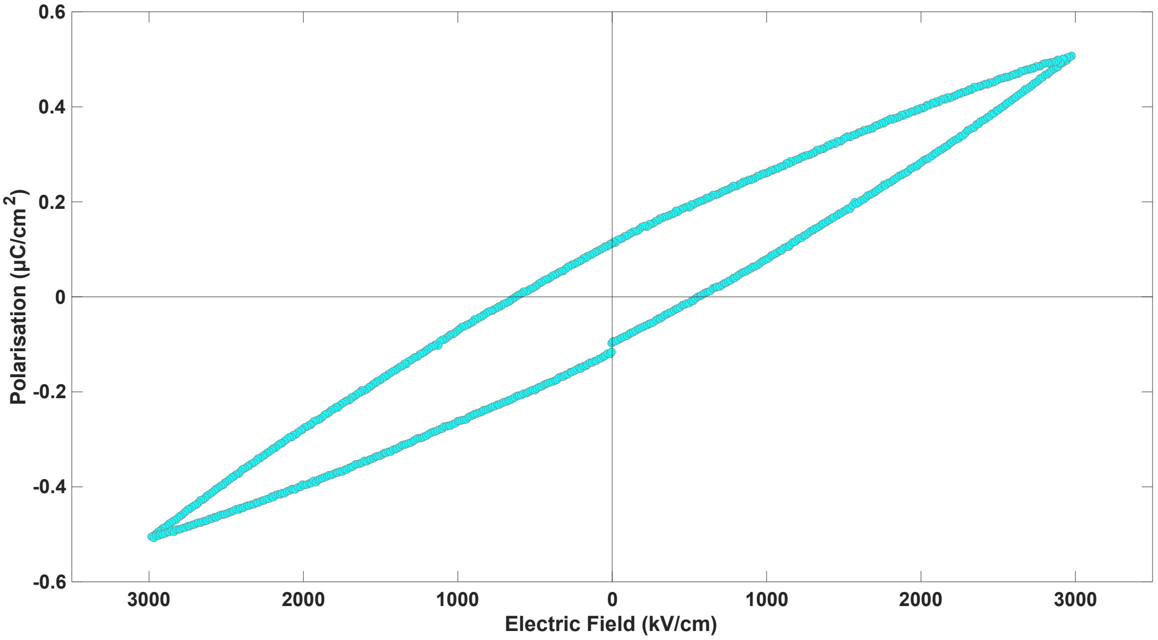

Figure 5.12: Polarisation Vs. Electric Field curves for the BSTO thin films. The obtained values are P_{max} = 0.507 μC/cm^2 and P_r = 0.113 μC/cm^2

The following data was obtained from the experiment

- Maximum Polarisation, $P_{max} = 0.507$ μC/cm^2
- Average Remnant Polarisation, $P_r = 0.113$ μC/cm^2
- Coerecive Electric Field, $E_c = 834.134$ kV/cm
- Effective Capacitance, $C_{\text{eff}} = 1.07$ pF

5.5.3 Impedance Analysis

An impedance analyser is an electronic device that can measure complex electrical impedance as a function of frequency. The overall process involves a phase sensitive measurement of the applied voltage and current while the frequency is continuously varied throughout the course of experiment. In general impedance analysis is performed to obtain information like resonance frequency, phase response and S parameters of a device under testing. Such measurements are also useful in characterising various dielectric materials. Impedance analysis was performed on the BSTO thin film to observe its frequency response to external AC signals and to determine the resonance frequency.

5.5.4 Frequency and Phase Response

The impedance analysis was done in the constant current mode with I=500 µA, 100 ms averaging was performed on the recorded data.

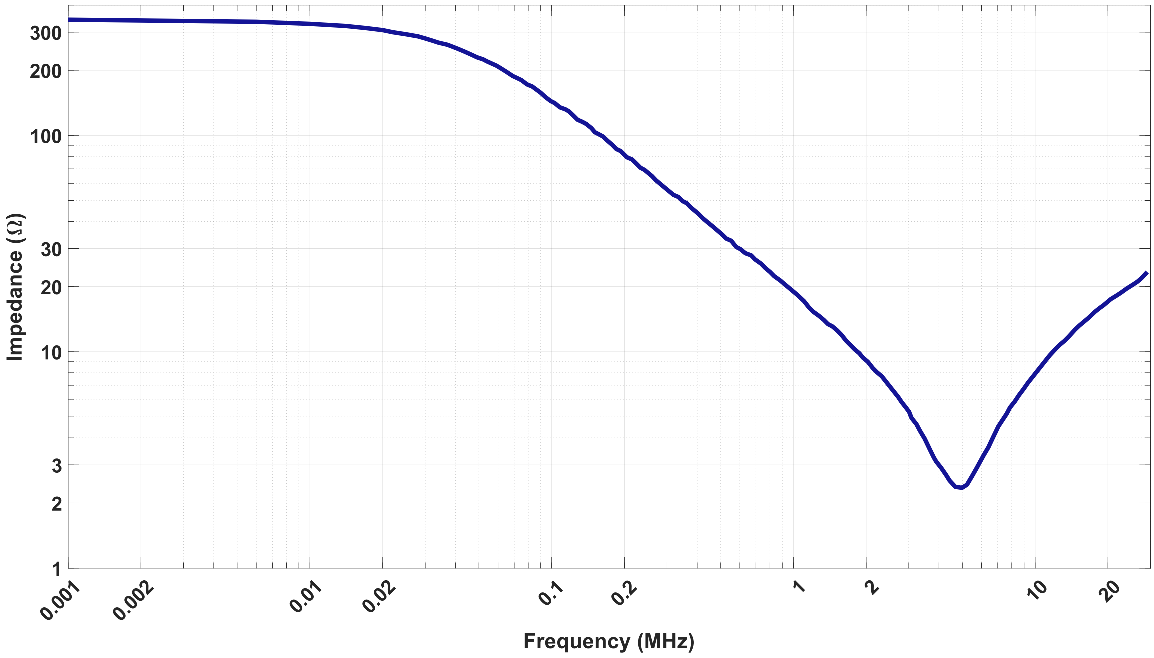

Figure 5.13: The Impedance Vs Frequency graph of the BSTO thin film. The thin film shows high bandwidth and has a resonance frequency around 2.5 MHz.

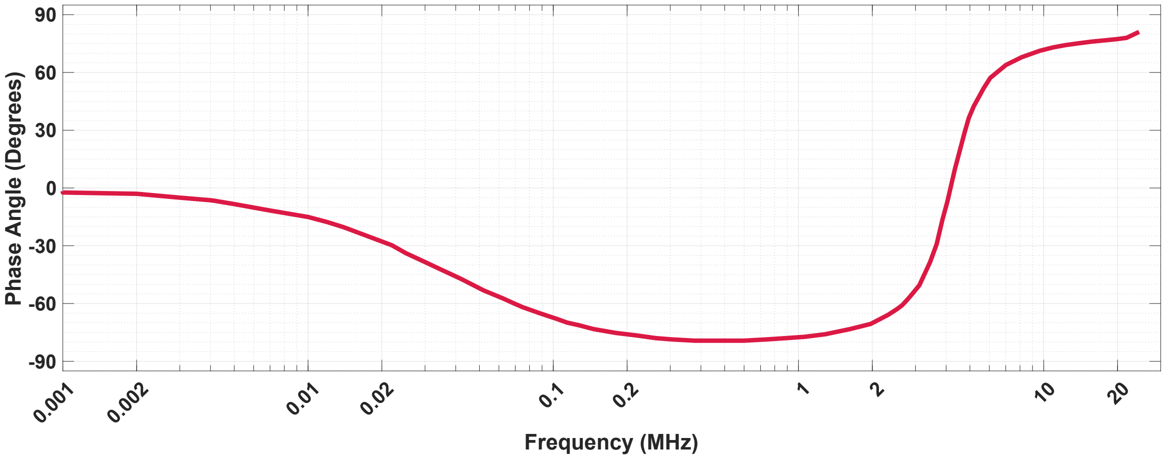

Figure 5.14: The phase response of the thin film under an continuously changing frequency.

5.6 Discussion

BSTO target material was successfully prepared by Solid State Reaction method and characterised by X-Ray Diffraction. The absence of any unexpected peaks indicate a proper phase formation in the polycrystalline material. Now coming to thin films, a streaky RHEED pattern after PLD growth of the film indicates 2D layer by layer growth. The XRD spectra of the BSTO/STO(001) thin films only shows the peaks corresponding to *ab* planes. This confirms that the only *c* axis oriented growth has taken place without any disordered or strained phases. This is a particularly important observation, as our ferroelectric films must be highly epitaxial and oriented to ensure out of plane electric polarisation. The BSTO/Nb:STO(001) thin films show some additional peaks compared to the previous film. These peaks however are not due to additional phases or growth orientation, they actually correspond to diffraction of Cu K-β radiation, which the diffractometer could not filter. We performed electrical polarisation measurements on the prepared ferroelectric thin films and obtained a *P-E* hysteresis loop, this confirms the presence of ferroelectric polarisation in the thin film. Additionally we performed impedance analysis on the films and found resonance behaviour in the frequency response curve, this is one more confirmation of presence of permanent electrical polarisation.

Chapter 6

Growth, Structure and Magnetic Properties of $La_{0.7}Sr_{0.3}MnO_3$ (001) Thin Films

6.1 Introduction

Lanthanum strontium manganite $La_{1\text{-}x}Sr_xMnO_3$ (LSMO) is a doped manganite perovskite. It is perhaps one of the most well-studied classes of materials since the discovery of the colossal magnetoresistance phenomenon in 1950 by G. H. Jonker and J. H. van Santen [92].

Ordered magnetism is observed in $LaMnO_3$ (a superexchange mediated antiferromagnetic insulator) − the mother compound of $La_{1\text{-}x}Sr_xMnO_3$ due to the Mn cation. Mn is in the +3 oxidation state with four $3d$ electrons, three of them occupy the t_{2g} levels and one occupies the e_g level. Due to a strong Hund coupling, all the spins are parallel on a given Mn site [93]. The highly correlated e_g band electrons create a large correlation gap above the Fermi energy. Introduction of Sr dopants induces holes at the e_g band near the Fermi energy. At a doping concentration of x=0.175 Jahn-Teller distortion vanishes and the magnetic ordering changes from antiferromagnetic to ferromagnetic [30], with a large effective magnetic moment since the intra-atomic Hund coupling is strong enough to align the spins within the same ionic site. Due to the strong intra-atomic ferromagnetic coupling between the itinerant holes and the localized spins ($S = 3/2$), the spins first cant (tilt) until the system becomes a ferromagnet upon doping with holes. A simpler explanation of hole doped ferromagnetic transition can be attributed to the creation of mixed valency of Mn within the crystal that favour the ferromagnetic double exchange, to minimise the overall energy of the system. The double exchange mechanism also explanins the conductivity of LSMO. For a detailed explanation of double exchange mechanism refer to Section 2.3.

6.2 Thin Film Growth

6.2.1 Target

The reaction sequence involved in the preparation of $La_{0.7}Sr_{0.3}MnO_3$ is

$$La_2O_3 + SrCO_3 + MnCO_3 \longrightarrow La_{0.7}Sr_{0.3}MnO_3 + CO_2 \tag{6.1}$$

LSMO powder was prepared by Solid State Reaction method in a similar process described in Sec. 5.2.1. The first round of calcination was performed at temperature of 900° C for 8 hours. The material was re-ground and subjected to a second round of calcination at 1000°C for 11 hours.

Post calcination the powder was characterised with XRD to confirm the proper phase formation. Finally it was pelletised and sintered as in Sec. 5.2.3 to obtain a target for PLD.

6.2.2 Substrates

$SrTiO_3$ single crystalline substrates with (001) orientation were used to grow LSMO thin films. The substrates were prepared for deposition in the same process as mentioned in Sec. 5.3.1.

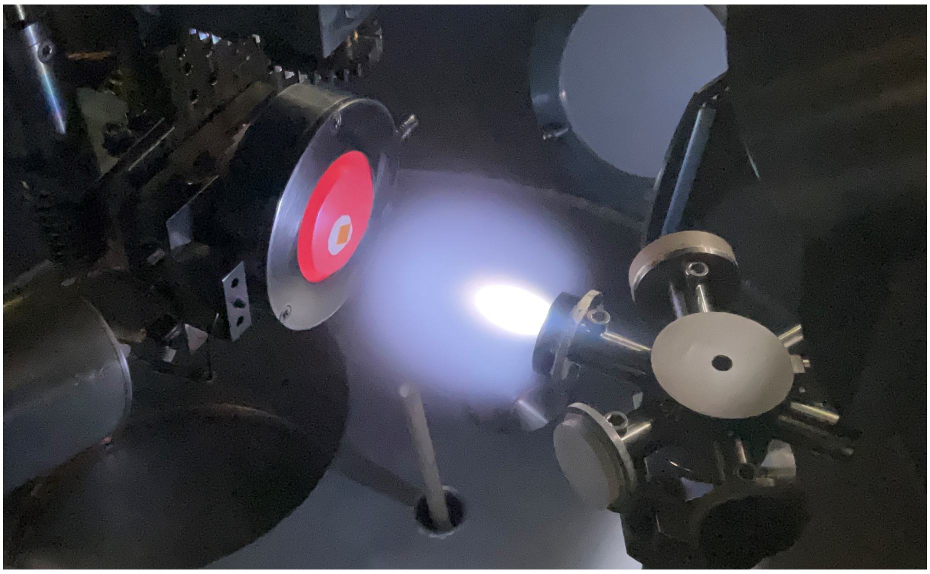

Figure 6.1: Snapshot of the LSMO thin film deposition process.

6.2.3 Deposition Conditions

The LSMO/STO (001) thin films were grown under the following deposition conditions:

- Substrate Temperature: 650° C
- Target Substrate Distance: 100 mm
- Pressure Conditions: A pressure of 0.2 mbar O_2 was maintained with dynamic flow of gas in the chamber.
- Laser Fluence: 1.6 J/cm^2
- Pulse Repetition Rate: 1 Hz
- Number of Pulses: 2000 laser pulses were fired.
- Cooling Rate: 5° C/min in presence of 0.2 mbar static O_2 pressure.

6.2.4 RHEED

In situ RHEED of deposition process was performed to examine the growth quality of the thin films. Then a 30 kV electron beam parameters with beam current of 1.6 µA was used for the imaging. It can be easily seen in Fig. 6.2 (a) that the specular spot intensity is very high and the three solid spots indicate a bare substrate surface. The image taken after deposition at room temperature under vacuum *i.e.* Fig.5.7 (b), shows a dimmer specular spot with long streaks along the spots indicating a 2D layer by layer growth.

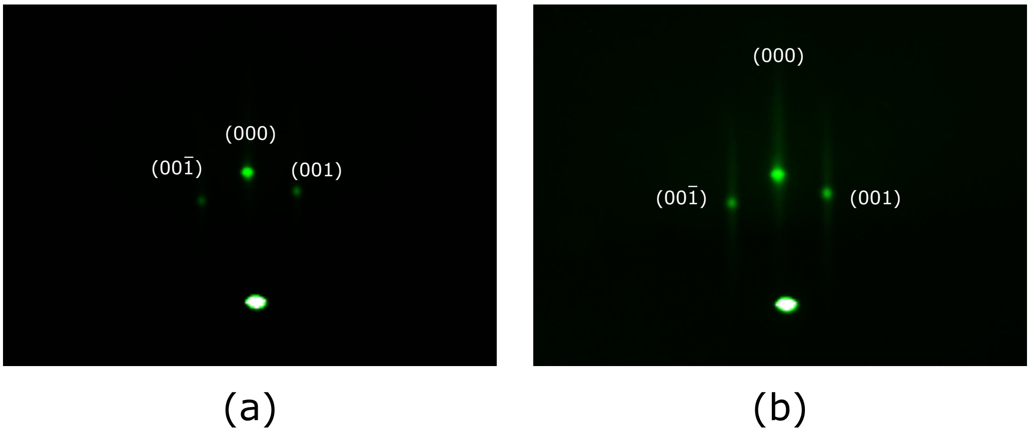

(a) (b)

Figure 6.2: (a) RHEED of STO(001) substrate taken before deposition at 650°C in vacuum. (b) RHEED of LSMO film deposited on STO(001) substrate after 2000 laser pulses, taken at room temperature in vacuum. The labelling indicate the corresponding miller indices.

6.3 Growth Characterisation

The structural characterisation of the LSMO/STO(001) thin films was carried out by X-ray diffraction and X-ray reflectivity experiments. Cu K-α radiation of wavelength

1.504 Å was used for all scans.

6.3.1 X Ray Diffraction

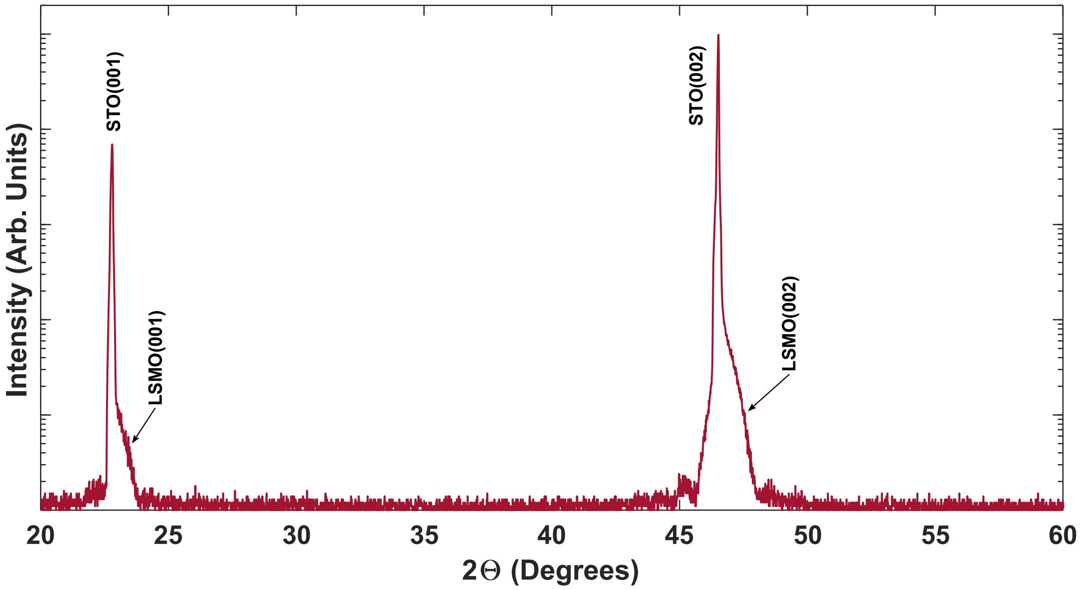

Figure 6.3: $\Theta - 2\Theta$ X Ray Diffraction spectra of LSMO/STO(001) thin film prepared by pulsed laser deposition method. The spectra shows the peaks for the LSMO thin film alongside the STO substrate peaks.

6.3.2 X Ray Reflectivity

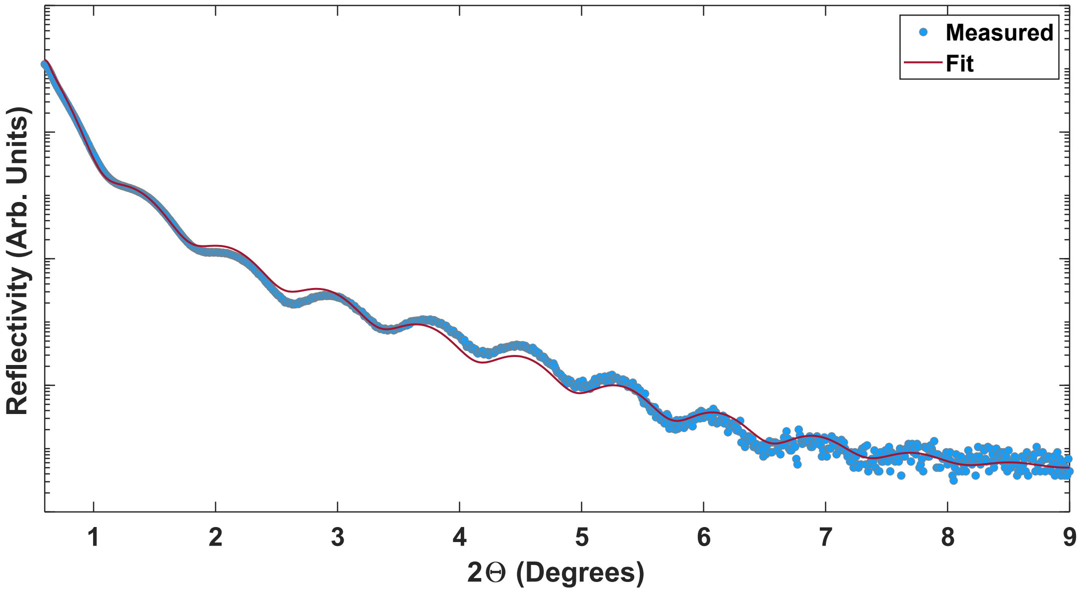

Figure 6.4: Measured and fitted X Ray Reflectivity of LSMO/STO(001) thin film prepared by pulsed laser deposition method.

From XRR data fitting, the film thickness was estimated to be 10.1 nm.

6.3.3 Atomic Force Microscopy

Atomic Force Microscopy was performed on the thin film to obtain the surface topography. Image reconstruction and statistical analysis were performed using **Gwyddion**, an open source program for visualisation and analysis of SPM (scanning probe microscopy) data.

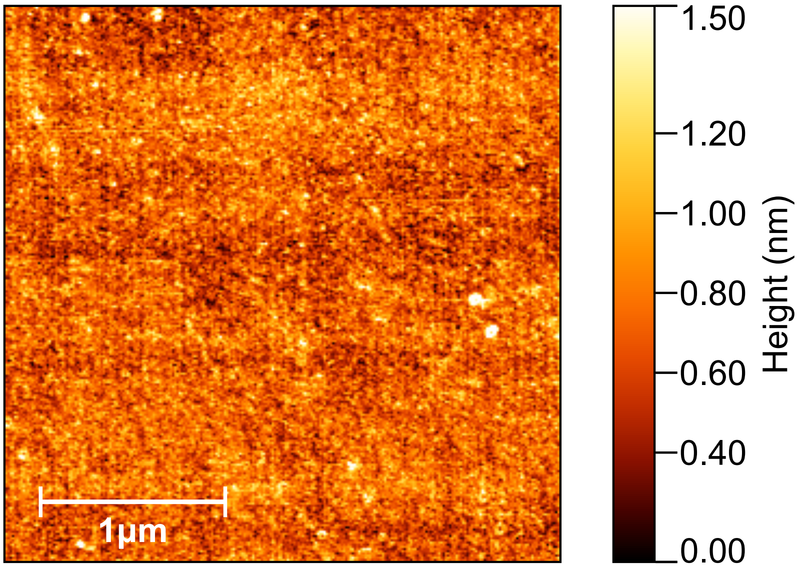

Figure 6.5: A surface topography map for a 3 × 3 µm section of the LSMO thin film, obtained by Atomic Force Microscopy (Contact Mode).

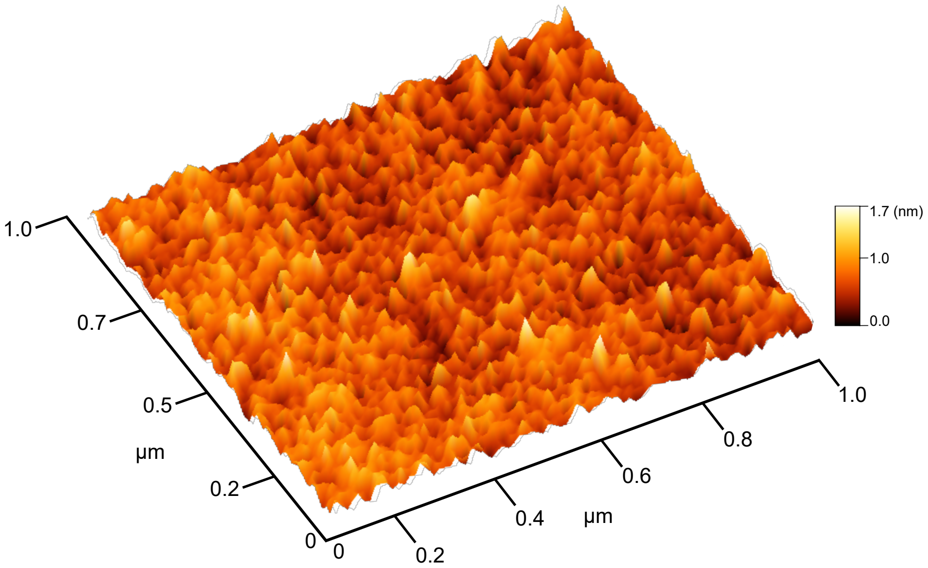

Figure 6.6: 3D reconstruction for a part of the surface of LSMO/STO(001) thin film illustrating the high homogeneity of the growth surface.

Height distribution (zero leveled) of the entire captured surface was plotted. This distribution was fit with a Gaussian. To determine the Root Mean Squared (RMS) roughness of the surface, an average cross sectional surface roughness profile was obtained my taking the average of 50 horizontal and 50 vertical line profiles along the surface.

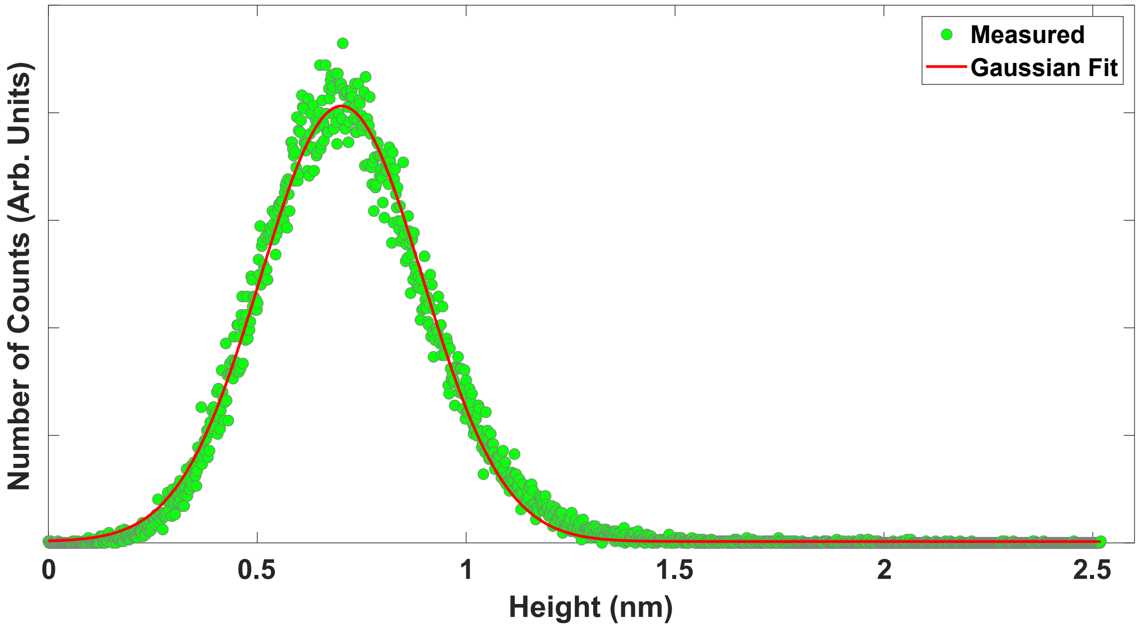

Figure 6.7: Height Distribution (zero leveled) obtained from a 3 × 3 µm section of the LSMO film. This also shows the Gaussian fitting (Red) of height distribution.

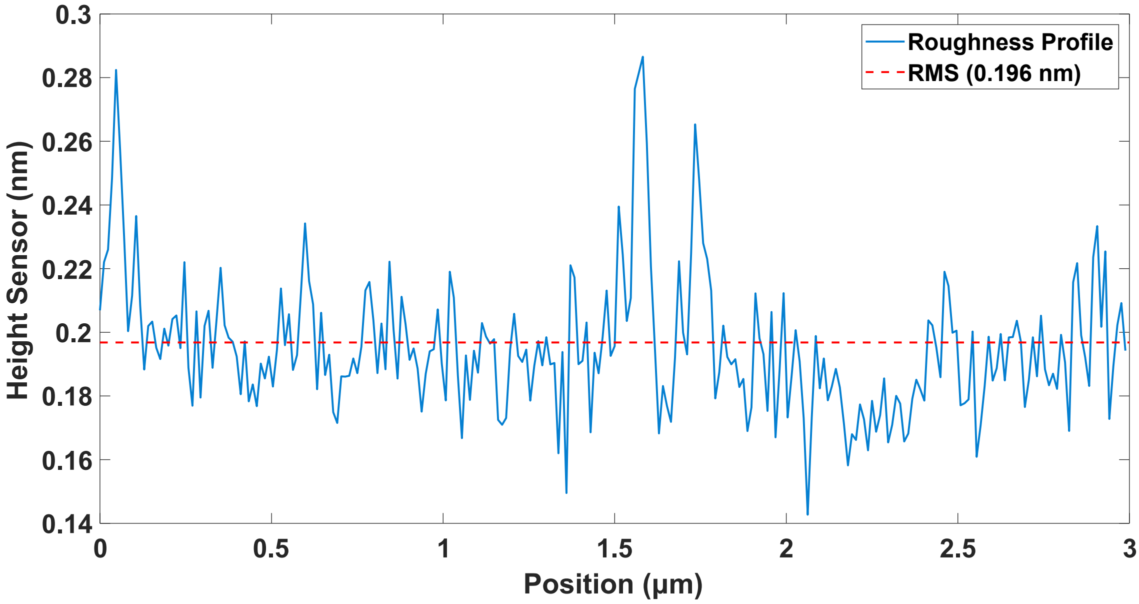

Figure 6.8: Average cross sectional roughness profile of the LSMO surface obtained by averaging 100 horizontal and vertical line profiles along the entire image. The obtained RMS roughness (dotted red line) is 0.196 nm.

6.4 Magnetic Measurements

SQUID magnetometry was performed on a 10 nm LSMO/STO(100) thin film. The sample was Field Cooled at 100 mOe to 2K and the magnetisation data was collected while increasing the temperature to 400 K.

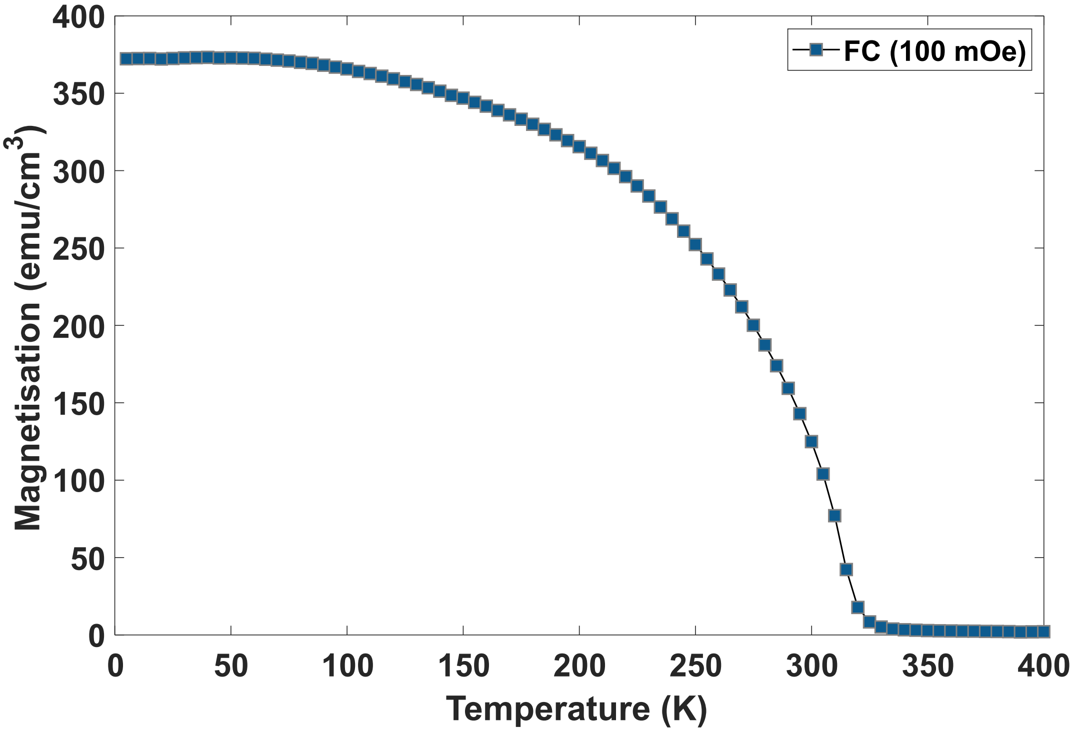

Figure 6.9: Field Cooled (10 mOe) magnetisation curve for a 10nm LSMO/BSTO(001) thin film. The sample shows a paramagnetic to ferromagnetic phase transition at around 320K.

6.5 Discussion

LSMO/STO(001) thin films were prepared by the PLD technique. The in situ RHEED pattern taken after growth shows a streaky pattern. This confirms that the 2D growth of LSMO on STO substrate has happened. The X-Ray Diffraction spectra shows the LSMO peaks only alongside the STO(001) substrate peaks, this assures that the thin film is single crystalline and epitaxial. The fitting of X-Ray reflectivity data gives an estimated LSMO film thickness of 10.1 nm, which corresponds to roughly 26 unit cells. The surface imaging was performed by Atomic Force Microscopy. Reconstruction and analysis of the images show an atomically flat surface with RMS roughness of only 0.196 nm, which is less than one unit cell height (0.386 nm) of LSMO. Finally SQUID magnetometry data of the film shows a paramagnetic to ferromagnetic phase transition at around 320 K, with a saturation magnetisation M_{sat} of 360 emu/cm^3.

Chapter 7

Growth and Characterisation of $Ba_{0.8}Sr_{0.2}TiO_3/La_{0.7}Sr_{0.3}MnO_3$ (001) Heterostructure

7.1 Introduction

Following the stabilisation of the individual ferroelectric (BSTO) and magnetic (LSMO) thin films we shift our focus towards developing a composite ferroelectric/-magnetic heterostructure to investigate the changes that might occur in the interfacial magnetic properties.

Electrically induced magnetic reconstruction has been predicted using computational methods and *ab initio* calculations for a variety of heterostructure interfaces such as $Fe_3O_4/BaTiO_3$ (001) [94], ferromagnet/ferroelectric/normal-metal superlattices [95] and manganite/titanate supercells [96]. Burton and Tsymbal [97], via first principle calculations on $La_{1-x}A_xMnO_3/BaTiO_3$ interface, where A is a divalent cation, show that the reversal of ferroelectric polarisation of $BaTiO_3$ leads to a change in the magnetic order at the interface from ferromagnetic to antiferromagnetic. In contrast a recent study by Kabanov *et. al* [98] involving *ab initio* investigation of different types of $LaMnO_3/BaTiO_3$ heterointerfaces, show that the interface becomes conducting and simultaneously exhibits an antiferromagnetic to ferromagnetic change of interfacial magnetic ordering.

The number of exciting experimental investigations that aim to study the change in magnetic behaviour in such interfaces is quite low. However, some recent attempts have been made in this direction, which employ various experimental tecniques. Meyer *et. al* [99] in 2016 reported the magnetoelectric coupling of magnetism and ferroelectric polarisation within a couple of nanometers with a FE/TMO $PbZr_{0.2}Ti_{0.8}O_3$/ $La_{0.2}Sr_{0.8}MnO_3$ system, probed by polarised neutron reflectometry. In 2021 Bocirnea *et. al* [100] studied the polarisation driven magnetism in $Ni/BaTiO_3$

interface. In the same year Yamada *et. al* [101] reported anisotropic magnetoresistance effect in an epitaxial $Co_2FeSi/BaTiO_3$ interfacial multiferroic system. However, no reports have been made on the strained ferroelectric/ferromagnetic interfaces like $Ba_{0.8}Sr_{0.2}TiO_3/La_{0.3}Sr_{0.7}MnO_3$. So we aim to study this particular composite heterostructure system by the use of SQUID magnetometry.

7.2 Sample Growth

7.2.1 Substrates

$SrTiO_3$ single crystalline substrates with (001) orientation were used to grow BSTO/LSMO heterostructures. The substrates were prepared for deposition in the same process as mentioned in Sec. 5.3.1.

7.2.2 Deposition Conditions

The heterostructure was prepared in 2 stages. First, the LSMO magnetic layer was grown under the following deposition conditions.

- Substrate Temperature: 650° C
- Target Substrate Distance: 100 mm
- Pressure conditions: A pressure of 0.2 mbar O_2 was maintained with a dynamic flow of gas in the chamber.
- Laser Fluence: 1.6 J/cm^2
- Pulse Repetition Rate: 1 Hz
- Number of LSMO pulses: 2000 laser pulses were fired.

Following this, the Ferroelectric BSTO layer was grown on top of LSMO at these deposition conditions.

- Substrate Temperature: 650° C
- Target Substrate Distance: 72 mm
- Pressure Conditions: A pressure of 0.2 mbar O_2 was maintained with a dynamic flow of gas in the chamber.
- Laser Fluence: 1.7 J/cm^2
- Pulse Repetition Rate: 4 Hz
- Number of BSTO pulses: 12,000 laser pulses were fired.

The sample was cooled at a rate of 5° C/min in the presence of static 0.2 mbar O_2.

7.3 Growth Characterisation

7.3.1 X Ray Diffraction

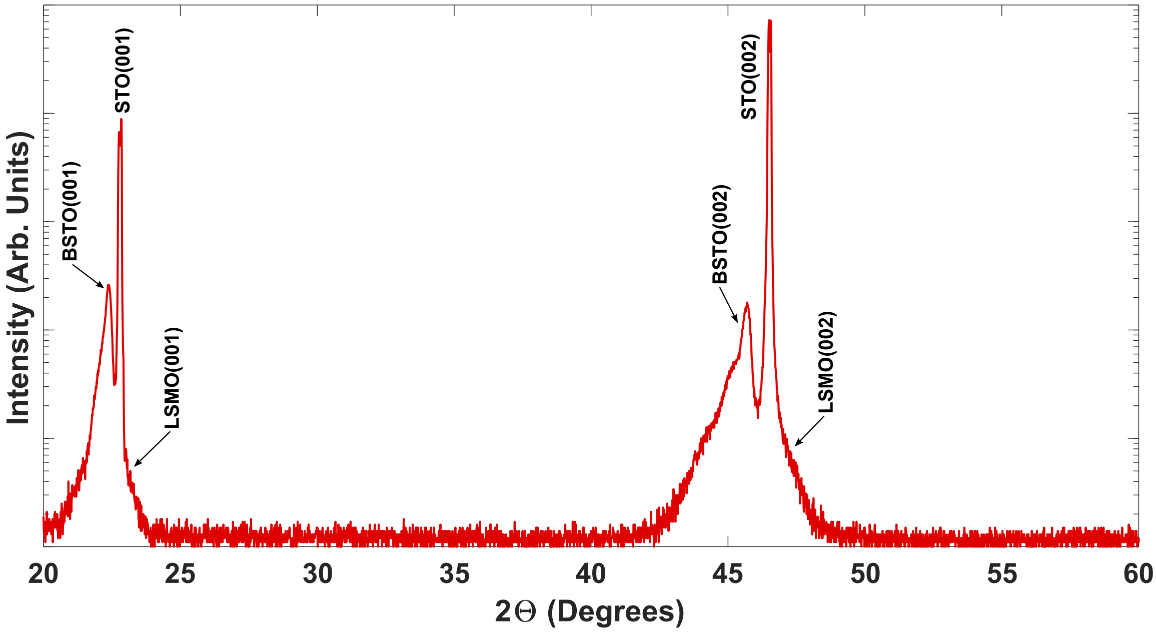

Figure 7.1: Θ−2Θ X Ray Diffraction spectra of BSTO/LSMO/STO(001) heterostructure. The spectra shows the peaks for the LSMO and BSTO layers alongside the STO substrate peaks.

7.3.2 X Ray Reflectivity

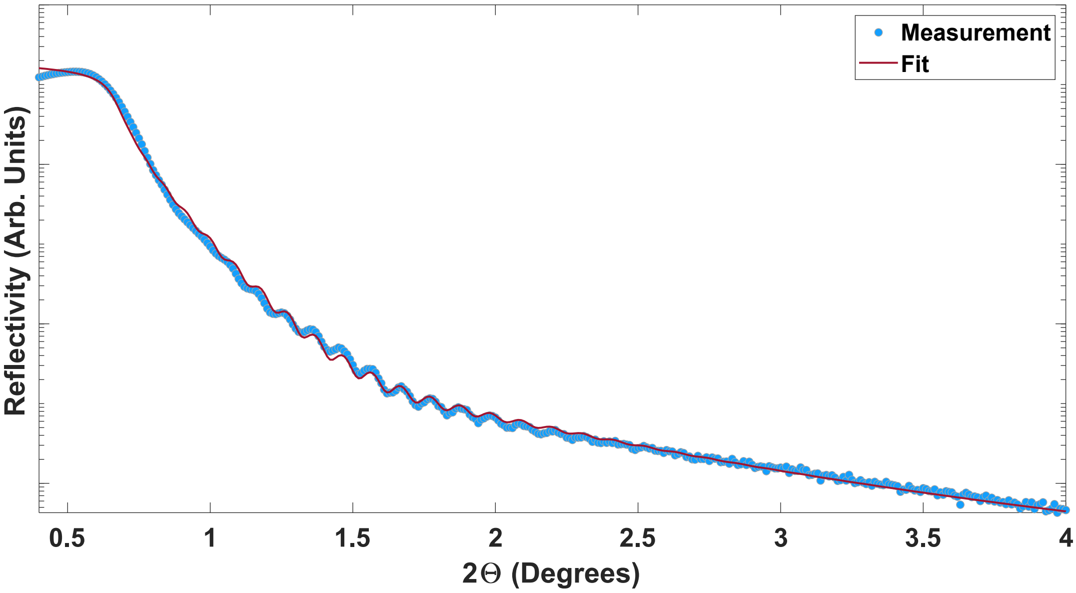

Figure 7.2: Measured and fitted X Ray Reflectivity of BSTO/LSMO/STO(001) thin film prepared by pulsed laser deposition method.

From XRR data fitting the following thickness were estimated: BSTO - 75.7 nm, LSMO - 1.7nm.

7.3.3 Atomic Force Microscopy

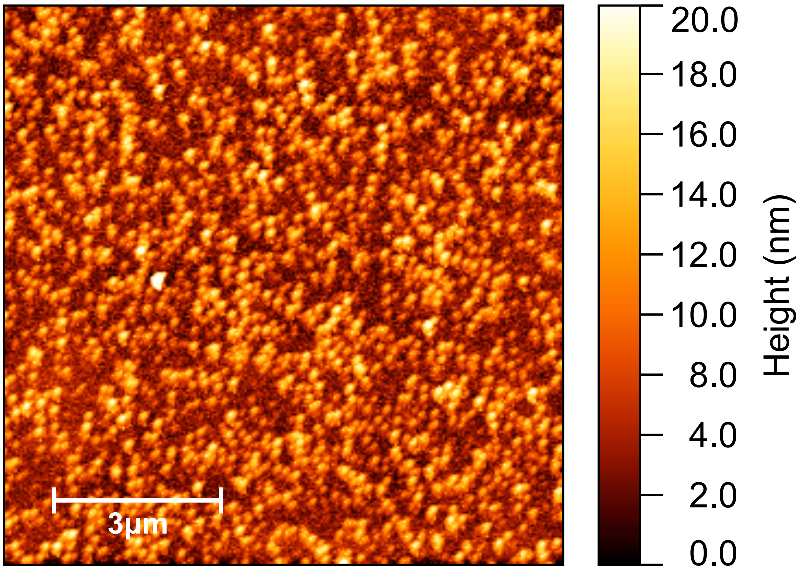

Figure 7.3: A surface topography map for a 10 × 10 µm section of the LSMO/BSTO/STO(001) heterostructure, obtained by Atomic Force Microscopy (Contact Mode).

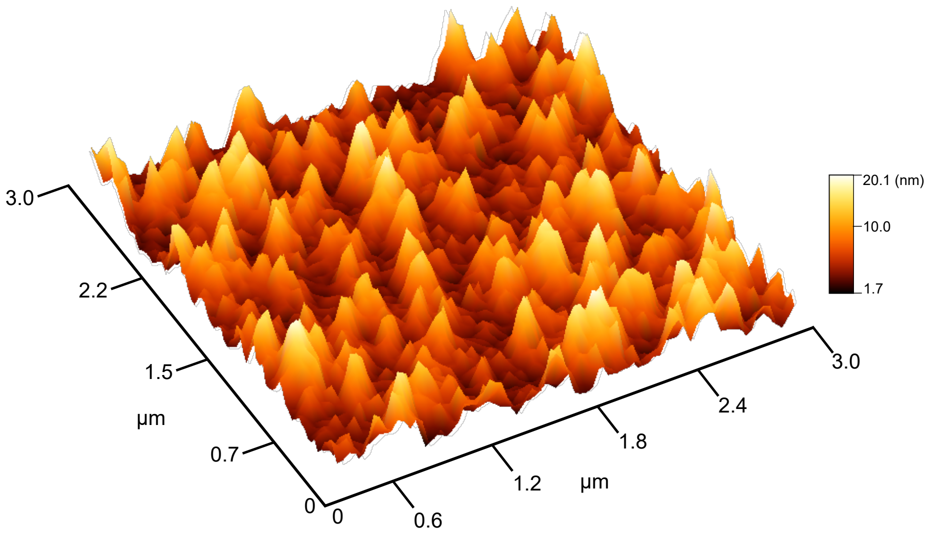

Figure 7.4: 3D reconstruction for a part of the surface of LSMO/BSTO/STO(001) heterostructure illustrating high in-homogeneity of the top surface of bilayer.

For statistical analysis, a method similar to Sec. 6.3.3 was followed. The only difference being that these procedures were followed on a 10 × 10 µm section image of the surface, and for roughness analysis, 250 horizontal and 250 vertical line profiles were averaged.

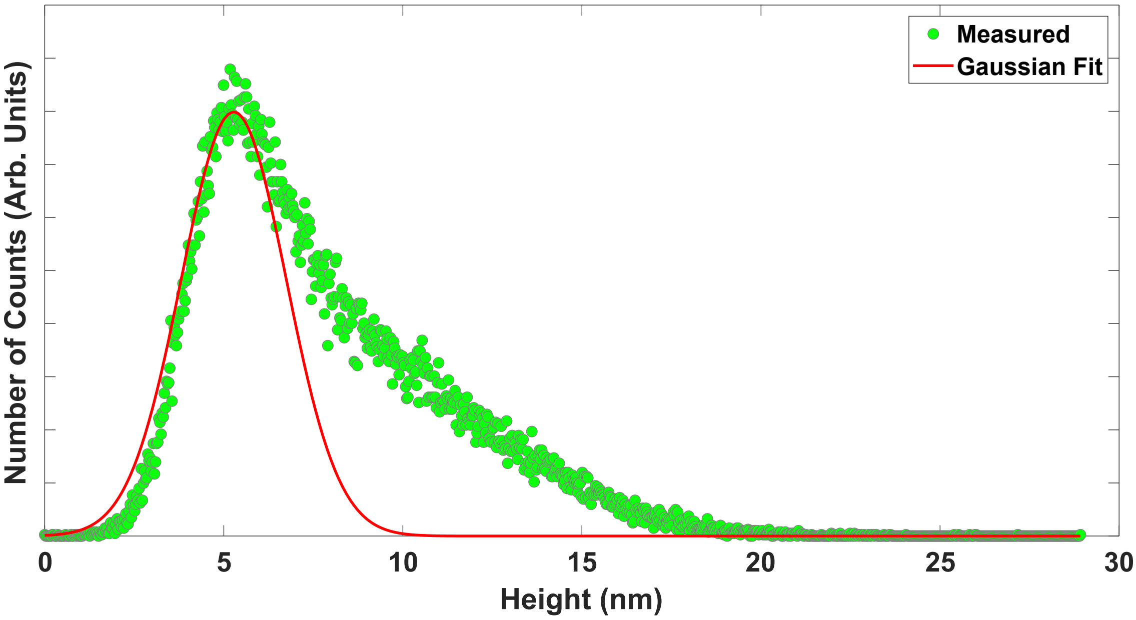

Figure 7.5: Height Distribution (zero leveled) obtained from a 10 × 10 µm section of the LSMO/BSTO bilayer. This also shows an attempted Gaussian fitting (Red) of height distribution.

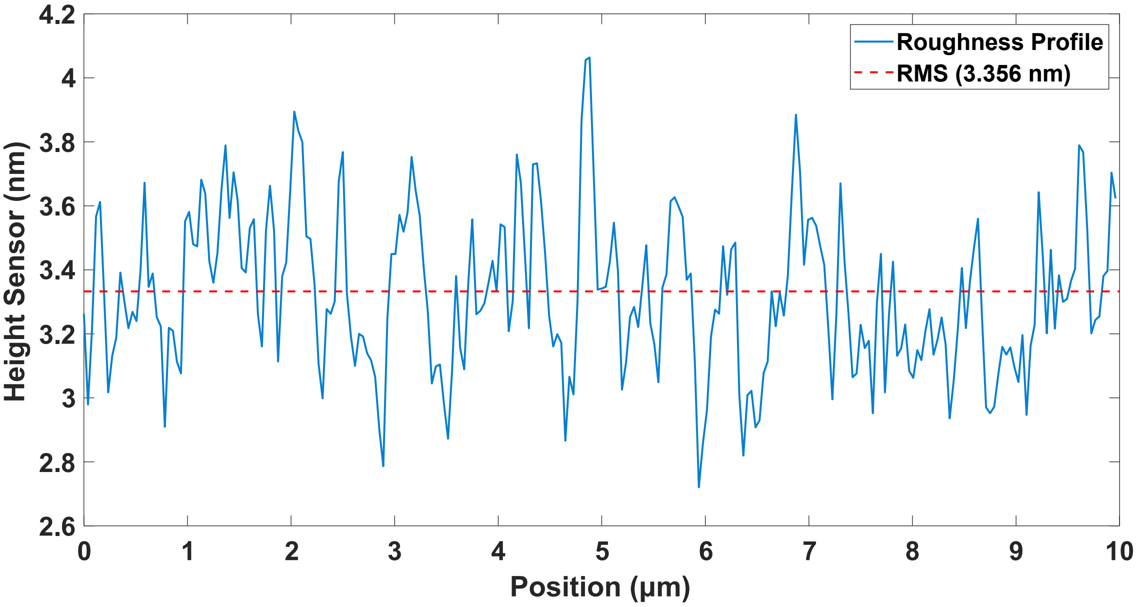

Figure 7.6: Average cross sectional roughness profile of the LSMO/BSTO bilayer surface obtained by averaging 500 horizontal and vertical line profiles along the entire image. The obtained RMS roughness (dotted red line) is about 3.356 nm.

7.4 Discussion

LSMO/BSTO/STO(001) heterostructures were prepared using the same deposition conditions as the individual thin films. The XRD spectra shows the BSTO peaks clearly but the LSMO peaks are less broad as compared to the individual thin films. XRR curve fitting shows that the BSTO layer thickness is 75.7 nm corresponding to 190 u.c., the top layer LSMO shows a thickness of only 1.7nm (5 u.c.). This thickness is extremely small and shows that the growth of LSMO could not stabilise on to of BSTO. Atomic Force Microscopy reveals that the top surface of the heterostructure is extremely rough with RMS roughness of 3.356 nm. Such high roughness doesn't allow for the epitaxial growth of LSMO.

So this heterostructure needs to be optimised before any meaningful magnetic experiments can be performed on it. This is the next planned part of this project.

Chapter 8

Conclusion and Future Prospects

The general summary of the work done and the results obtained in this thesis, followed by the future plans and prospects of this research work are discussed here.

For the study of ferroelectrically driven interfacial control of magnetism, BSTO was chosen as the candidate ferroelectric due to it's lower lattice constant and improved strain compared to its mother compound BTO.The material was synthesised by solid state reaction method followed by phase characterisation with powder XRD. The ferroelectric nature of BSTO thin films were prepared by thr Pulsed Laser Deposition method, was confirmed by P-E loop measurements and impedance analysis.

The candidate transition metal oxide for the study was chosen to be LSMO. The grown thin films were of high epitaxial quality and were atomically flat which was verified by RHEED, X-Ray Diffraction, X-Ray Reflectivity and Atomic Force Microscopy experiments. The thin films displayed a paramagnetic to ferromagnetic phase transition at around 320 K in field cooled SQUID Magnetometry experiments.

In the final part of the thesis we made initial attempts to make heterostructures of LSMO/BSTO/STO(001) following the optimised parameters for individual BSTO and LSMO thin films. However, we encountered several issues of ferroelectric relaxation and high surface roughness which made the stabilisation of LSMO on BSTO difficult. This caused the top layer of LSMO to become very thin which cannot be used as candidate samples for our study of composite magnetic/ferroelectric heterostructures.

Future Prospects

Since the initial attempts of heterostructure growth was not as per our expectations, the immediate plans are to stabilise an appreciable thickness of LSMO on BSTO by optimising the growth process. Once the stable heterostructures are confirmed by structural analysis experiments, we shall move on to the magnetometry experiments and make a detailed comparison between the magnetic data of the thin film and heterostructure to study the influence of BSTO on the interfacial magnetism of LSMO.

We also plan to do magnetotransport studies on these samples to illustrate the effect of the ferroelectric material's local electric field on the transport properties of LSMO.

Detailed analysis of the results from the above studies will open up avenues of new research problems from a fundamental point of view in the field of interfacial magnetic and transport studies of transition metal oxide/ferroelectric heterostructures.

References

[1] N. A. Spaldin and M. Fiebig, "The Renaissance of Magnetoelectric Multiferroics", Science **309**, 391 (2005).

[2] M. Fiebig, "Revival of the magnetoelectric effect", J. Phys. D: Appl. Phys. **38**, R123 (2005).

[3] W. Eerenstein, N. D. Mathur, and J. F. Scott, "Multiferroic and Magnetoelectric Materials", Nature **442**, 759 (2006).

[4] R. Ramesh and N. A. Spaldin, "Multiferroics: Progress and prospects in thin films", Nat. Mater. **6**, 21 (2007).

[5] F. Matsukura, Y. Tokura, and H. Ohno, "Control of magnetism by Electric Field", Nat. Nanotech. **10**, 209 (2015).

[6] T. Zhu, F. Orlandi, P. Manuel, A. S. Gibbs, W. Zhang, P. S. Halasyamani, and M. A. Hayward, "Directed synthesis of a hybrid improper magnetoelectric multiferroic material", Nat. Commun. **12**, 4945 (2021).

[7] N. A. Hill, "Why are There so Few Magnetic Ferroelectrics?", J. Phys. Chem. B **104**, 6694 (2000).

[8] S.-W. Cheong and M. Mostovoy, "Multiferroics: A magnetic twist for Ferroelectricity", Nat. Mater. **6**, 13 (2007).

[9] T. Kimura, T. Goto, H. Shintani, K. Ishizaka, T. Arima, and Y. Tokura, "Magnetic control of Ferroelectric Polarization", Nature **426**, 55 (2003).

[10] M. Imada, A. Fujimori, and Y. Tokura, "Metal-Insulator Transitions", Rev. Mod. Phys. **70**, 1039 (1998).

[11] L. W. Martin and A. M. Rappe, "Thin-film ferroelectric materials and their applications", Nat. Rev. Mater. **2**, 16087 (2016).

[12] A. Goldman, "Electrostatic Gating of Ultrathin Films", Annu. Rev. Mater. Res. **44**, 45 (2014).

[13] C. H. Ahn, A. Bhattacharya, M. Di Ventra, J. N. Eckstein, C. D. Frisbie, M. E. Gershenson, A. M. Goldman, I. H. Inoue, J. Mannhart, A. J. Millis, A. F. Morpurgo, D. Natelson, and J.-M. Triscone, "Electrostatic modification of novel materials", Rev. Mod. Phys. **78**, 1185 (2006).

[14] C. H. Ahn, J.-M. Triscone, and J. Mannhart, "Electric field effect in correlated oxide systems", Nature **424**, 1015 (2003).

[15] C.-W. Nan, M. I. Bichurin, S. Dong, D. Viehland, and G. Srinivasan, "Multiferroic magnetoelectric composites: Historical perspective, status, and future directions", J. Appl. Phys. **103**, 031101 (2008).

[16] G. Srinivasan, "Magnetoelectric composites", Annu. Rev. Mater. Res. **40**, 153 (2010).

[17] X. Huang and S. Dong, "Ferroelectric control of magnetism and transport in oxide heterostructures", Modern Physics Letters B **28**, 1430010 (2014).

[18] J. Y. Kim, M.-J. Choi, and H. W. Jang, "Ferroelectric field effect transistors: progress and perspective", APL Mater. **9**, 021102 (2021).

[19] S. Zhang, "Spin-dependent surface screening in ferromagnets and magnetic tunnel junctions", Phys. Rev. Lett. **83**, 640 (1999).

[20] J. M. Rondinelli, M. Stengel, and N. A. Spaldin, "Carrier-mediated magnetoelectricity in complex oxide heterostructures", Nat. Nanotech. **3**, 46 (2007).

[21] J. P. Velev, S. S. Jaswal, and E. Y. Tsymbal, "Multi-ferroic and magnetoelectric materials and interfaces", Phil. Trans. R. Soc. A. **369**, 3069 (2011).

[22] C. Song, B. Cui, J. Peng, H. Mao, and F. Pan, "Electrical control of magnetism in oxides", Chinese Phys. B **25**, 067502 (2016).

[23] N. A. Spaldin, "Multiferroics beyond electric-field control of magnetism", Proc. R. Soc. A. **476**, 20190542 (2020).

[24] M. A. Peña and J. L. Fierro, "Chemical structures and performance of perovskite oxides", Chem. Rev. **101**, 1981 (2001).

[25] H. A. Jahn and E. Teller, "Stability of polyatomic molecules in degenerate electronic states : I—orbital degeneracy", Proc. R. Soc. Lond. A **161**, 220 (1937).

[26] R. Freitag and J. Conradie, "Understanding the Jahn–Teller Effect in Octahedral Transition-Metal Complexes: *A* molecular orbital view of the Mn(β-diketonato)$_3$ complex", J. Chem. Educ. **90**, 1692 (2013).

[27] I. Turek, J. Kudrnovský, V. Drchal, and P. Bruno, "Exchange interactions, spin waves, and transition temperatures in itinerant magnets", Philosophical Magazine **86**, 1713 (2006).

[28] M. Pajda, J. Kudrnovský, I. Turek, V. Drchal, and P. Bruno, "Ab initio calculations of exchange interactions, spin-wave stiffness constants, and curie temperatures of Fe, Co, and Ni", Phys. Rev. B **64**, 174402 (2001).

[29] W. Heitler and F. London, "Wechselwirkung neutraler Atome und homopolare Bindung nach der Quantenmechanik. Zeitschrift für Physik", Zeitschrift fr Physik **44**, 455 (1927).

[30] S. J. Blundell, *Magnetism in condensed matter* (Oxford University Press, 2014).

[31] J. Kübler, "Magnetic moments of ferromagnetic and antiferromagnetic BCC and FCC Iron", Physics Letters A **81**, 81 (1981).

[32] J. C. Slater and G. F. Koster, "Simplified lcao method for the periodic potential problem", Phys. Rev. **94**, 1498 (1954).

[33] D. Khomskii, "Electronic structure, exchange and magnetism in oxides", in *Spin electronics*, edited by M. Ziese and M. J. Thornton (Springer Berlin Heidelberg, Berlin, Heidelberg, 2001), pp. 89–116.

[34] J. B. Goodenough, "Theory of the role of Covalence in the perovskite-type manganites[La,*M(II)*]MnO_3", Phys. Rev. **100**, 564 (1955).

[35] J. B. Goodenough, "An interpretation of the magnetic properties of the perovskite-type mixed crystals $La_{1-x}Sr_xCoO_{3-\lambda}$", J. Phys. Chem. Solids **6**, 287 (1958).

[36] J. Kanamori, "Superexchange interaction and symmetry properties of electron orbitals", J. Phys. Chem. Solids **10**, 87 (1959).

[37] P. W. Anderson, "Antiferromagnetism. Theory of Superexchange Interaction", Phys. Rev. **79**, 350 (1950).

[38] D. Samal, *"On The Magnetic And Magnetotransport Studies Of Cobaltates And Superconductor/ Ferromagnet Heterostructures"* (Indian Institute of Science, Bangalore, 2011).

[39] C. M. Zener, "Interaction between the $\boldsymbol{d}$ shells in the Transition Metals", Phys. Rev. **81**, 440 (1951).

[40] P. Orgiani, A. Galdi, C. Aruta, V. Cataudella, G. De Filippis, C. A. Perroni, V. Marigliano Ramaglia, R. Ciancio, N. B. Brookes, M. Moretti Sala, G. Ghiringhelli, and L. Maritato, "Multiple double-exchange mechanism by Mn^{2+} doping in manganite compounds", Phys. Rev. B **82**, 205122 (2010).

[41] P. W. Anderson and H. Hasegawa, "Considerations on Double Exchange", Phys. Rev. **100**, 675 (1955).

[42] M. Getzlaff, *Fundamentals of Magnetism* (Springer, 2010).

[43] K. Yosida, *Theory of Magnetism* (Springer, 1998).

[44] K. Yosida, “Magnetic properties of Cu-Mn alloys”, Phys. Rev. **106**, 893 (1957).

[45] J. F. Nye, *Physical properties of crystals: their representation by tensors and matrices* (Clarendon Press, 2011).

[46] F. Seitz, D. Turnbull, H. Ehrenreich, and C. S. Smith, “Macroscopic Symmetry and Properties of Crystals”, in *Solid state physics: Advances in research and applications*, Vol. 22 (Academic Press, 1968), pp. 175–249.

[47] S. V. Kalinin, B. Mirman, and E. Karapetian, “Relationship between direct and converse piezoelectric effect in a nanoscale electromechanical contact”, Phys. Rev. B **76**, 212101 (2007).

[48] P. M. Woodward, “Octahedral Tilting in Perovskites. I. Geometrical Considerations”, Acta Cryst. B **53**, 32 (1997).

[49] P. M. Woodward, “Octahedral Tilting in Perovskites. II. Structure Stabilizing Forces”, Acta Cryst. B **53**, 44 (1997).

[50] V. M. Goldschmidt, “Die gesetze der Krystallochemie (The laws of crystallochemistry)”, Die Naturwissenschaften **14**, 477 (1926).

[51] W. Cochran, “Crystal stability and the theory of ferroelectricity”, Phys. Rev. Lett. **3**, 412 (1959).

[52] A. P. Levanyuk, I. B. Misirlioglu, and M. B. Okatan, “Landau, ginzburg, devonshire and others”, Ferroelectrics **569**, 310 (2020).

[53] C. K. Wong and F. G. Shin, “A simplified treatment of the landau theory of phase transitions for thin ferroelectric films”, American Journal of Physics **76**, 31 (2008).

[54] K.-H. Chew, Y. Ishibashi, F. G. Shin, and H. L. W. Chan, “Effective Landau-Devonshire-Type Theory of Phase Transitions in Ferroelectric Thin Films Based on the Tilley–Zeks Model”, J. Phys. Soc. Jpn. **72**, 2972 (2003).

[55] P. Chandra and P. B. Littlewood, “A Landau Primer for Ferroelectrics”, in *Physics of Ferroelectrics: A Modern Perspective* (Springer, 2007), pp. 69–116.

[56] N. A. Spaldin, “Analogies and Differences between Ferroelectrics and Ferromagnets”, in *Physics of Ferroelectrics: A Modern Perspective* (Springer, 2007), pp. 175–218.

[57] P. S. Halasyamani and K. R. Poeppelmeier, “Noncentrosymmetric oxides”, Chem. Mater. **10**, 2753 (1998).

[58] I. B. Bersuker, “Pseudo-Jahn-Teller Effect - A Two-State Paradigm in Formation, Deformation, and Transformation of Molecular Systems and Solids”, Chem. Rev. **113**, 1351 (2013).

[59] P. R. Willmott and J. R. Huber, “Pulsed laser vaporization and deposition”, Rev. Mod. Phys. **72**, 315 (2000).

[60] R. W. Eason and D. P. Norton, “What is PLD?”, in *Pulsed laser deposition of thin films: applications-led growth of functional materials* (Wiley, 2007).

[61] P. Kuppusami and V. S. Raghunathan, “Status of pulsed laser deposition: Challenges and opportunities”, Surface Engineering **22**, 81 (2006).

[62] R. Timm, P. R. Willmott, and J. R. Huber, “Ablation and blow-off characteristics at 248 nm of Al, Sn and Ti targets used for thin film pulsed laser deposition”, J. Appl. Phys. **80**, 1794 (1996).

[63] D. Bhattacharya, R. K. Singh, and P. H. Holloway, “Laser-target interactions during pulsed laser deposition of superconducting thin films”, J. Appl. Phys. **70**, 5433 (1991).

[64] J. C. Kools, T. S. Baller, S. T. De Zwart, and J. Dieleman, “Gas flow dynamics in laser ablation deposition”, J. Appl. Phys. **71**, 4547 (1992).

[65] R. K. Singh and J. Narayan, “Pulsed-laser evaporation technique for deposition of thin films: physics and theoretical model”, Phys. Rev. B **41**, 8843 (1990).

[66] S. Amoruso, R. Bruzzese, N. Spinelli, R. Velotta, M. Vitiello, and X. Wang, “Dynamics of laser-ablated MgB_2 plasma expanding in argon probed by optical emission spectroscopy”, Phys. Rev. B **67**, 224503 (2003).

[67] P. E. Dyer, A. Issa, and P. H. Key, “Dynamics of excimer laser ablation of superconductors in an oxygen environment”, Appl. Phys. Lett. **57**, 186 (1990).

[68] M. Ohring, *Materials science of thin films: Deposition and structure* (Academic Press, 2002).

[69] *PLD System User Manual*, English, version 1.0.1, Twente Solid State Technology B.V., Netherlands (2015), 102 pp.

[70] C. Hammond, *The basics of crystallography and diffraction* (University Press, 2015).

[71] G. H. Stout and L. H. Jensen, *X-ray structure determination: A practical guide* (J. Wiley, 1989).

[72] B. D. Cullity, *Elements of X-ray diffraction* (Addison-Wesley Publishing Company, 1956).

[73] W. H. Bragg and W. L. Bragg, “The reflection of X-rays by crystals”, Proc. R. Soc. Lond. A **88**, 428 (1913).

[74] Y. Fujii, “Recent developments in the X-ray reflectivity analysis”, American Journal of Physics and Applications **4**, 27 (2016).

[75] B. K. Tanner, "Grazing Incidence X-Ray Reflectivity and Scattering", in *Handbook of advanced non-destructive evaluation*, edited by N. Ida and N. Meyendorf (Springer International Publishing, Cham, 2018), pp. 1–34.

[76] R. Matyi, L. Depero, E. Bontempi, P. Colombi, A. Gibaud, M. Jergel, M. Krumrey, T. Lafford, A. Lamperti, M. Meduna, and et al., "The international VAMAS project on X-ray reflectivity measurements for evaluation of Thin Films and multilayers-preliminary results from the second round-robin", Thin Solid Films **516**, 7962 (2008).

[77] B. Josephson, "Possible new effects in superconductive tunnelling", Physics Letters **1**, 251 (1962).

[78] P. W. Anderson and J. M. Rowell, "Probable Observation of the Josephson Superconducting Tunneling Effect", Phys. Rev. Lett. **10**, 230 (1963).

[79] U. Mizutani, *Introduction to the electron theory of metals* (Cambridge University Press, 2003).

[80] A. R. Innes and E. Rhoedrick, *Introduction to Superconductivity*, 2nd ed. (Pergamon, 1978).

[81] M. Buchner, K. Höfler, B. Henne, V. Ney, and A. Ney, "Tutorial: basic principles, limits of detection, and pitfalls of highly sensitive squid magnetometry for nanomagnetism and spintronics", J. Appl. Phys. **124**, 161101 (2018).

[82] B. Jaffe, W. R. Cook, and C. J. H. Ludwig, *Piezoelectric ceramics* (Academic Press, 1971).

[83] K. Uchino, *Ferroelectric devices* (CRC Press, 2018).

[84] D. L. Ko, M. F. Tsai, J. W. Chen, P. W. Shao, Y. Z. Tan, J. J. Wang, S. Z. Ho, Y. H. Lai, Y. L. Chueh, Y. C. Chen, D. P. Tsai, L.-Q. Chen, and Y. H. Chu, "Mechanically controllable nonlinear dielectrics", Sci. Adv. **6**, 3180 (2020).

[85] V. Garcia, S. Fusil, K. Bouzehouane, S. Enouz-Vedrenne, N. D. Mathur, A. Barthélémy, and M. Bibes, "Giant tunnel electroresistance for non-destructive readout of Ferroelectric States", Nature **460**, 81 (2009).

[86] D. A. Tenne, P. Turner, J. D. Schmidt, M. Biegalski, Y. L. Li, L. Q. Chen, A. Soukiassian, S. Trolier-McKinstry, D. G. Schlom, X. X. Xi, D. D. Fong, P. H. Fuoss, J. A. Eastman, G. B. Stephenson, C. Thompson, and S. K. Streiffer, "Ferroelectricity in Ultrathin $BaTiO_3$ Films: Probing the Size Effect by Ultraviolet Raman Spectroscopy", Phys. Rev. Lett. **103**, 177601 (2009).

[87] Y.-H. Chu, Q. Zhan, L. W. Martin, M. P. Cruz, P.-L. Yang, G. W. Pabst, F. Zavaliche, S.-Y. Yang, J.-X. Zhang, L.-Q. Chen, D. G. Schlom, I.-N. Lin, T.-B. Wu, and R. Ramesh, “Nanoscale Domain Control in Multiferroic $BiFeO_3$ Thin Films”, Adv. Mater. **18**, 2307.

[88] I. K. Bdikin, J. A. Pérez, I. Coondoo, A. M. R. Senos, P. Q. Mantas, and A. L. Kholkin, “Ferroelectric domain structure of $PbZr_{0.35}Ti_{0.65}O_3$ single crystals by piezoresponse force microscopy”, J. Appl. Phys. **110**, 052003 (2011).

[89] H. Wu, X. Ma, Z. Zhang, J. Zeng, J. Wang, and G. Chai, “Effect of crystal orientation on the phase diagrams, dielectric and piezoelectric properties of epitaxial $BaTiO_3$ thin films”, AIP Advances **6**, 015309 (2016).

[90] Z. Li, Z. Zhang, J. Liu, R. Zhu, B. Ge, Y. Li, X. Zhang, P. Gao, D. Wang, X. Xu, W. Tian, and Y. Jiang, “Enhancement of Interfacial Polarization in $BaTiO_3$ Thin Films via Oxygen Inhomogeneity”, Adv. Electron. Mater. **8**, 2100876 (2021).

[91] R. Guo, L. Shen, H. Wang, Z. Lim, W. Lu, P. Yang, Ariando, A. Gruverman, T. Venkatesan, Y. P. Feng, and J. Chen, “Tailoring Self-Polarization of $BaTiO_3$ Thin Films by Interface Engineering and Flexoelectric Effect”, Adv. Mater. Interfaces **3**, 1600737 (2016).

[92] J. Van Santen and G. Jonker, “Electrical conductivity of ferromagnetic compounds of manganese with perovskite structure”, Physica **16**, 599 (1950).

[93] M. C. Martin, G. Shirane, Y. Endoh, K. Hirota, Y. Moritomo, and Y. Tokura, “Magnetism and structural distortion in the $La_{0.7}Sr_{0.3}MnO_3$ metallic ferromagnet”, Phys. Rev. B **53**, 14285 (1996).

[94] M. K. Niranjan, J. P. Velev, C.-G. Duan, S. S. Jaswal, and E. Y. Tsymbal, “Magnetoelectric effect at the $Fe_3O_4/BaTiO_3$ (001) interface: a first-principles study”, Phys. Rev. B **78**, 104405 (2008).

[95] T. Cai, S. Ju, J. Lee, N. Sai, A. A. Demkov, Q. Niu, Z. Li, J. Shi, and E. Wang, “Magnetoelectric coupling and electric control of magnetization in ferromagnet/ferroelectric/normal-metal superlattices”, Phys. Rev. B **80**, 140415 (2009).

[96] A. Ciucivara, B. Sahu, and L. Kleinman, “Density functional study of a ferromagnetic ferroelectric $LaMnO_3BaTiO_3$ superlattice”, Phys. Rev. B **77**, 092407 (2008).

[97] J. D. Burton and E. Y. Tsymbal, “Prediction of electrically induced magnetic reconstruction at the manganite/ferroelectric interface”, Phys. Rev. B **80**, 174406 (2009).

[98] V. V. Kabanov, I. I. Piyanzina, Y. V. Lysogorskiy, D. A. Tayurskii, and R. F. Mamin, “Ab initio investigation of electronic and magnetic properties of antiferromagnetic/ferroelectric LaMnO3/BaTiO3 interface”, Mater. Res. Express **7**, 055020 (2020).

[99] T. L. Meyer, A. Herklotz, V. Lauter, J. W. Freeland, J. Nichols, E.-J. Guo, S. Lee, T. Z. Ward, N. Balke, S. V. Kalinin, M. R. Fitzsimmons, and H. N. Lee, “Enhancing interfacial magnetization with a ferroelectric”, Phys. Rev. B **94**, 174432 (2016).

[100] A. E. Bocirnea, D. G. Popescu, C. Chirila, R. M. Costescu, V. Kuncser, V. Stancu, L. Trupina, I. Pasuk, A. M. Vlaicu, and M. A. Husanu, “Polarization-dependent magnetism of the Ni/$BaTiO_3$ interface”, Phys. Rev. Materials **4**, 034402 (2020).

[101] S. Yamada, Y. Teramoto, D. Matsumi, D. Kepaptsoglou, I. Azaceta, T. Murata, K. Kudo, V. K. Lazarov, T. Taniyama, and K. Hamaya, “Electric field tunable anisotropic magnetoresistance effect in an epitaxial $Co_2FeSi/BaTiO_3$ interfacial multiferroic system”, Phys. Rev. Materials **5**, 014412 (2021).